



**HAL**  
open science

# Advanced Concepts of Metamaterials for Electromagnetism and Photonics

Elena Bochkova

► **To cite this version:**

Elena Bochkova. Advanced Concepts of Metamaterials for Electromagnetism and Photonics. Optics / Photonic. Université Paris Saclay (COmUE), 2017. English. NNT : 2017SACLS441 . tel-01968035

**HAL Id: tel-01968035**

**<https://theses.hal.science/tel-01968035>**

Submitted on 2 Jan 2019

**HAL** is a multi-disciplinary open access archive for the deposit and dissemination of scientific research documents, whether they are published or not. The documents may come from teaching and research institutions in France or abroad, or from public or private research centers.

L'archive ouverte pluridisciplinaire **HAL**, est destinée au dépôt et à la diffusion de documents scientifiques de niveau recherche, publiés ou non, émanant des établissements d'enseignement et de recherche français ou étrangers, des laboratoires publics ou privés.

# Concepts avancés de métamatériaux pour l'électromagnétisme et la photonique

Thèse de doctorat de l'Université Paris-Saclay  
préparée à l'Université Paris-Sud

École doctorale n°575  
PHYSIQUE-ET-INGENIERIE: électrons, photons, sciences du vivant  
(EOBE)

Spécialité de doctorat  
Electronique et Optoélectronique, Nano- et Microtechnologies

Thèse présentée et soutenue à Orsay, le 15 décembre 2017, par

**Elena Bochkova**

## Composition du Jury :

Alexandre Bouhelier Directeur de Recherche CNRS, ICB	Président
Nicolas Bonod Chargé de Recherche CNRS/HDR, Institut Fresnel	Rapporteur
Éric Lheurette Professeur d'Université, IEMN	Rapporteur
Julien Moreau Maître de Conférences, LCF	Examineur
Shah Nawaz Burokur Maître de Conférences/HDR, LEME	Directeur de thèse
Anatole Lupu Directeur de Recherche CNRS, C2N	Co-Encadrant de thèse
Géraldine Guida Maître de Conférences/HDR, LEME	Invitée
Thomas Lepetit Ingénieur de Recherche, ONERA	Invité

# Table of contents

Acknowledgements	iii
Résumé en français	v
Chapter 1. General Introduction and Context of Study	1
Chapter 2. Dark Mode and Fano Resonance: Analysis on State-of-arts	7
2.1. Classical analog of Electromagnetically Induced Transparency	7
2.2. Plasmonic EIT viewed as bright and dark modes Fano interference	11
2.3. Plasmonic EIT revisited	19
2.4. Fabry-Perot metasurface cavities	23
2.5. Direct improvement of the resonators' quality factors	26
2.6. Simulation and measurement tools	27
2.7. Summary and conclusion	29
Chapter 3. Direct dark mode excitation mechanism based on symmetry matching	39
3.1. Symmetry matching approach	40
3.2. Control of magnetic dipole mode	47
3.2.1. Split Ring Resonator	47
3.2.2. Symmetry matching for SRR	51
3.2.3. Magnetic dipole excitation based on symmetry matching	54
3.2.4. Design optimization	57
3.2.5. Measurements	61
3.3. Dark mode engineering based on complementary MSs	63
3.3.1. Babinet's principle	63
3.3.2. Dark mode excitation in complementary MSs	65
3.4. Conclusion	70
Chapter 4. Fano resonance in Metasurface cavity	77
4.1. Basic equations of Temporal Coupled Mode Theory	78

4.2.	Resonance coupling	80
4.2.1.	Coupling between modes in individual resonator	80
4.2.2.	Near-field coupling between modes of different resonators	82
4.2.3.	Far-field coupling between modes of different resonators	85
4.3.	Metasurface cavity	87
4.3.1.	Transmission and reflection characteristics	87
4.3.2.	Engineering of radiation losses	87
4.3.3.	CMT mode analysis	90
4.3.4.	Non-radiative losses	93
4.3.5.	Experimental results	94
4.4.	Sensing capability	95
4.5.	Conclusion	98
Chapter 5.	Control of Fano Resonance in Metasurfaces	101
5.1.	Control of Fano resonance in enantiomeric metasurface	101
5.2.	Measurement result	108
5.3.	Excitation of second higher order mode	109
5.4.	Conclusions	114
Chapter 6.	Conclusions and Outlooks for Future Work	117
6.1.	Conclusions	117
6.2.	Outlooks for Future Work	118
	List of publications	123

# Acknowledgements

I would like to express my greatest gratitude to all people without whom this thesis and my three years residence in France would be impossible.

I wish especially to deeply thank my supervisor Dr. Shah Nawaz Burokur for his continuous guidance, support and infinite patience. His strategic planning, constructive comments and ability to go out difficult situations helped me to finish my dissertation.

I wish to acknowledge my co-supervisor Dr. Anatole Lupu for suggesting me to have PhD experience in France. His creative scientific ideas and physical intuition always encouraged me to work harder. I am also grateful for his help in my personal life during my PhD study. He also provided a great help in my accommodation in France.

I thank all the members of my PhD jury: Dr. Nicolas Bonod and Prof. Eric Lheurette who had the task to review my thesis, Dr. Alexandre Bouhelier for being the president of the jury, and Dr. Julien Moreau, Dr. Géraldine Guida and Dr. Thomas Lepetit for taking part in the jury. I thank every member of the jury for the discussion we had during my defense.

I send a great appreciation to Prof. Andre de Lustrac for his valuable advices and for being open for discussions. I would like also to thank Dr. Thomas Lepetit for helping me a lot to learn Coupled Mode Theory. He generously gave clear instruction and notations which considerably helped to make a progress in my work. I would like to offer my special thanks to Aloyse Degiron. Counselling with him always helped to solve problems owing to his unique experience and great competence in physics.

I am heartily grateful to my colleagues Tatiana Teperik, Natalia Dubrovina, Dylan Germain, Jianjia Yi, Quynh Le Van, Anna Niang, Yulong Fan and Vincent de Brac for their support, encouragement and warm time spending together. I would like to express my deep appreciation to Badreddine Ratni for the readiness to help at any time on any issue.

Finally, I would like to thank my husband Alexey for his infinite support. All my accomplishments during my PhD study could be impossible without his motivational spirit which he shared with me. I always got a lot of inspiration after our long discussions. I wish also to thank my parents and sister for their love and encouragement.

Lastly, I would like to acknowledge the financial support from the French Ministry of Higher Education and Research.



## Résumé en français

Les métamatériaux (MM) sont des matériaux composites artificiels conçus pour produire des propriétés électromagnétiques particulières. Le concept des métamatériaux introduit suite aux travaux de Sir J. Pendry en 1996 [Pendry 1996] représente maintenant dans son sens le plus large un éventail de structures artificielles, dont les propriétés sont étendues au-delà des limites fournies par la nature. Nous pouvons donc avoir des matériaux artificiels avec des propriétés complètement différentes des matériaux employés; par exemple des matériaux avec un indice de réfraction négatif, avec des propriétés magnétiques dans le domaine optique, des dispositifs d'illusion, des capes d'invisibilité, etc. La recherche actuelle sur les métamatériaux symbolise le début de l'ère dans laquelle les rayons électromagnétiques et la lumière influenceront profondément les processus physiques et techniques dans la vie quotidienne et dans l'industrie.

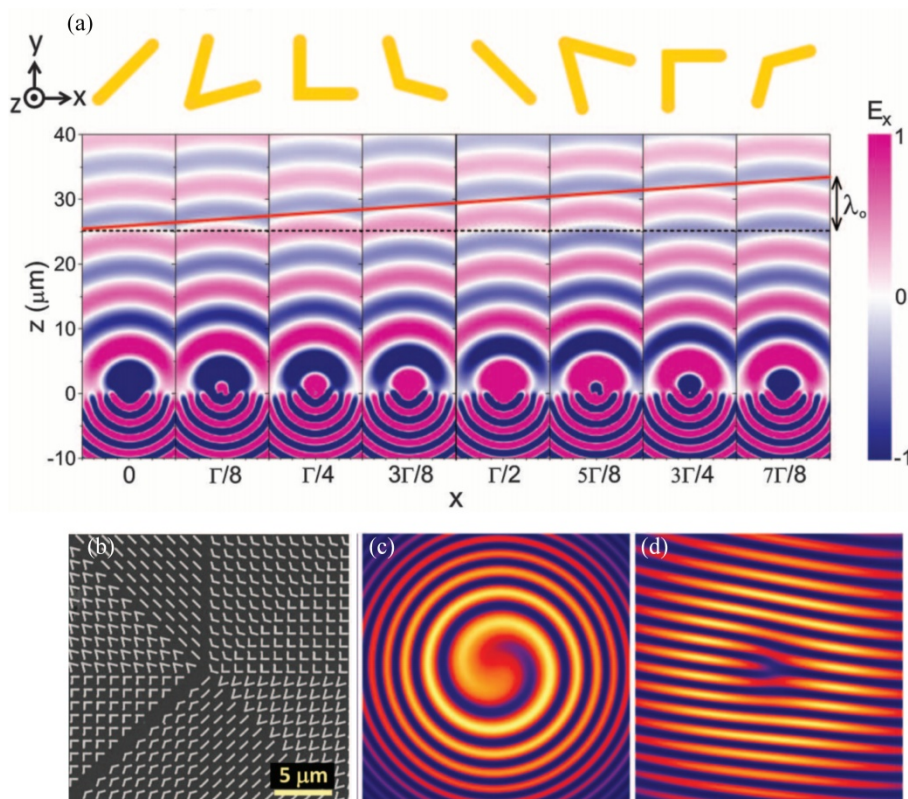


**Fig. 0.1.** Les métasurfaces contrôlent l'amplitude la phase et la polarisation d'une onde électromagnétique en concevant la géométrie du résonateur et la distance entre les résonateurs. (a) Principe de diffusion de champ électromagnétique résultant d'une superposition d'ondes sphériques d'antennes individuelles constituant la métasurface. (b) Les éléments constitutifs peuvent produire une phase qui varie dans la direction azimutale, c'est à dire un front d'onde hélicoïdal. (c)-(d) Exemples de vortex optiques produits par des métasurfaces [Yu 2011].

Les MM électromagnétiques sont communément conçus comme un ensemble d'inclusions ou d'ouvertures artificiellement fabriquées dans un milieu hôte. Cependant, les MM sont distinctement différents des autres structures électromagnétiques artificielles, telles que les cristaux photoniques et les surfaces sélectives en fréquence. La caractéristique distinctive des MM est que les dimensions et la périodicité des éléments de la structure sont significativement plus petites que la longueur d'onde de travail. Leurs propriétés électromagnétiques sont issues de la nature résonante des éléments artificiels individuels [Holloway 2012].

Le changement de paradigme apporté par l'avènement des MM est que l'interaction de l'onde incidente avec des résonateurs sub-longueur d'onde donne la possibilité de contrôler la phase et l'amplitude de l'onde réfléchi ou transmise sur une longueur de propagation de l'ordre de  $\lambda/10$  à l'aide d'une seule couche de MM, appelée également métasurface (MS) [Yu 2011; Ni 2011; Huang 2012; Aieta 2012; Pfeiffer 2013; Yu 2014], comme illustré sur la Fig. 0.1.

Les métasurfaces contrôlent de façon complète les ondes électromagnétiques grâce aux nanostructures sub-longueur d'onde. Les réseaux de nano-antennes ont été efficaces pour contrôler la phase, l'amplitude et la polarisation d'une onde réfléchi et transmise [Yu 2011; Ni 2011]. Des dispositifs novateurs illustrés sur la Fig. 0.2, tels que des lentilles plates ultraminces [Chen 2012; Aieta 2012; Ni 2013], des hologrammes géométriques [Huang 2012; Larouche 2012], et la génération de faisceaux vortex ont été proposés [Yu 2011]. Les tendances actuelles de recherche sur les MS sont axées sur les fonctions d'accordabilité, de commutation, de non-linéarité et de détection. La reconfigurabilité dynamique pourrait mener à des communications de grande capacité, à une formation de faisceaux dynamique, à une imagerie hyper-spectrale et à des optiques adaptatives.

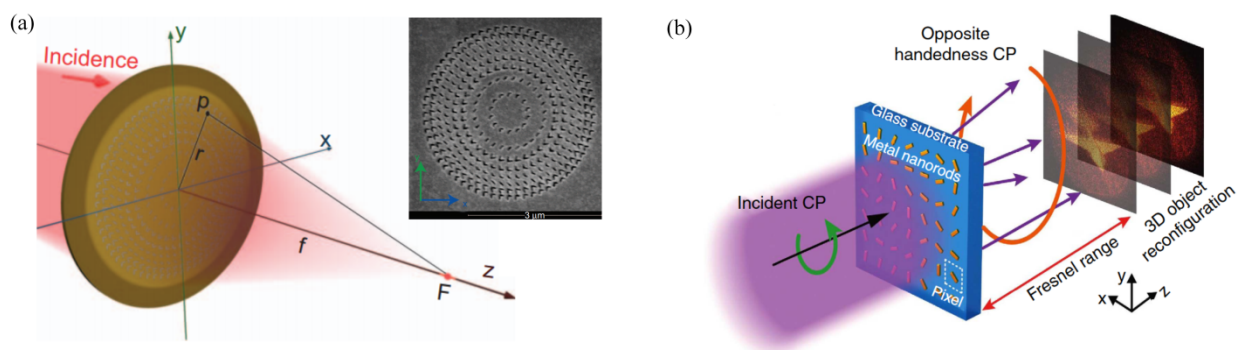


**Fig. 0.2. (a) Conception de meta-lentilles. La lumière diffusée par une nano-antenne  $p$  est focalisée au point focal  $F$ . Les éléments sont disposés de sorte qu'il y ait une interférence constructive au point focal  $F$  de toute la lumière diffusée [Ni 2013]. (b) Conception d'un hologramme à base de métasurface [Huang 2013].**

Le défi consiste à développer le contrôle «à la demande» des méta-atomes individuels aux fréquences micro-ondes. Toutefois, les performances des MSs sont généralement limitées par les pertes [Zheludev 2012; Chen 2012; Larouche 2012; Ni 2013; Ni 2011; Yu 2011; Zheludev 2015; Lin 2013].

La réduction des pertes est donc l'une des questions essentielles à résoudre pour porter les MM et les dispositifs à des applications réelles. L'analyse des méthodes permettant l'amélioration des facteurs de qualité des résonateurs à métamatériaux et des métasurfaces dans les domaines micro-ondes et optique est la principale motivation de ce sujet de thèse.

Le facteur de qualité de certains phénomènes de résonance est limité par des pertes radiatives et non-radiatives dans la structure. Appliqué aux MM et aux MS, les pertes non-radiatives incluent l'absorption dans les milieux hôtes diélectriques et les pertes ohmiques dans les résonateurs métalliques, qui sont couramment utilisés en raison de leur haute conductivité. L'absorption est négligeable en micro-ondes puisque les métaux se comportent comme des conducteurs parfaits. Contrairement au domaine des micro-ondes où les performances des MS sont généralement limitées par des pertes par rayonnement, les pertes non-radiatives jouent un rôle essentiel aux fréquences optiques. Une forte absorption aux fréquences hautes est liée à une faible conductivité. Cependant, la contribution des pertes par rayonnement reste comparable aux pertes par absorption.

Naturellement, la solution principale permettant de réduire les pertes non-radiatives consiste à explorer des matériaux à faibles pertes et à minimiser le volume physique du milieu d'absorption, par exemple en utilisant des métasurfaces minces. Nous pouvons penser aux matériaux tout-diélectriques qui peuvent être employés pour surmonter l'inconvénient des résonateurs métalliques à hautes fréquences. Cependant, cette étude n'est pas consacrée à l'analyse des matériaux optimaux et à la minimisation des pertes par absorption. L'objectif est plutôt de développer des méthodes de suppression des pertes par rayonnement.

Ce travail porte sur les structures plasmoniques où la réponse électromagnétique est basée sur les plasmons de surface, qui sont des oscillations collectives d'électrons libres excités par un champ externe dans un métal. Le phénomène de résonance plasmonique dans les métamatériaux ouvre une large gamme de possibilités d'applications dans des domaines différents. Les plus importantes applications concernent les antennes, les dispositifs d'invisibilité et des systèmes de contrôle de signaux tels que des commutateurs et des filtres. De plus, la sensibilité de la résonance de plasmon à la variation de l'indice de réfraction de l'environnement rend les métamatériaux très utiles pour la détection de biomolécules. La caractéristique essentielle pour

les applications de détection est une résonance avec un fort facteur de qualité et une variation d'intensité abrupte [Anker 2008; Lal 2007; Willets 2007; Zhang 2008]. Cependant, dû à son faible facteur de qualité causé par des pertes radiatives élevées, la résonance de plasmon n'est pas en mesure de présenter les propriétés de détection. Les nombreuses études consacrées aux méthodes de réduction de pertes radiatives peuvent être classifiées en trois catégories, qui se différencient dans le mécanisme utilisé pour rendre étroite la réponse spectrale en transmission ou en réflexion.

Analogie classique de la transparence électromagnétiquement induite. La méthode est basée sur l'interférence destructive de type Fano dans un système d'éléments résonants couplés qui conduit à l'apparition d'une fenêtre de transmission (réflexion) étroite au milieu d'une large bande de réflexion (transmission).

Cavités Fabry-Perot à base de métasurfaces. Les propriétés de haute réflexion proche de la fréquence de résonance des métasurfaces sont utilisées pour concevoir une cavité électromagnétique formée par deux métasurfaces et affichant un facteur de qualité élevé pour les modes Fabry-Perot.

Amélioration directe des facteurs de qualité des résonateurs. Le rétrécissement de la réponse spectrale est réalisé par une réduction des pertes d'absorption et/ou de rayonnement. Cette méthode est principalement liée à l'excitation de modes d'ordre supérieur qui peuvent fournir des caractéristiques de résonance plus étroites que le mode fondamental.

Le phénomène de la transparence électromagnétiquement induite est généralement associé à l'excitation des modes sombres [Liu 2009; Prodan 2003; Chiam 2009]. Dans ce contexte, les modes sombres ne peuvent pas être directement excités. Cependant, ils peuvent être obtenus à partir de l'hybridation de modes induite par un couplage champ proche très fort entre différents éléments [Lukyanchuk 2010]. Le mode sombre est caractérisé par de faibles pertes radiatives et représente l'excitation d'oscillations déphasées de courant. Par conséquent, de tels modes se manifestent par une résonance très étroite par rapport aux modes clairs. Cependant, le mécanisme d'hybridation est très sensible à la variation de la distance séparant les éléments et, donc aux tolérances et imperfections de fabrication. Cela peut rendre l'ingénierie de modes sombres assez compliqué, en particulier dans le domaine de l'optique. Dans le cadre de cette thèse, un mécanisme différent pour l'excitation de mode sombre est proposé. Il consiste en une adaptation de symétrie de l'élément résonant et du champ électromagnétique incident. Une structure de résonateur appropriée qui correspond à la symétrie des champs électrique et magnétique nous permet d'obtenir une résonance de mode sombre dans un résonateur individuel

par un couplage direct avec le champ incident et de ce fait ne dépendant pas de l'hybridation de modes. Ce type de mécanisme assouplit fortement le processus de fabrication dans le domaine optique pour l'obtention de résonances à fort facteur qualité. De plus, cette méthode peut être exploitée pour obtenir une réponse magnétique efficace avec une contribution réduite du dipôle électrique, particulièrement pour la gamme de fréquences optiques.

Dans ce travail, nous nous intéressons également aux phénomènes de résonance dans des systèmes plus complexes de résonateurs couplés qui se traduisent par l'apparition de caractéristiques spectrales ultra-étroites. L'interaction est déterminée par la distance de séparation entre les éléments résonants et leur arrangement. Deux mécanismes de couplage fondamentalement différents peuvent être définis par rapport à la distance de séparation entre les éléments : le couplage par le champ proche et le couplage par le champ lointain. Le couplage champ proche peut provoquer un décalage de la fréquence de résonance plasmon ou une hybridation de modes entraînant l'apparition de deux modes normaux. La résonance étroite de Fano, résultant de l'interférence de modes, peut être observée à proximité du mode antisymétrique. Le couplage de champ proche diminue avec une distance de séparation accrue entre deux couches de résonateurs. Quand la distance de séparation devient plus grande que la longueur d'onde de la résonance plasmon, les résonateurs se couplent par le champ lointain en raison de la différence significative de phase du champ électromagnétique pour les éléments. Cela permet d'avoir des modes de cavité ultra-étroits dans le voisinage de la fréquence de résonance plasmon, semblable à la cavité Fabry-Perot classique. Ainsi, la cavité à base de métasurfaces présente des caractéristiques de résonances étroites pour différents régimes d'interaction. L'objectif est de chercher la configuration géométrique optimale et la distance de séparation de la cavité à base de métasurfaces, en utilisant des outils théoriques et expérimentaux adéquats, pour des applications de détection.

L'objectif de cette thèse est d'explorer des solutions innovantes visant à concevoir des métasurfaces avec des réponses spectrales hautement sélectives pour des applications liées aux capteurs. Le manuscrit est organisé en six chapitres. Le premier chapitre présente une introduction générale sur les motivations de cette thèse. Le deuxième chapitre présente une analyse approfondie sur l'état de l'art concernant l'excitation de résonances très étroites dans les métasurfaces. Ce chapitre présente notamment les approches présentées dans la littérature, permettant d'obtenir des résonances à fort facteur de qualité dans le domaine de MS. Dans le chapitre 3, le mécanisme d'excitation direct de mode sombre dans le résonateur individuel par une adaptation de symétrie est proposé. Les chapitres 4 et 5 sont dédiés à l'excitation de la

résonance de Fano dans le système des résonateurs couplés identiques. Les conclusions finales et des perspectives sur des travaux futurs sont présentées dans le chapitre 6.

## References

- [Aieta 2012] F. Aieta et al., 2012. “Out-of-Plane Reflection and Refraction of Light by Anisotropic Optical Antenna Metasurfaces with Phase Discontinuities”. *Nano Letters*, 12, pp.1702-1706.
- [Chen 2012] X. Chen et al., 2012. “Dual-polarity plasmonic metalens for visible light”. *Nature Communications*, 3, p.1198.
- [Holloway 2012] C.L. Holloway et al., 2012. “An Overview of the Theory and Applications of Metasurfaces: The Two-Dimensional Equivalents of Metamaterials”. *IEEE Antennas and Propagation Magazine*, 54, pp.10-35.
- [Huang 2012] C. Huang et al., 2012. “Asymmetric electromagnetic wave transmission of linear polarization via polarization conversion through chiral metamaterial structures”. *Physical Review B*, 85.
- [Larouche 2012] S. Larouche et al., 2012. “Infrared metamaterial phase holograms”. *Nature Materials*, 11, pp.450-454.
- [Lin 2013] J. Lin et al., 2013. “Nanostructured Holograms for Broadband Manipulation of Vector Beams”. *Nano Letters*, 13, pp.4269-4274.

- [Ni 2011] X. Ni et al., 2011. “Broadband Light Bending with Plasmonic Nanoantennas”. *Science*, 335, pp.427-427.
- [Ni 2013] X. Ni, S. Ishii, A.V. Kildishev & V.M. Shalaev, 2013. “Ultra-thin, planar, Babinet-inverted plasmonic metalenses”. *Light: Science*
- [Pendry 1996] J.B. Pendry, A.J. Holden, W.J. Stewart & I. Youngs, 1996. “Extremely Low Frequency Plasmons in Metallic Mesostructures”. *Physical Review Letters*, 76, pp.4773-4776.
- [Pfeiffer 2013] C. Pfeiffer & A. Grbic, 2013. “Metamaterial Huygens’ Surfaces: Tailoring Wave Fronts with Reflectionless Sheets”. *Physical Review Letters*, 110.
- [Yu 2014] N. Yu & F. Capasso, 2014. “Flat optics with designer metasurfaces”. *Nature Materials*, 13, pp.139-150.
- [Yu 2011] N. Yu et al., 2011. “Light Propagation with Phase Discontinuities: Generalized Laws of Reflection and Refraction”. *Science*, 334, pp.333-337.
- [Zheludev 2015] N.I. Zheludev, 2015. “Obtaining optical properties on demand”. *Science*, 348, pp.973-974.
- [Zheludev 2012] N.I. Zheludev & Y.S. Kivshar, 2012. “From metamaterials to metadevices”. *Nature Materials*, 11, pp.917-924.



# Chapter 1.

## General Introduction and Context of Study

Metamaterials (MMs) are artificial composite materials designed to display particularly specified electromagnetic properties.

The concept of metamaterials introduced after the work of Sir J. Pendry in 1996 [Pendry 1996] is now in its broadest sense an umbrella for artificial substances, whose properties are extended beyond the limits provided by nature and resulting in something with completely different properties from the materials employed; for example, materials with a negative refractive index, with pronounced magnetic properties in the optical domain, cloaking devices, etc. The current research on metamaterials symbolizes the beginning of the era, in which electromagnetic rays and light will deeply influence physical and technical processes everywhere in everyday life and industry.

Electromagnetic MMs are commonly engineered as an array of artificially fabricated inclusions or apertures in a specified host medium. However, MMs are distinctly different from other artificial electromagnetic structures, such as photonic crystals and frequency selective surfaces. The distinctive feature of MMs that makes them different from other artificial materials is that the dimensions and the periodicity of scattering elements of structure are significantly smaller than the operation wavelength. Their electromagnetic properties stem for essential from the resonant nature of individual artificial elements [Holloway 2012].

The change of paradigm brought by the advent of MMs is that the interaction of incoming wave with localized sub-wavelength size resonators brings the possibility to control the phase and the amplitude of reflected or transmitted wave on a propagation length of the order of  $\lambda/10$  by using a single layer of MMs, called also metasurface (MS) [Yu 2011; Yu 2014; Ni 2011; Aieta 2012; Huang 2012; Pfeiffer 2013].

Metasurfaces fully control electromagnetic waves thanks to inner sub-wavelength scale nanostructures. Arrays of nano-antennas were effective at controlling the phase, amplitude, and polarization of both a reflected and transmitted wave [Ni 2011; Yu 2011]. Innovative elements, such as ultrathin flat lenses [Chen 2012; Ni 2013; Aieta 2012], computer-generated geometric holograms [Huang 2012; Larouche 2012], and wave-plate vortex-beam generation were reported [Yu 2011] (Fig.1.1-1.2).

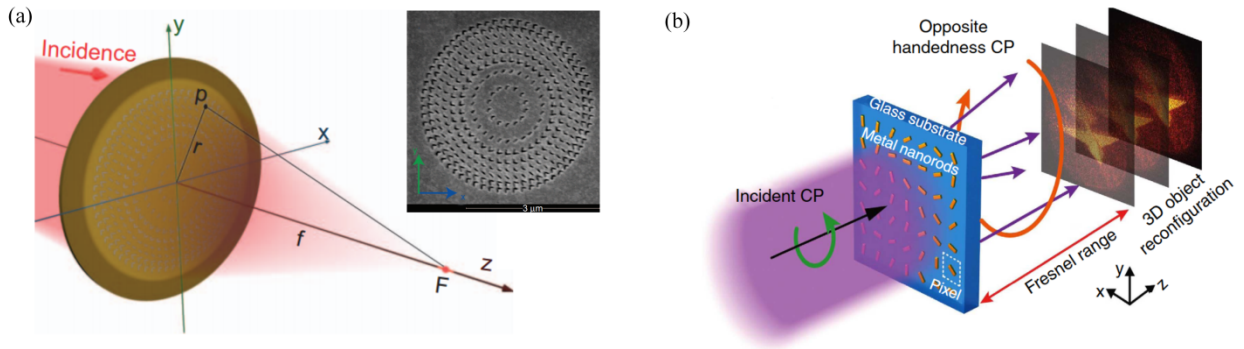


**Fig.1.1. (a) Design principles of the metalenses. Light scattered by an arbitrary individual nano-antenna  $p$  focuses at a focal point  $F$ . Elements are arranged such that all scattered light constructive interfere at point  $F$  [Ni 2013]. (b) Metasurface hologram design [Huang 2013].**

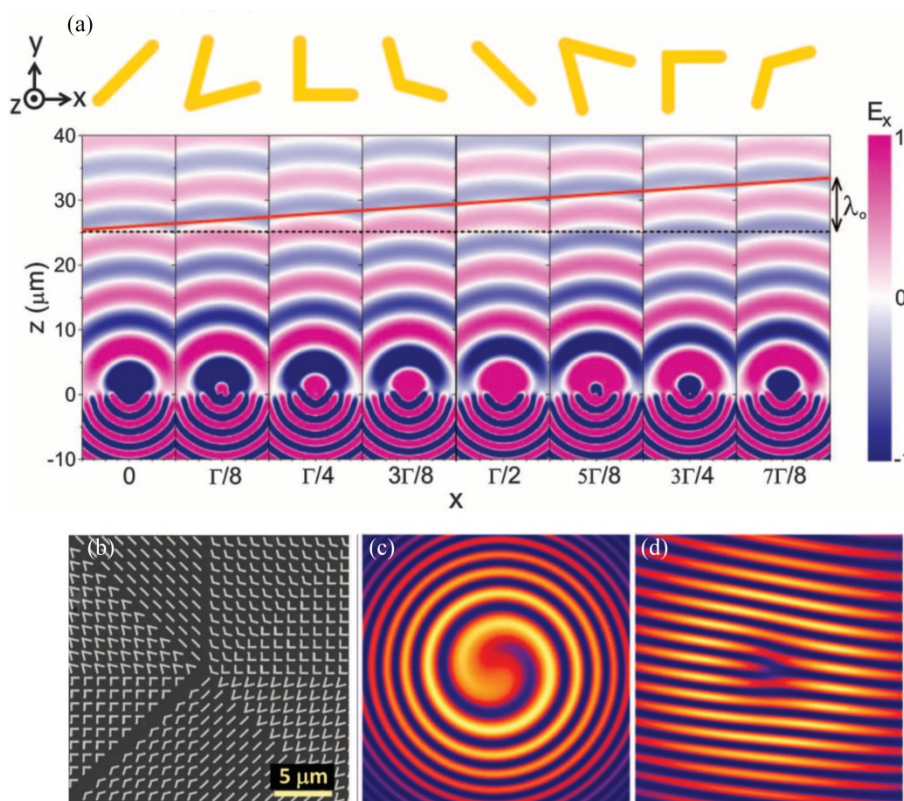


**Fig. 1.2. MSs control amplitude, phase and polarization state of electromagnetic wave by designing a resonator shape and separation distance between neighbours. (a) Principle of electric field scattering as a result of superposition of spherical wave from the individual antennas composing the array for  $y$ -polarized plane wave excitation at normal incidence. (b) Arranged elements can produce azimuthally varying phase difference i.e. helicoidal scattered wavefront. (c)-(d) examples of optical vortices obtained by using MSs [Yu 2011].**

The current research trends on MSs are focused on tunable, switchable, nonlinear, and sensing functionalities. Dynamic reconfigurability could lead to high-capacity communications, dynamic beam shaping, hyperspectral imaging, and adaptive optics. The challenge is to develop “on-demand” control of individual metamolecules operating at GHz frequency range. However, the performances of MSs requiring high quality resonators are usually limited by the losses [Zheludev 2012; Chen 2012; Larouche 2012; Ni 2013; Ni 2011; Yu 2011; Zheludev 2015; Lin 2013].

The reduction of losses is thus one of the essential issues to be solved to bring MMs and metadevices to real life applications. The explorations of the methods enabling the improvement of the quality factors of MMs and MSs resonators in the microwave and optical domains has motivated the subject of the present PhD work study.

As known the quality factor of some resonance phenomenon is limited by radiative and non-radiative losses in the structure. Applied to MMs and MSs, the last one includes absorption in dielectric host media and ohmic losses in a metallic resonator, which are commonly used due to their high conductivity. Microwave region is characterized by negligibly small absorption since metals behave as perfect conductor. In contrast to the microwave domain, where MSs performances are generally limited by radiation losses, at optical frequency non-radiative losses play an essential role. Strong absorption for the high frequencies is related to low conductivity, intra-band and inter-band electron transitions. However, the contribution of radiation losses remains comparable with absorption losses.

An obvious solution to reduce non-radiative losses consists in exploring low loss materials and minimization of physical volume of absorption medium, for instance by using thin MSs. Recent progress in the area of MMs and MSs is related to the investigation of all-dielectric materials that are promising candidates to overcome some issues inherent to metallic resonators at high frequencies. This study is not however devoted to the analysis of optimal materials and minimization of absorption losses. The aim is rather to develop methods providing either a suppression by design of radiative losses or circumventing issues related to their negative impact.

To summarize the objective of the PhD work is to explore innovative solutions that allow achieving a high selectivity of MSs spectral response in view of sensing applications. The manuscript is organized as follows. The critical analysis of the existing approaches employed for the tailoring of the MSs spectral response aiming the obtaining of narrow band spectral features is presented in the Chapter 2. Chapter 3 is devoted to the presentation and analysis of direct dark

mode excitation mechanism in individual resonator through symmetry matching. Chapters 4 and 5 are dedicated to the analysis of Fano resonance excitation in the system of identical coupled resonators. Final conclusions and outlooks for future work are presented in Chapter 6.

## References

- [Aieta 2012] F. Aieta et al., 2012. “Out-of-Plane Reflection and Refraction of Light by Anisotropic Optical Antenna Metasurfaces with Phase Discontinuities”. *Nano Letters*, 12, pp.1702-06.
- [Chen 2012] X. Chen et al., 2012. “Dual-polarity plasmonic metalens for visible light”. *Nature Communications*, 3, p.1198.
- [Holloway 2012] C.L. Holloway et al., 2012. “An Overview of the Theory and Applications of Metasurfaces: The Two-Dimensional Equivalents of Metamaterials”.
- [Huang 2012] L. Huang et al., 2012. “Dispersionless Phase Discontinuities for Controlling Light Propagation”. *Nano Letters*, 12, pp.5750-55.
- [Huang 2013] L. Huang et al., 2013. “Three-dimensional optical holography using a plasmonic metasurface”. *Nature Communications*, 4.
- [Larouche 2012] S. Larouche et al., 2012. “Infrared metamaterial phase holograms”. *Nature Materials*, 11, pp.450-54.
- [Lin 2013] J. Lin et al., 2013. “Nanostructured Holograms for Broadband Manipulation of Vector Beams”. *Nano Letters*, 13, pp.4269-74.
- [Ni 2011] X. Ni et al., 2011. “Broadband Light Bending with Plasmonic Nanoantennas”. *Science*, 335, pp.427-27.
- [Ni 2013] X. Ni, S. Ishii, A.V. Kildishev & V.M. Shalaev, 2013. “Ultra-thin, planar, Babinet-inverted plasmonic metalenses”. *Light: Science*
- [Pendry 1996] J.B. Pendry, A.J. Holden, W.J. Stewart & I. Youngs, 1996. “Extremely Low Frequency Plasmons in Metallic Mesostructures”. *Physical Review Letters*, 76, pp.4773-76.

- [Pfeiffer 2013] C. Pfeiffer & A. Grbic, 2013. “Metamaterial Huygens’ Surfaces: Tailoring Wave Fronts with Reflectionless Sheets”. *Physical Review Letters*, 110.
- [Yu 2014] N. Yu & F. Capasso, 2014. “Flat optics with designer metasurfaces”. *Nature Materials*, 13, pp.139-50.
- [Yu 2011] N. Yu et al., 2011. “Light Propagation with Phase Discontinuities: Generalized Laws of Reflection and Refraction”. *Science*, 334, pp.333-37.
- [Zheludev 2015] N.I. Zheludev, 2015. “Obtaining optical properties on demand”. *Science*, 348, pp.973-74.
- [Zheludev 2012] N.I. Zheludev & Y.S. Kivshar, 2012. “From metamaterials to metadevices”. *Nature Materials*, 11, pp.917-24.

## Chapter 2.

# Dark Mode and Fano Resonance: Analysis on State-of-arts

The realization of MSs and MMs with sharp spectral features in view of filtering or sensing applications motivated an important amount of research devoted to the achievement of this goal. The numerous studies reported on this subject in the literature can be broadly classified into three categories, differing according to the mechanism used for narrowing the bandwidth of the spectral response either in transmission or reflection:

Classical analog of Electromagnetically Induced Transparency. The method is based on the Fano type destructive interference in a system of coupled resonant elements that leads to the opening of a narrow transmission (reflection) window in the middle of a wide reflection (transmission) band.

Fabry-Perot metasurface cavities. The high reflection properties of MSs near the resonance frequency are used to build an electromagnetic cavity formed by two MSs displaying high finesse factor for Fabry-Perot modes.

Direct improvement of the resonators' quality factors. The linewidth narrowing is achieved by means of reduction of absorption and/or radiation losses.

The fundamentals as well as the critical analysis of advantages and drawbacks of the listed methods are detailed in the following.

### 2.1. Classical analog of Electromagnetically Induced Transparency

Fundamental of EIT

The concepts of dark mode, Fano resonance and EIT were initially developed in atomic physics. We will start with introduction of the basis of these phenomena to further extend them to the area of electromagnetic MMs and MSs.

Describing an interaction of matter with electromagnetic radiation usually relates to phenomenon of resonance - enhancement of the response of vibrating system under external force at natural frequency. Symmetric spectral response known as a Lorentzian resonance is observed, for example, in harmonic oscillator under periodic force. In contrast, the Fano resonance exhibits an asymmetric profile. Wood [Wood 1935] was first who observed asymmetric behavior of the

spectrum of metallic diffraction gratings. Later, Beutler [Beutler 1935] noticed the asymmetric absorption peaks in the spectral lines of noble gases. Trying to explain these phenomena, Ugo Fano [Fano 1961; Fano 1936] developed his approach based on interference of discrete states and continuum states with similar energy. In metallic gratings under particular conditions propagating radiation interacts with excited surface leaky waves that lead to Fano resonance. Similar result is observed in atoms due to the interference of discrete auto-ionized state with a continuum. It should be noted that such interference is general effect thus, Fano resonance can be found in many different systems: Bose-Einstein condensate, Josephson junction, photonic crystal slabs, photonic waveguides and Aharonov-Bohm interferometer [Miroshnichenko 2010].

To understand intuitively the mechanism of Fano resonance the classical model of coupled oscillators can be considered (Fig.2.1) [Alzar 2002; Joe 2006]. The dynamic of two coupled oscillators with resonant frequencies  $\omega_1$  and  $\omega_2$ , damping factors  $\gamma_1$  and  $\gamma_2$ , and driven by external harmonic forces  $f$  applied to the first resonator is described by a system of motion equations:

$$\begin{aligned} \ddot{x}_1 + \gamma_1 \dot{x}_1 + \omega_1^2 x_1 + \kappa x_2 &= f e^{i\omega t} \\ \ddot{x}_2 + \gamma_2 \dot{x}_2 + \omega_2^2 x_2 + \kappa x_1 &= 0 \end{aligned} \quad (2.1)$$

where  $\kappa$  is a coupling between two oscillators. The complex steady-state solutions for the displacement of the oscillators are periodic and can be written as  $x_1 = c_1 e^{i\omega t}$  and  $x_2 = c_2 e^{i\omega t}$ , where  $c_1$  and  $c_2$  are the complex amplitudes:

$$\begin{aligned} c_1 &= \frac{(\omega_2^2 - \omega^2 + i\gamma_2\omega)}{(\omega_1^2 - \omega^2 + i\gamma_1\omega)(\omega_2^2 - \omega^2 + i\gamma_2\omega) - \kappa^2} f \\ c_2 &= \frac{\kappa}{(\omega_1^2 - \omega^2 + i\gamma_1\omega)(\omega_2^2 - \omega^2 + i\gamma_2\omega) - \kappa^2} f \end{aligned} \quad (2.2)$$

The phases of the oscillators are determined from:

$$c_1(\omega) = |c_1(\omega)| e^{-i\varphi_1(\omega)}, \quad c_2(\omega) = |c_2(\omega)| e^{-i\varphi_2(\omega)}$$

The frequency response of the first oscillator shown in Fig. 2.2b demonstrates two resonances: a broader one centered at  $\omega_1$  and a narrower with more or less pronounced asymmetric shape centered at  $\omega_2$ . The drop in oscillation amplitude  $x_1$  occurring in the vicinity of the resonance frequency  $\omega_2$  is the result of Fano type destructive and constructive interference caused by the coupling between oscillators. As can be seen in Fig. 2.2b in the vicinity of the Fano resonance there appears a  $\pi$ -jump in the phase of the first oscillator. Below that resonant frequency, both oscillators are in phase, while above the resonant frequency they oscillate out of phase.

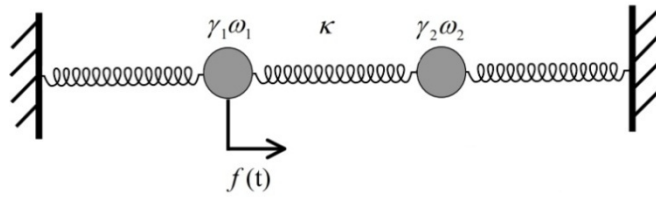


Fig. 2.1. Classical model of two coupled mechanical oscillators [Alzar 2002].

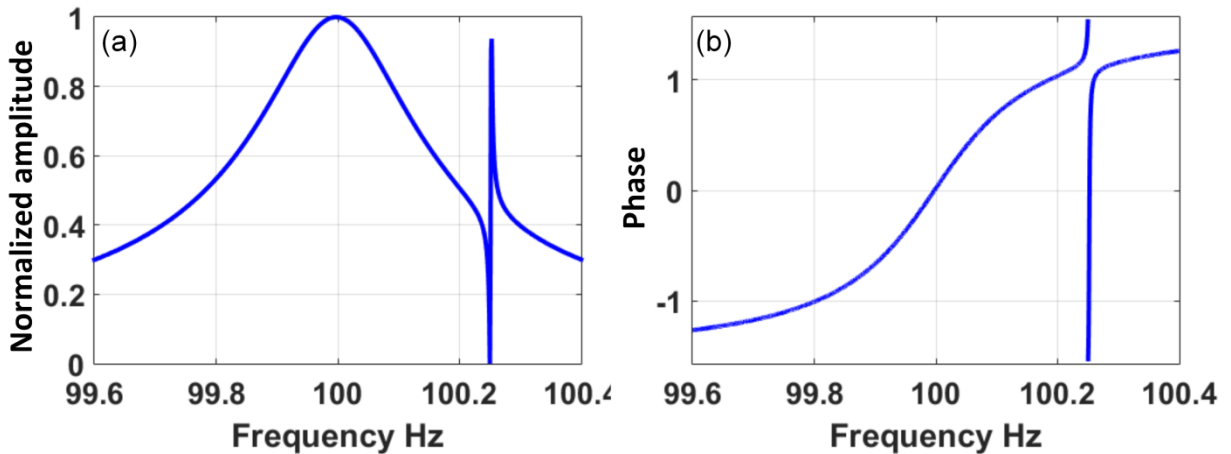
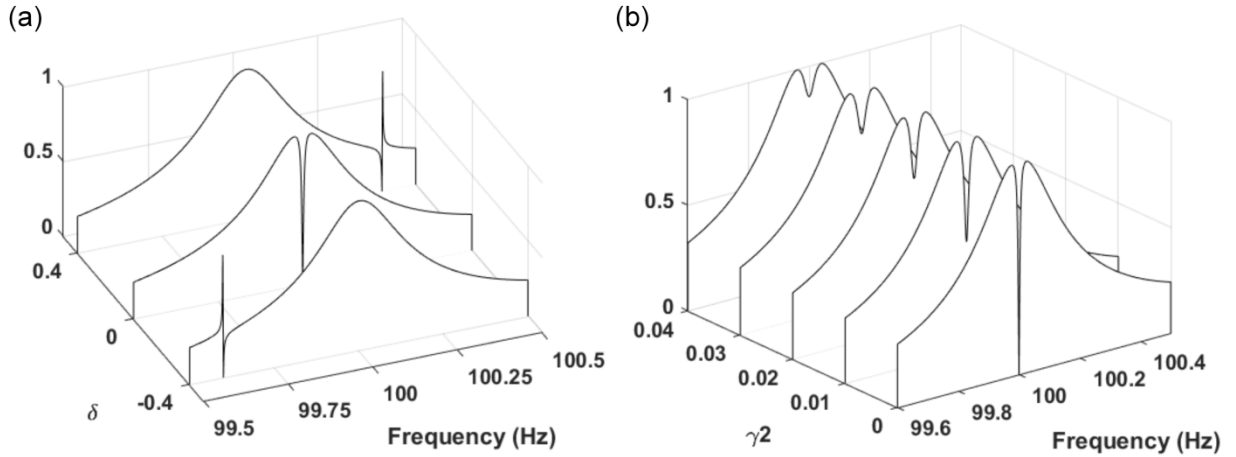


Fig. 2.2. (a) Normalized amplitude as a function of frequency for the driven oscillator in the system of coupled resonators with resonant frequencies  $\omega_1 = 100$  Hz,  $\omega_2 = 100.25$  Hz, damping  $\gamma_1 = 0.25$  Hz,  $\gamma_2 = 0$ ,  $\kappa = 5$  Hz. (b) Phase characteristic for the first oscillator. Phase change of  $\pi$  occurs at the frequency of asymmetric resonance.

It should be noted, that such a resonant behavior is typical for many systems which can be described by a model of coupled oscillators: RLC contour, mechanical systems with masses and springs or nano-particles coupled through the near field. Owing to simplicity this approach is often used for fitting the response of mechanical or plasmonic systems, exhibiting Fano resonance [Qin 2013; Tassin 2009; Gu 2012; Hu 2016; Lee 2015; Liu 2009].



**Fig. 2.3.** Normalized amplitude  $|c_1|$  of the driven oscillator in the classical coupled oscillators system. (a) Variation of the resonance frequency detuning  $\delta = \omega_1 - \omega_2$  at  $\omega_1 = 100$  Hz,  $\gamma_1 = 0.25$  Hz,  $\gamma_2 = 0$ ,  $\kappa = 5$  Hz. (b) Variation of the damping strength  $\gamma_2$  of the second oscillator at  $\delta = 0$ .

Consider fundamental relations of system parameters which influence the resonance response. Adjusting the resonance frequency detuning  $\delta = \omega_1 - \omega_2$  allows to observe different interference picture (Fig.1.3a). At the zero detuning  $\delta$  extremely narrow dip in resonance response is observed that is similar to the spectrum of EIT - particular case of Fano interference in atomic systems.

It is important to note that efficiency of constructive-destructive interference characteristic for a Fano resonance strongly depends on losses. The impact of the variation of the damping strength of second oscillator  $\gamma_2$  is depicted in Fig. 2.3b. With the increase of the damping strength  $\gamma_2$  the transmission dip almost completely disappears though  $\gamma_2$  is still much lower than  $\gamma_1$ .

Same type of constructive-destructive Fano interference also lies in the origin of Electromagnetically Induced Transparency effect. The difference with respect to the system of coupled classical oscillators is that in atomic physics the phenomenon of EIT is based on quantum interference of transition probabilities. Such effect manifests as an extremely narrow transparency window within a broader Lorentzian absorption profile. Coherent coupling of two different atom ground states with common excited state driven by two lasers leads to Fano-like interference [Fleischhauer 2005]. Initially, the demonstration of EIT was performed in three-level atomic systems. One widely used configuration is depicted in Fig. 2.4. The ground state 2 interacts with the excited state 3 through a pump laser field; the transition 1-2 is a dipole-forbidden transition. When the probe laser frequency is adjusted to transition 1-3 the absorption of probe laser radiation vanishes. In the terms of bare atomic states EIT effect is explained as the

result of an interference of two possible excitation pathways of level 3: directly from the level 1 or indirectly from the level 1 through level 2 due to the strong pump field. To realize the regime of EIT the probe field should be much weaker as compared with the pump field intensity. In such configuration the ground state does not interact with the probe field and is said to be dark [Harris 1997; Gray 1978].

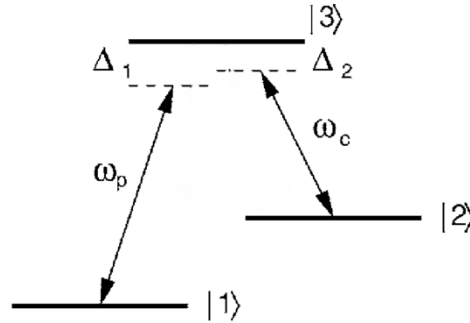


**Fig. 2.4. Energy diagram of a three-level  $\Lambda$ -type atom interacting with two laser beams,  $\omega_p$  and  $\omega_c$  - frequencies of pump and probe laser respectively,  $\Delta_1$  and  $\Delta_2$  is detuning from atomic resonance frequency [Fleischhauer 2005].**

There are several difficulties related to the experimental realization of EIT. For instance the coherent laser light needs to be tuned to a certain energy transition. Moreover, a cryogenic setup or source of magnetic field is often required. The classical analog of EIT offers the opportunity to avoid such experimental difficulties. It should be noted that before considering the demonstration of EIT-effect in plasmonic and MMs systems, this phenomenon was widely investigated by considering classical systems of coupled mechanical [Alzar 2002], electrical[Xu 2006; Litvak 2002], optical [Maleki 2004; Vahala 2003], and acoustic oscillators [Liu 2010]. The principal difference with respect to the atomic systems is the interference of interacting fields instead of the probability of amplitudes. The most important advantage of non-atomic structures for demonstrating classical analogs of EIT effect is the flexibility of resonance frequency which can be engineered by varying the geometry design of resonators.

## 2.2. Plasmonic EIT viewed as bright and dark modes Fano interference

MMs and MSs thus greatly facilitate the realization of classical analogs of Fano interference effect in a wide frequency range spanning from microwave to optics. In metallic MSs the interaction of unit resonant elements with the external electromagnetic field causes collective oscillations of conductivity electrons. In the quasi-electrostatic approximation such systems may be described in terms of the plasmonic eigenmodes interacting with the external field. The Fano

resonance is occurring due to the interference between plasmonic eigenmodes. The eigenmodes with strong dipolar momentum correspond to in-phase oscillation of coupled resonators and are called bright or radiative modes. In contrast, the eigenmodes with low dipolar momentum correspond to (opposite-phase oscillation of coupled resonators and are called dark modes. Such modes weakly couple with external field because of practically zero net dipolar momentum and therefore demonstrate higher quality factor.

One of the methods that found a large use for exciting dark modes consists in breaking the symmetry in a system of coupled resonators. Such breaking enables excitation of antisymmetric currents in the near vicinity of the resonance frequency. The emitted radiation induced by oppositely directed currents is strongly suppressed, leading thus to the appearance of a transparency window in a narrow frequency range. The first experimental demonstration of dark mode excitation by using this approach was made by Fedotov in the microwave domain [Fedotov 2007]. The demonstration was performed by using an array composed of pair of metallic arcs of slightly different length. The polarization of electric field of incident plane wave was directed along the arcs (Fig. 2.5). The narrow maximum observed in the transmission spectrum near 6 GHz corresponds to antiphase current oscillations in the arcs that induce a dipolar magnetic momentum. Such mode is normally inaccessible by using mirror symmetric arcs of equal length because of a zero net dipolar momentum resulting under such an arrangement.

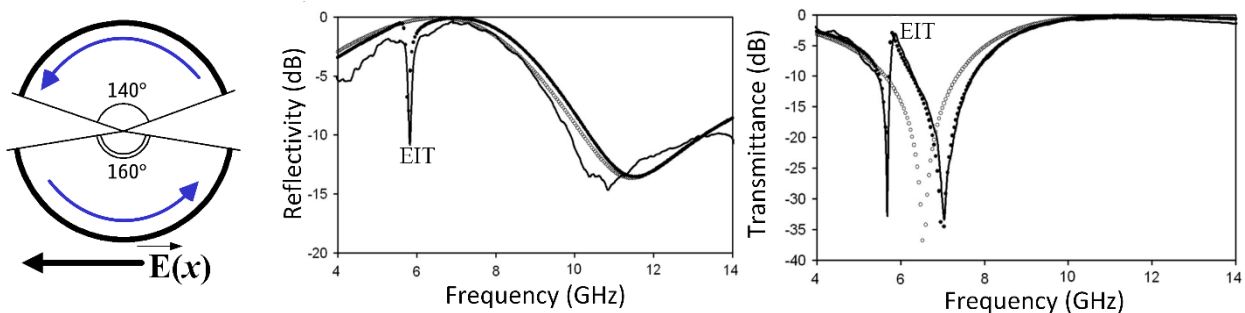


**Fig. 2.5. Schematic design of unit cell and polarization of external field. Transmission and reflection spectra [Fedotov 2007].**

Small time later a theoretical model introducing a general description of an EIT like plasmonic “molecule” was proposed in [Zhang 2008]. The authors have considered an artificial plasmonic molecule consisting of two “atoms”. The bright resonant element represented in Fig. 2.6a corresponds to a super-radiant plasmonic mode  $|a\rangle = \tilde{a}(\omega)\exp(i\omega t)$  that strongly couples with the incident field and is having a broad resonance linewidth. The dark atom represented in Fig.

2.6b corresponds to a sub-radiant plasmonic mode  $|b\rangle = \tilde{b}(\omega)\exp(i\omega t)$ , which weakly couples to the incident light and is having a narrow resonance linewidth. The field amplitude of both elements are described by a system of linearly coupled Lorentzian oscillators:

$$\begin{pmatrix} \tilde{a} \\ \tilde{b} \end{pmatrix} = - \begin{pmatrix} \Delta\omega + i\gamma_a & \kappa \\ \kappa & \Delta\omega + i\gamma_b \end{pmatrix}^{-1} \begin{pmatrix} g\tilde{E}_0 \\ 0 \end{pmatrix} \quad (2.3)$$

where the detuning from resonance  $\Delta\omega = \omega - \omega_0 \ll \omega_0$ , the damping factors of the two resonators satisfy  $\gamma_b \ll \gamma_a \ll \omega_0$ ,  $\kappa$  is the coupling between two atoms and  $g$  is the factor indicating the coupling of superradiant element with the incident electromagnetic field. It is assumed that there is no direct coupling between the dark element and the incident field. Basically this system of differential equation is equivalent to that of coupled mechanical oscillators given by Eq. (2.1)

The amplitude of the dipole response of the bright element is given as:

$$\tilde{a} = \frac{-gE_0(\Delta\omega + i\gamma_b)}{(\Delta\omega + i\gamma_a)(\Delta\omega + i\gamma_b) - \kappa^2} \quad (2.4)$$

The obtained result is in fact only a particular case with respect to the more general solution given by Eq. (2.2). The polarizability of the plasmonic molecule sketched in Fig. 2.6c, is proportional to the amplitude of the bright atom. It follows from Eq. (2.4) that its spectral response is having a form very similar to that in the EIT atomic system. The EIT results from the interference of a narrow discrete resonance with a broad spectral line. The variation with separation distance  $d$  of the plasmonic molecule spectral response is displayed in Fig. 2.6d. At large separation distance where the coupling is weak, the width of the EIT feature is narrow, but the contrast of the pick in the spectral response is small. With the increase of coupling (decrease of separation distance) the contrast of the pick is also increasing but the linewidth of the EIT resonance widens. Such a behavior is due to the fact the increase of the modes coupling decreases the time spent for the energy transfer through the indirect pathway that results in the broadening of the EIT spectral feature related to the interference between the direct and indirect pathways.

By consequence, when considering practical applications, as for instance chemical or biological sensing, requiring simultaneously both a high contrast and a narrow bandwidth, an optimal tradeoff conciliating these requirements needs to be found.

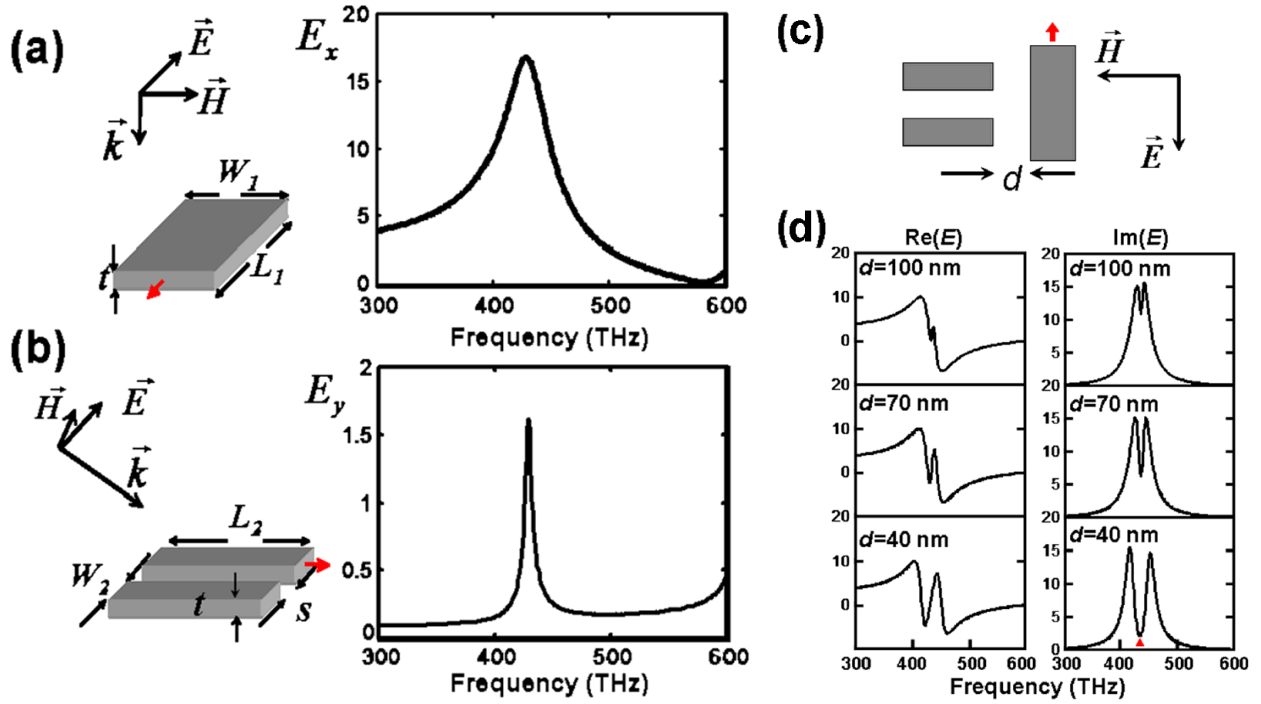


Fig. 2.6. (a) Left: The schematic of a silver optical antenna which functions as a bright atom. Right: The spectral response of an electric field probed at the end of the metal strip. (b) Left: The schematic of a pair of metal strips forming a dark plasmonic atom. Right: The spectral response of an electric field probed at the end of one of the metal strips of the dark atom. (c) The schematic of the plasmonic system composed of a bright element and a dark element with a separation  $d$ , with light incident at the normal direction. (d) The variation with separation distance  $d$  of the real and imaginary parts of an electric field probed at the end of the bright atom metal strip [Zhang 2008].

Since these seminal works [Zhang 2008; Fedotov 2007] a plethora of EIT effect demonstrations exploiting the concept of interacting bright and dark modes have been performed. Several designs based on dolmen type geometry [Gallinet 2011; Liu 2009; Zhang 2008; Gallinet 2013], plasmonic oligomers [Bao 2010; Mirin 2009; Nordlander 2004; Fan 2010], ring-disk nanocavities [Hao 2008; Verellen 2009], nanoshells [Prodan 2003; Wang 2006], asymmetric coupled split-ring resonators [Fedotov 2007; Tassin 2009; Aydin 2010; Singh 2011] or cut wires plasmonic lattices [Christ 2007; Duan 2012; Christ 2008] have been proposed and investigated for EIT characteristics.

Selected examples of plasmonic nanostructures reporting the demonstration of EIT effect in the NIR domain are presented below.

### Symmetry-broken dolmen metamolecules

Following the conceptual precepts elaborated in [Zhang 2008], the experimental demonstration of EIT-like effects in dolmen type structure was performed small time later in [Liu 2009]. The dolmen structure unit cell sketched in Fig. 2.7a consists of a gold bar stacked above two symmetric gold wires. The top gold bar acting as radiative dipole antenna plays the role of the bright mode strongly coupled to the incident light. The bottom gold wire pair acts as a non-radiative quadrupole antenna and represents the dark mode, whose excitation is forbidden for normally incident light. As shown in Fig. 2.7b, the symmetry breaking renders this normally dark mode active and excitable. The EIT is totally absent when the top bar is symmetrically centered with respect to the bottom gold wire pair. The Fano interference and related EIT progressively increases with the lateral displacement  $s$  of the top bar from the central position.

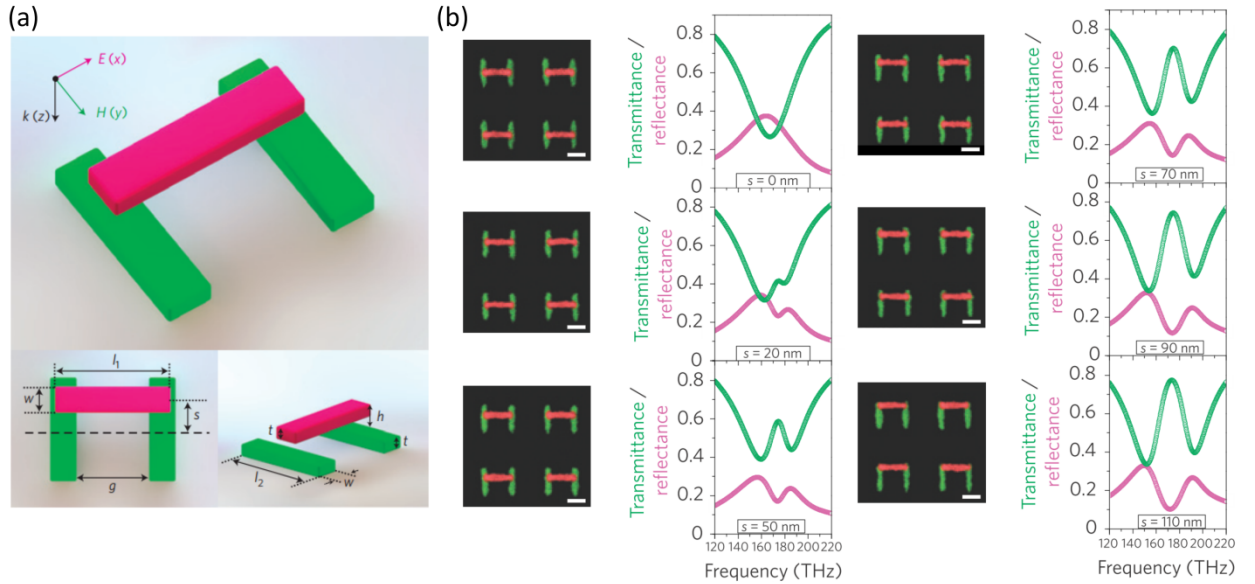


**Fig. 2.7. (a) Schematic of the stacked dolmen structure. (b) Experimental transmittance and reflectance spectra in dependence on lateral displacement  $s$  used as parameter for structure symmetry breaking [Liu 2009].**

The EIT appears as the consequence of interaction between the narrow dark mode and the broad bright mode, as resumed in Fig. 2.8a. The EIT appears as a result of destructive interference between two possible pathways, namely,  $|0\rangle - |1\rangle$  and  $|0\rangle - |1\rangle - |2\rangle - |1\rangle$ . As shown in Fig. 2.8c, the experimentally found transmittance is well fitted by the model of coupled bright and dark modes given by Eq. 2.3. The parameters entering the coupled modes equation are found through the fitting procedure. The evolution of fit parameters as function of the lateral displacement  $s$  corroborates the validity of the model. As it can be observed from Fig. 2.8b, in agreement with

the general physical considerations, the damping strength of both bright and dark mode is practically constant and doesn't depend of the asymmetry parameter. In contrast, the coupling strength displays an approximately linear dependence of the lateral displacement.

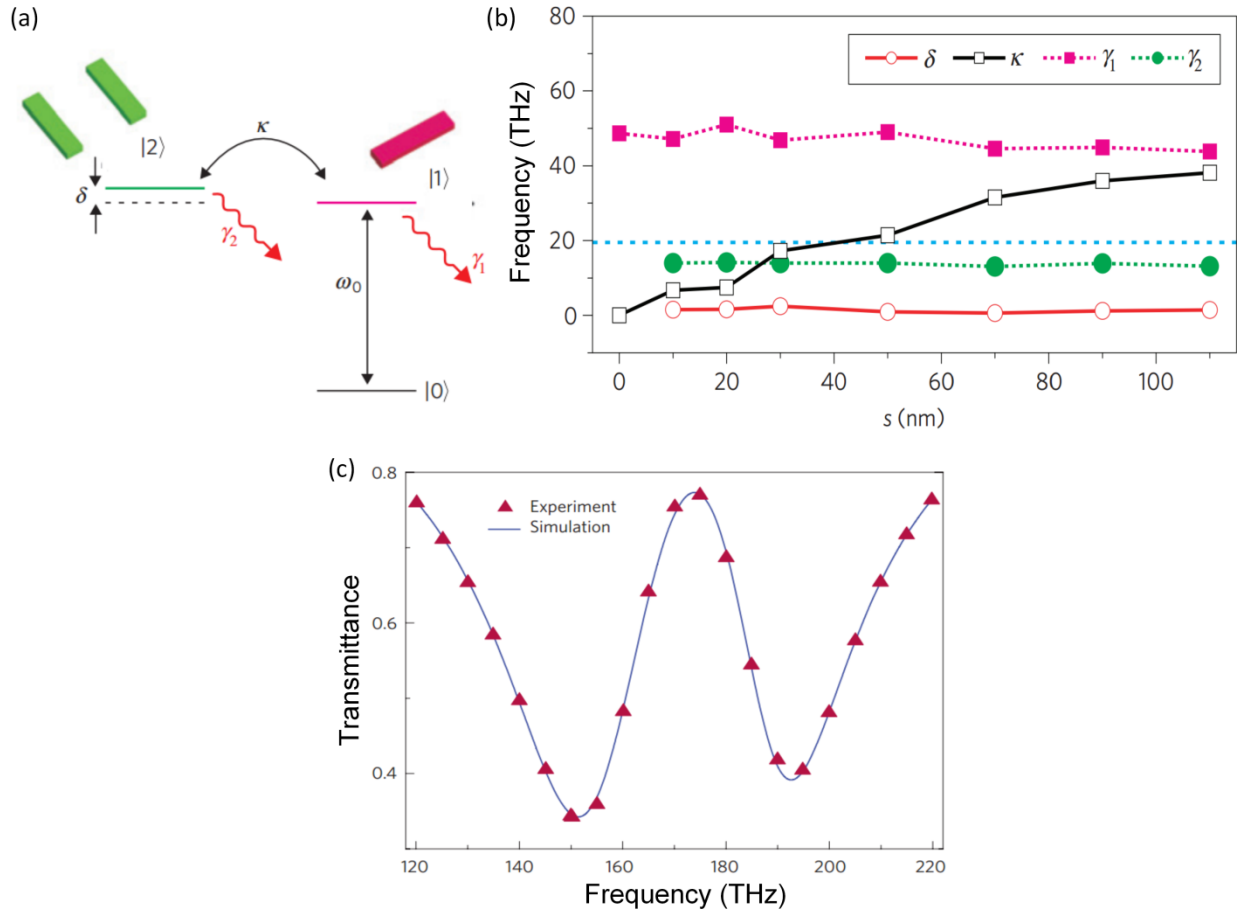


**Fig. 2.8. (a) Plasmonic three-level analog of EIT. The parameter  $\delta$  accounts for the 3THz detuning of the resonance frequency between the dipole and quadrupole elements caused by the imperfection of technological fabrication process [Liu 2009]. (b) Extracted experimental damping and coupling parameters as a function of lateral displacement  $s$ . (c) Experimental transmittance spectrum and fitting curve calculated using the model of Fano-type coupled oscillators; [Lukyanchuk 2010].**

### Symmetry-broken ring-disk nano-cavities

Similar behavior was also reported for system composed of ring-disk nano-cavities [Hao 2008]. The schematic of the structure is represented in Fig. 2.9a. The superradiant anti-bonding dipolar mode acts as the bright resonant element. The rings' quadrupolar electric mode acts as the dark resonant element. Its excitation is forbidden for normally incident light in concentric ring-disk nano-cavities, but becomes allowed when the symmetry of the system is broken. As shown in

Fig. 2.9b, the coupling between bright and dark modes in non-concentric cavity induces an asymmetric Fano resonance in the extinction spectrum similar to the EIT.

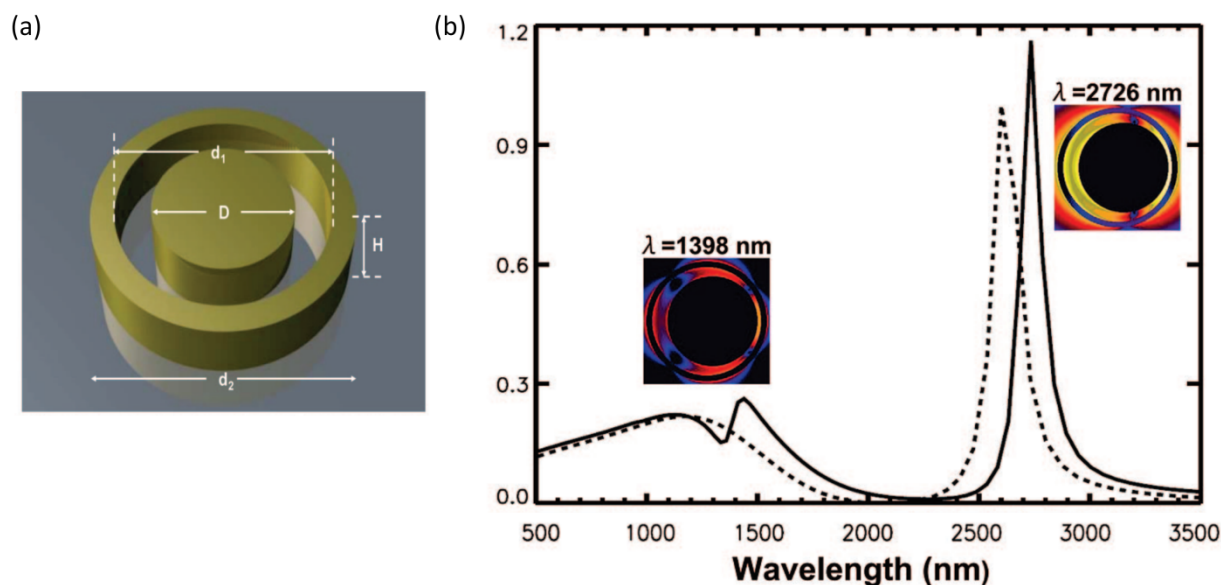


**Fig. 2.9. (a) Schematic of the concentric ring-disk nanocavity. (b) Extinction spectra for Ag concentric ring-disk nanocavity (dashed lines) and symmetry broken non-concentric ring-disk nanocavity (solid lines) [Hao 2008].**

### Plasmonic oligomer clusters

Another family of nanostructures used for the investigation of Fano resonances and EIT is that of plasmonic oligomers [Chuntonov 2011; Fan 2010; Miroshnichenko 2010; Prodan 2003]. In this structure the bright dipolar mode is produced by the collective in-phase oscillation of electrons both of the central and of the outer ring nanoparticles. The dark mode is produced by the anti-phase oscillation of collective charges in the outer ring with respect to the central oligomer nanoparticle. Figures 2.10a and 2.10b show modeling and experimental extinction spectra for a MSs composed of heptamer clusters that is represented in Fig. 2.10d. One important difference with respect to the previous examples of dolmen and coupled disk-ring nanostructures, is that in the case of oligomer clusters the dark mode cannot be assigned to a separate cluster element. It appears instead as the result of near field interaction between plasmonic nanoparticles, a phenomenon known also as hybridization mechanism [Prodan 2003; Nordlander 2004; Christ 2007; Mirin 2009; Bao 2010; Chuntonov 2011; Hentschel 2011]. The plasmon hybridization approach is based on a quasi-electrostatic approximation. The dressed eigenmodes of a system of interacting nanoparticles are considered as a hybridized linear combination of the “primitive” or “diabatic” plasmon modes of the individual particles [Bao 2010; Wang 2006]. In the quantum

mechanical description the hybridization process represents the first order approximation in the perturbation theory approach. As known, in the approximation of weak perturbation the solutions of the perturbed Hamiltonian are found as power series of terms using solutions of unperturbed Hamiltonian.

Another notable difference is that Fano interference between the bright and dark mode doesn't rely on some symmetry-breaking of the oligomer arrangement. However, as illustrated by the Fig. 2.10c, varying the geometrical dimensions of the inner oligomer particle can significantly modify the efficiency of the Fano interference mechanism [Bao 2010]. The generation of a marked Fano resonance in the extinction spectrum was argued by matching the dipole moments of the outer ring and the center particle. In a similar manner as for dolmen or ring-disk coupled structures, the EIT effect is by far more pronounced when the bright dressed mode is highly super-radiant and the dark dressed mode is very sub-radiant.

The provided examples show that the simple model of coupled mechanical oscillators captures the essential features of the Fano interference occurring in plasmonic systems. However, as it was pointed in several works [Frimmer 2012; Gallinet 2011; Lovera 2013] it suffers from a number of approximations detailed below. Furthermore, the parameters entering the coupled mode equation are obtained through a fitting procedure from modeling or experimental scattering spectra instead of being calculated directly from the radiative characteristics of the individual unhybridized modes. This issue motivated scientists to develop novel approaches aiming to achieve the predictive power when considering an *ab initio* design.

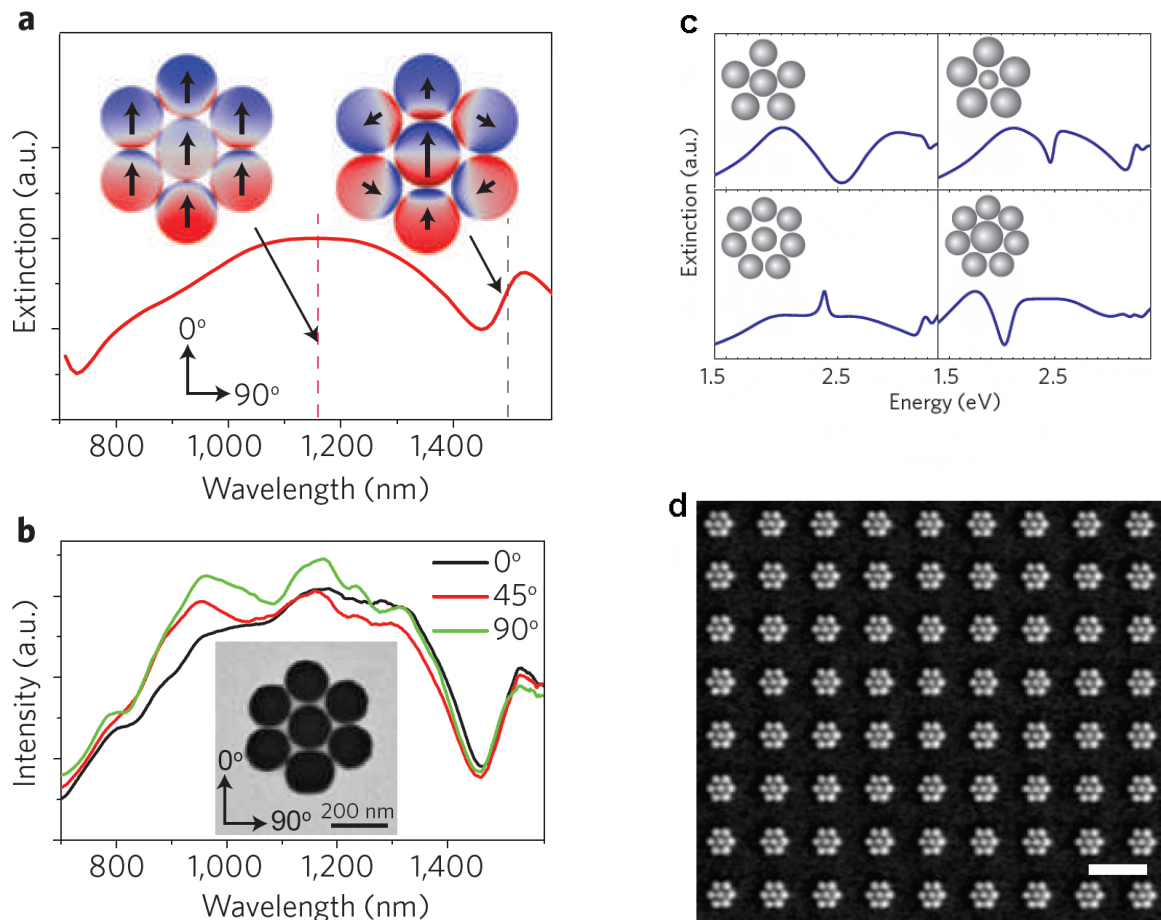


**Fig. 2.10** (a) Calculated dipole amplitudes of the bonding and antibonding collective dipolar plasmon modes in a gold nanoshell heptamer. (b) Experimental scattering spectra of a gold nanoshell heptamer at different incidence angles [Fan 2010]. (c) Impact of the size of the central particle Extinction spectra on the extinction spectra in silver nanosphere hexamers and octumers. (d) Example of technological realization of gold nanodisk heptamers [Hentschel 2011].

### 2.3. Plasmonic EIT revisited

The initial interpretation given to the phenomenon of Fano resonance and EIT in plasmonic systems was based on the concept of interference between a bright and dark mode. The assumption made when using the model of coupled mechanical oscillators is that the incident light is for essential scattered by the bright mode. To verify the validity of this conjecture based on the quasi-electrostatic approach [Forestiere 2013] considered the scattering in a plasmonic system with two or more bright modes. The performed analysis showed that the coupling between at least two bright modes gives rise to Fano-like resonances in the scattering spectrum. The authors have determined in a very clear fashion the contribution of each plasmon mode to the scattering and absorption processes. The obtained results highlighted the fact that the Fano-

type interference and associated with it the plasmonic equivalent of EIT are by far more pronounced as the radiative strengths of both plasmonic modes are similar. As shown in Fig. 2.11, the interference of two modes with very dissimilar radiative strengths increases the asymmetry of the scattering response but the amplitude of EIT is greatly reduced.

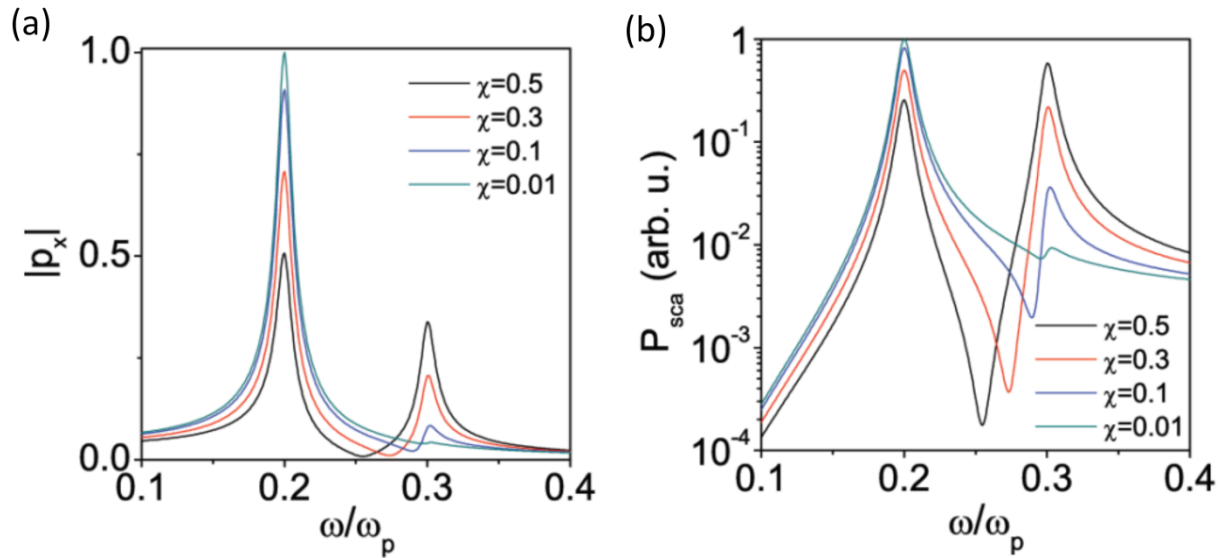


**Fig. 2.11. (a) Magnitude of the x component of the dipole moment  $p$  as a function of  $\omega/\omega_p$  in a plasmonic system with two bright and excitable modes, for different values of the asymmetry factor  $\chi$ . (b) Scattered power spectrum for different values of the asymmetry factor  $\chi$  [Forestiere 2013].**

The apparent contradiction with the previous model of bright-dark mode interaction stems from the fact that Forestiere [Forestiere 2013] considered the interaction of dressed and not diabatic eigenmodes of the plasmonic system.

The considered in [Forestiere 2013] approach is fully consistent with the experimental results reported for oligomers clusters, namely what concerns the influence of the size of the central nanoparticle. Indeed, as illustrated in Fig. 2.10c the Fano interference is by far more pronounced when the size and related with it dipolar moment of the central nanoparticle is matched with that of the outer ring.

Yet one important thing left aside in [Forestiere 2013] analysis is related to the condition of the orthogonality of the eigenmodes. As known, no interference effect should exist in the case of an orthogonal basis of eigenmodes. By consequence it is not clear why Fano interference is observed, especially when dealing with an oligomer assembly having a high degree of symmetry. The initial explanation of this result was based on the non-Hermitian nature of considered system

due to metal related losses. However later results have shown the possibility for occurrence of a Fano resonance in all-dielectric symmetric oligomers [Miroshnichenko 2012].

The relevant explanation of this discrepancy was done in [Hopkins 2013]. As it was pointed by the authors of this publication “The key is that the symmetry approach produces orthogonal modes by definition, whereas the interaction matrix, which describes the coupling between the dipole moments of each particle, is non-Hermitian.” The non-Hermitian character of interaction matrix is due to the presence of both electric and magnetic polarizabilities in the system of interacting particles [Merchiers 2007]. The resulting eigenvectors form a complete set, but are not orthogonal. The fact that the eigenvectors are not orthogonal means that even though the eigenmodes are themselves decoupled; their excitations are coupled. In this case, according to the analysis performed in [Merchiers 2007] “the scattering and absorption cross sections can be written as sums of two contributions. The first is a sum of the individual eigenvalues, and the second is the sum of the double products between different eigenvalues.”

On this basis it was shown in [Hopkins 2013] that the true modes of the oligomer assembly are bright instead of dark and then concluded that “the Fano resonance in this system is explicitly due to the interference between bright modes only, and it does not involve any dark mode.” Another conclusion of great importance to this PhD study was that “generic oligomer structures can be characterized entirely in terms of distinct electric and magnetic collective eigenmodes.”

The non-Hermiticity of interaction matrix is thus the key feature to observe the Fano-type interference of eigenmodes. This non-Hermiticity can be also viewed as the consequence of the open character of the system where the scattered wave corresponds to the resonance-continuum coupling [Lepetit 2010; Wiersig 2006].

One elegant way to take into account the open character of the system was proposed in [Lovera 2013]. The authors of this publication proposed an extended coupled oscillator model (ECO), which consists to introduce in the system of coupled Eq. 2.1 an additional term accounting for the radiative dumping:

$$\begin{aligned}\ddot{x}_1 + \gamma_1 \dot{x}_1 + \omega_1^2 x_1 + \kappa x_2 &= 0.5 \ddot{P}_{tot} + f_1 e^{i\omega t} \\ \ddot{x}_2 + \gamma_2 \dot{x}_2 + \omega_2^2 x_2 + \kappa x_1 &= 0.5 \ddot{P}_{tot} + f_2 e^{i\omega t}\end{aligned}\quad (2.5)$$

where the total dipole moment of the system  $P_{tot} = P_1 + P_2 = \alpha_1 x_1 + \alpha_2 x_2$  is the sum of the dipole momentum of oscillators 1 and 2,  $\alpha_j = f_j / E_{ext}$  are the polarizabilities related to the diabatic plasmon modes.

On the example of plasmonic assembly shown in Fig. 2.12a and made of a gold dipole nanoantenna (yellow) surrounded by two gold nanorods (blue), it was demonstrated that ECO model results (Fig. 1.12d) are in a very good agreement with numerical modeling simulations (Fig. 2.12c) obtained by using Surface Integral Equation method (SIE) as well as with experimental measurements (Fig. 2.12b).

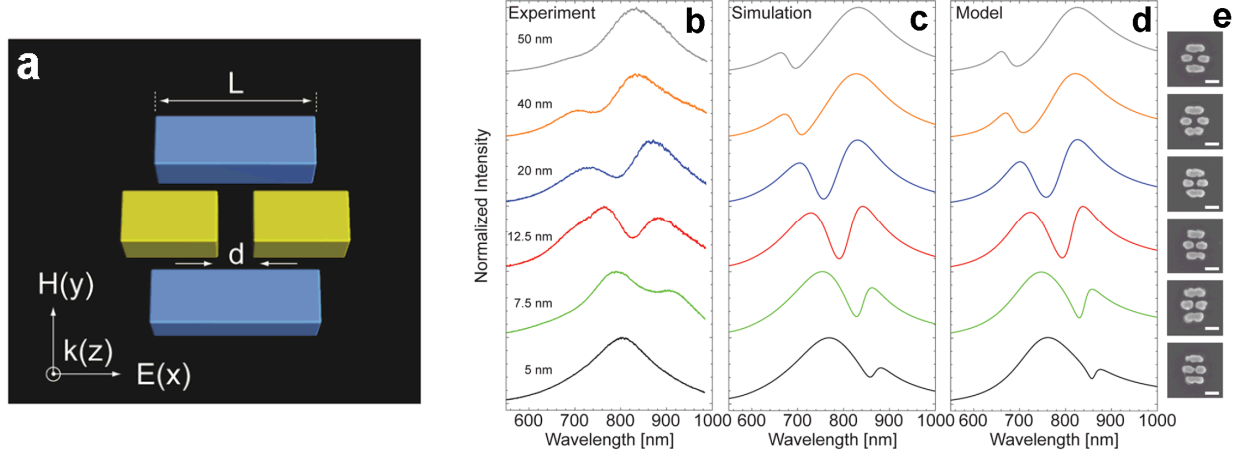


**Fig. 2.12. (a) Schematic of the gold plasmonic structure. (b) Experimental results. (c) SIE scattering simulations. (d) Fit with the ECO model. (e) SEM pictures (scale bar 100 nm) [Lovera 2013].**

However the most elaborated in our opinion approach that takes into account the open character of the system of interacting plasmonic resonators is that using the formalism of the scattering matrix based on the temporal coupled mode theory (TCMT), which was originally proposed by H. Haus for a system of coupled optical resonators in [Haus 1984] and later considerably developed by S. Fan and co-workers [Fan 2003; Ruan 2012; Suh 2004]. Following this approach a resonator system considered to be open and can freely couple to free space through radiation. Propagation of electromagnetic waves through such system occurs via two channels that incorporate direct non-resonance pathway and resonance-assisted pathway. In this formalism and by using same notations as in [Kodigala 2015], the scattering matrix for the system of coupled resonators can be expressed as:

$$S = C + iV[\omega I - H_{\text{eff}}]^{-1} V^\dagger \quad (2.6)$$

where  $C$  is the background scattering which does not interact with resonator and accounts also for the higher order resonances far away from considered frequency range.  $V$  is the coupling between radiation and resonator,  $H_{\text{eff}}$  - effective Hamiltonian which can be described as:

$$H_{eff} = H_0 + i\frac{1}{2}VV^\dagger + i\Lambda_L \quad (2.7)$$

Eigenvalues of  $H_0$  represents the discrete resonator states, being Hermitian matrix. The second term is the coupling between radiation and discrete states and the third term involves extraneous losses. Owing to the presence of latter terms the effective Hamiltonian become non-Hermitian and possesses non-orthogonal basis of eigenmodes. The essential feature of this approach is that the Hamiltonian  $H_{eff}$  takes into account both coupling of eigenmodes to each other and to the free space.

The great advantages for using this method is that all coefficients entering Eq. 2.6 and 2.7 can be expressed with a limited number of parameters in terms of resonators frequencies, damping factors and near field coupling coefficients. Furthermore, this approach can be also used to describe the behavior of more complex arrangement of interacting resonators where in addition retardation effects should be taken into account, as it is the case for plasmonic type Fabry-Perot micro-cavities detailed below. It is namely this formalism of TCMT based scattering matrix and effective Hamiltonian that was used for the following in this PhD study.

## 2.4. Fabry-Perot metasurface cavities

Plasmonic type Fabry-Perot cavities formed by two plasmonic MSs are offering additional opportunities for the spectral response engineering. In the microwave domain most of the studies on this topic were devoted to the use of subwavelength resonant cavities for antennas applications [Ratni 2017]. While concerning the optical domain, the main interest to the study of MSs micro-cavities was motivated by their use as narrow band Fabry-Perot filters for sensing applications [Ameling 2010; Ameling 2012]. In both cases, as shown in Fig. 2.13a, the principle used to shrink the cavity length is based on the additional phase shift induced by the MSs. As evident from the Fig. 2.13b, a maximal sharpness of the Fabry-Perot cavity spectral response is achieved in the near vicinity of the MSs resonance frequency.

Most frequently the operation of such Fabry-Perot cavities is performed when the separation distance between MSs is of the order of wavelength. Generally such a distance is high enough to neglect the near field coupling effects between MMs resonant elements. This situation corresponds to the far-field coupling regime between MSs. Things become more complex when deeply subwavelength cavities are considered and the near field coupling effects are predominant. However such an operation regime may be of particular interest for sensing

applications since EIT can be observed in this case, as illustrated by Figs. 1.14-1.16 [Papasimakis 2008; Kanjanasit 2013; Kodigala 2015].

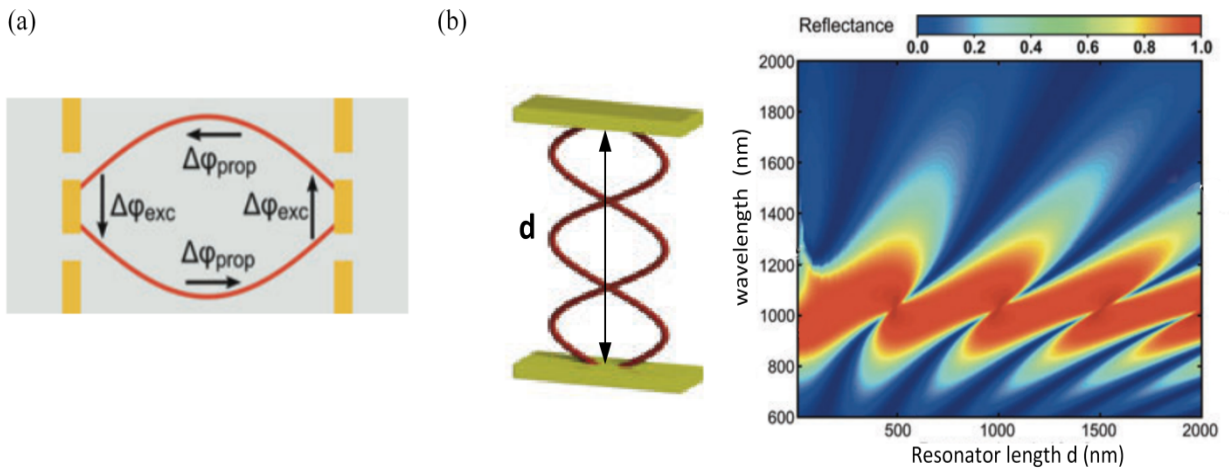


**Fig. 2.13. (a) Phase shifts for Fabry-Perot cavities formed by resonant metasurfaces. (b) Reflectance spectra of MSs confined Fabry-Perot cavities with varying resonator length  $d$ . [Ameling 2012].**

However, despite the very numerous studies on the double layered MSs performed either in the microwave or the optical domain, a global insight on the conditions to be met for the observation of Fano interference in coupled MSs was missing when this PhD study was initiated. For instance there is a divergence on the reported results whether the MSs should be aligned as in [Kanjanasit 2013] (Fig. 2.14) or rather misaligned [Papasimakis 2008; Kodigala 2015] (Figs. 2.13, 2.15). Furthermore, it is not clear what the optimal separation distance between MSs is, and more generally, what are the advantages for using near-field coupled MS cavities instead of far-field coupled MS cavities. Filling this gap and providing answers to these questions was the objectives of this PhD work.

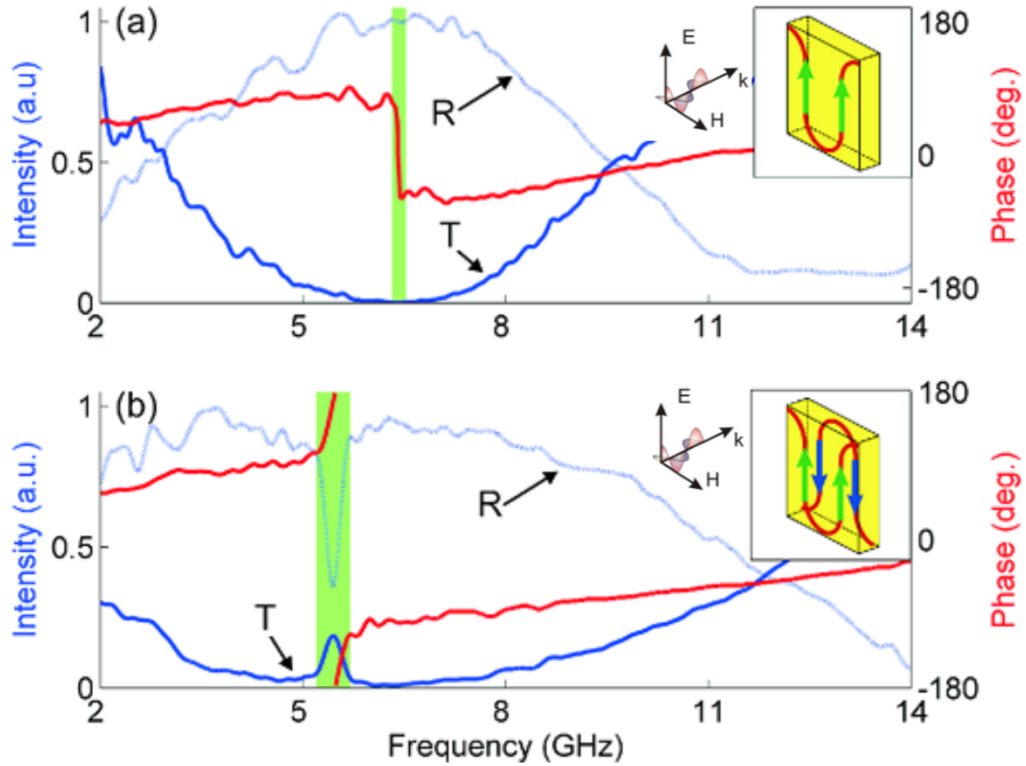


Fig. 2.14. Transmission and reflection spectra and phase change for a) single and b) double layers fish scale structure in microwave [Papasimakis 2008].

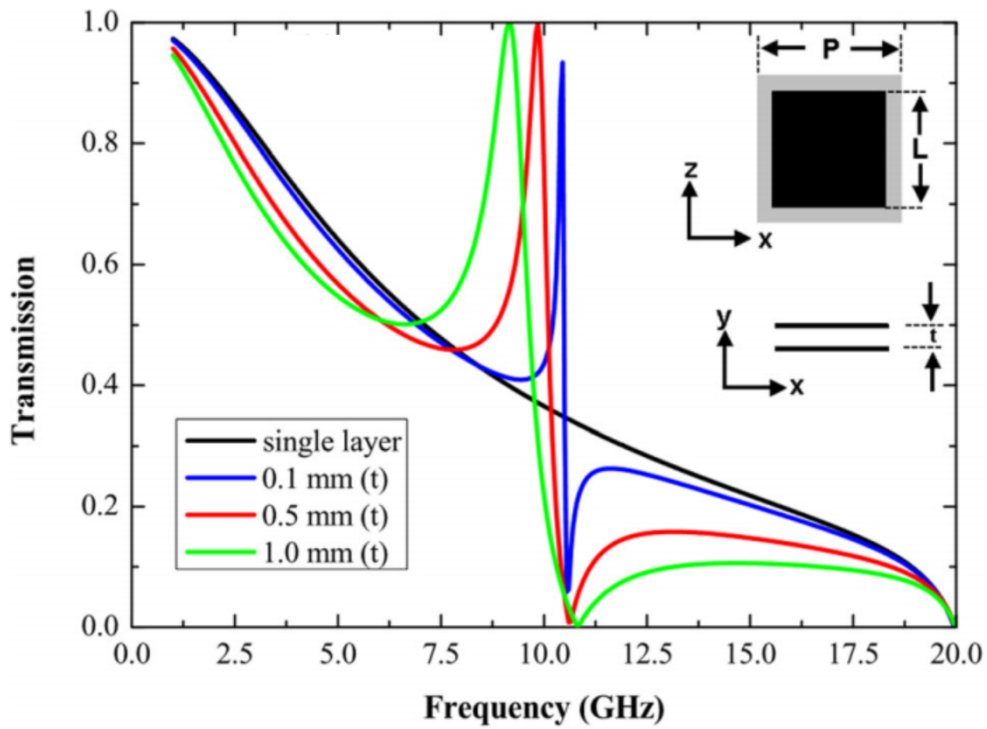
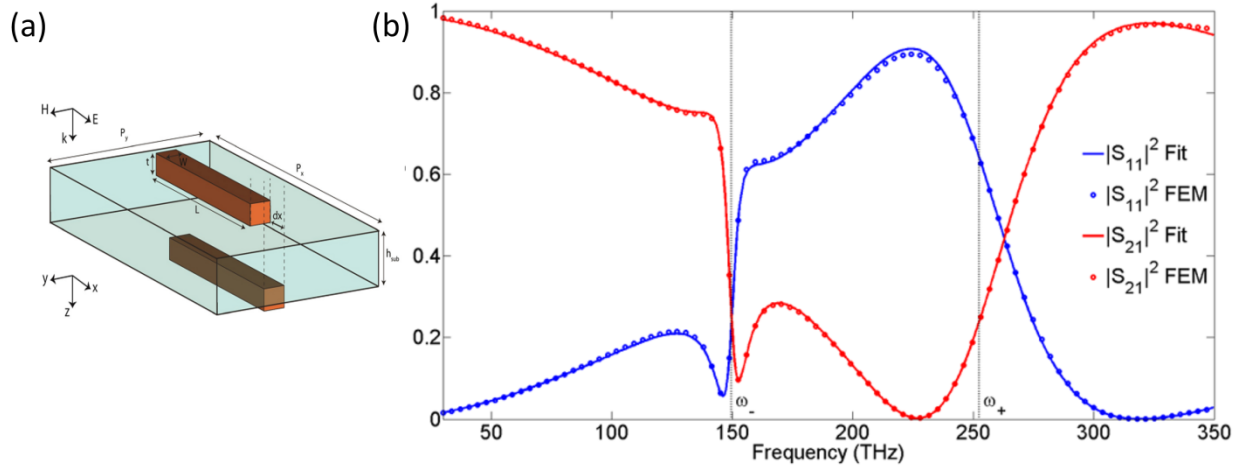


Fig. 2.15. Evolution of Fano resonance for aligned double layers of square patches at different thickness of dielectric spacer [Kanjanasit 2013].



**Fig. 2.16. (a) Unit cell of paired gold bars separated by a dielectric substrate. (b) Simulated transmission and reflection characteristics (solid curve), rational fit (dotted curve) for aligned bars [Kodigala 2015].**

## 2.5. Direct improvement of the resonators' quality factors

The ultimate method for the enhancement of the selectivity of the spectral response is related to the direct improvement of the resonators' quality factor. Most of the research devoted to this direction was focused on the search of alternatives to the metal by replacing it with dielectric or semiconductor materials having lower absorption losses [Boltasseva 2011]. The objective of the present study is rather different. The aim is to provide insights on the geometry design of resonant elements allowing reducing radiation losses and thus improving resonance quality factor. Since the higher radiation losses correspond to that of an electric dipole emitter, the second higher order term in the multipolar decomposition is that of a magnetic dipole. The solution found in the present PhD work for the selective excitation of dipolar magnetic or higher order emitters, the advantages brought for sensing applications are detailed in the next chapter. The fact that these higher order multipoles can be excited only under certain conditions, for instance only by the magnetic component of the incident field, means that they also considered as dark modes. The distinct feature as compared to the previously considered cases is that some of these dark modes are allowed for a direct excitation mechanism that is not relying on any Fano interference interaction [Burokur 2015].

## 2.6. Simulation and measurement tools

The goal of this thesis is to advance in issues of current approaches concerning the engineering of high-quality factor Fano resonance and efficient dark mode excitation in plasmonic MSs. To examine the phenomena and effects investigated through this work, numerical simulations are conducted using the finite element method (FEM) based Maxwell's equation solver of high frequency structure simulator (HFSS) commercial code by ANSYS [www.ansys.com]. This tool provides the calculation of scattering matrix parameters and field distributions for the designed MSs.

In order to examine the periodically structured metamaterials, a single unit cell is computed with appropriate periodic boundary conditions. The unit cell represents parallelepiped box with MS pattern set normally (in the case of normal-to-plane propagation) to the expected direction of propagation of source radiation, as illustrated in Fig. 2.17. The periodicity of designed two-dimensional unit cell is realized by assigning side faces of the box as Master/Slave boundaries. The E-field on the master boundary matches the E-field on the corresponding slave boundary within a phase difference that allows to simulate infinite periodic arrays. It is important to note that Master/Slave boundaries support simulations under oblique incidence. The source of electromagnetic field and direction of propagation are determined by Floquet ports. The assigned periodic boundary conditions and excitation ports are presented in Fig 2.17a and b respectively.

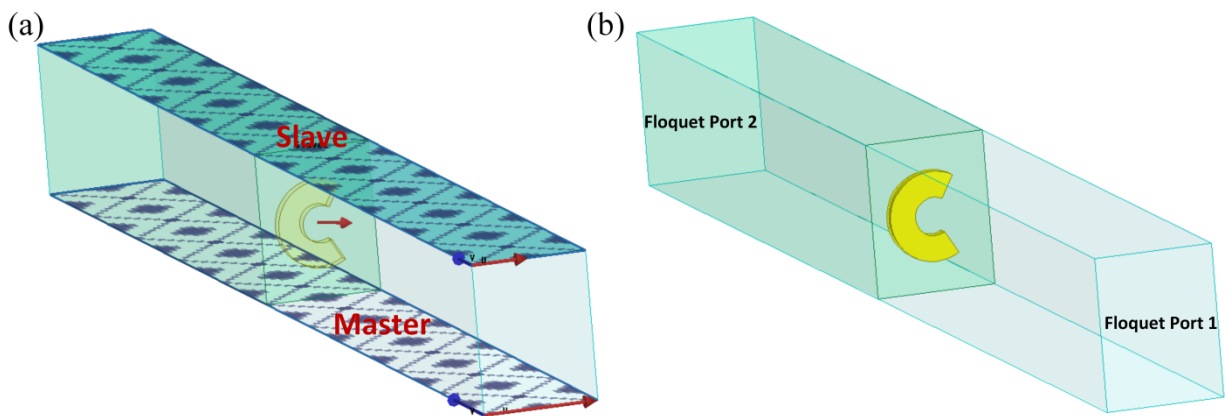


**Fig. 2.17. (a) Master/Slave boundaries and (b) excitation ports for the simulated three-dimensional unit cell.**

Though most of the studies in this thesis are basically performed in the microwave region, structures in the optical region have also been examined. Underlying scheme of numerical simulation for both frequency regions is the same except for features related to the change of

metal behavior at optical frequencies. In microwave domain calculations, metal is assumed perfect and thickness of metallic elements can be considered zero. For high frequency region, to account for finite conductivity, the dispersion relation in metal is introduced. In addition, the metallic thickness becomes important, that requires 3-D design of resonant element.

To experimentally validate modeling results, several prototypes of studied MSs are fabricated. Microwave structures are fabricated by using classical printed circuit board technology. Microwave transmission measurements are conducted in an anechoic chamber using an Agilent 8722ES network analyzer and two wideband horn antennas. The experimental setup is schematically shown in Fig. 2.18a. To account for the influence of signal propagation from the antenna to the sample, it is necessary to make phase referencing and normalization by measuring data without the prototype in the signal path. Oblique incidence measurements are provided by controlling rotation of sample set on the turn table as demonstrated in Fig. 2.18b. Reflection measurements are done by placing the source and receiving horns on the same side of the sample and bouncing the microwave signal off the sample. The source and receiver horns are each inclined with an angle of about  $4\text{--}5^\circ$  with respect to normal on the sample surface. The reflection measurement is calibrated using a sample-sized sheet of copper as a reflecting mirror.

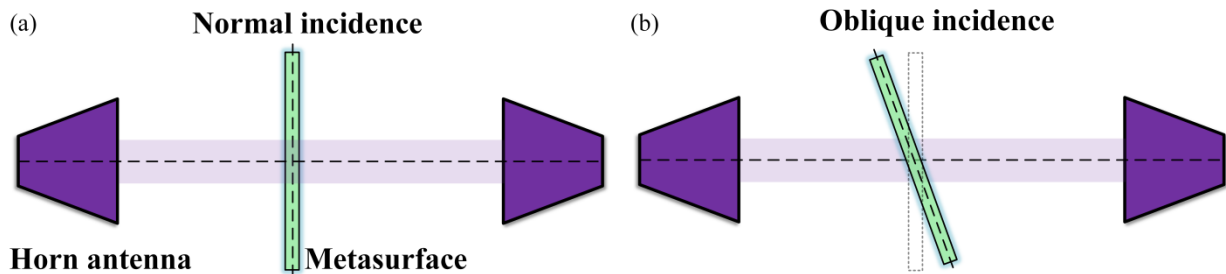


**Fig. 2.18. Experimental setup for (a) normal and (b) oblique incidence microwave measurements.**

The fabrication and technology characterization measurements of samples intended for optical frequencies have been performed by using the Centre for Nanoscience and Nanotechnology (C2N) clean room fabrication facilities. The experimental metasurfaces have been fabricated by using electron beam lithography to print periodic nano-scale metallic elements on a dielectric substrate. Spectral measurements have been performed by using angle resolved Fourier-transform infrared spectroscopy allowing to obtain spectral characteristics under oblique incidence for both TE and TM waves (Fig. 2.19).

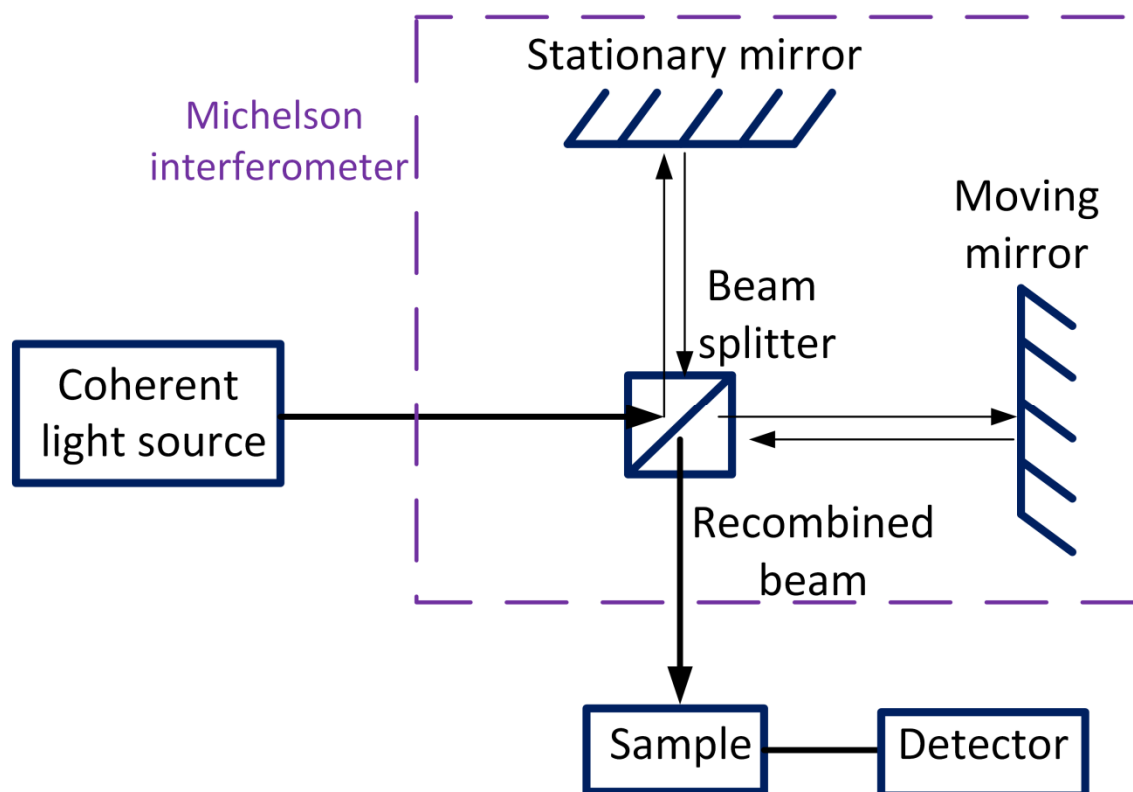


**Fig. 2.19. Schematic principle of standard FTIR setup based on Michelson interferometer. Moving mirror allows controlling optical path difference. The signal beam coming from the interferometer to the detector is processed by computer to obtain resulting spectral characteristics.**

## 2.7. Summary and conclusion

We revisit the engineering of metasurfaces displaying sharp spectral features and conventionally relying on the use of electromagnetically induced transparency resulting from Fano type interference between dark and bright resonant elements. The last theoretical advances have led to revisit this commonly shared interpretation. In particular it was shown that no dark mode excitation is necessary for EIT resonances. They can be described by the interference of bright modes only. In contrast, the Fano interference of two modes with substantially different radiative strength results in a very weak EIT effect. The origin of this apparent contradiction stems from the fact that the eigenmodes of the coupled system can significantly differ from those of the individual elements, and in general they are not orthogonal.

An obvious question arising in the context of the present study and that we address by the following is whether it is possible to achieve Fano interference in a more efficient manner, without making use of the element with different radiative strength but rather through an interaction of identical resonators representing bright resonant elements. The implementation of such EIT

excitation mechanism would be highly desirable due to the possibility to obtain more efficient resonance response.

We also address the problematic of EIT in Fabry-Perot cavities formed by near-field coupled MSs. The variation of the refractive index inside the photonic cavity influences both near-field and far-field coupling between the MSs, resulting in an enhancement of sensing capabilities. We expect such structures to play an important role in the next generation of optical biosensors and telecom filters.

Based on the symmetry approach presented in the next chapter we bring theoretical and experimental evidence in the microwave domain that EIT and dark mode excitation can be achieved in an independent manner by using distinctly different mechanisms. The use of these distinctly different mechanisms provides higher flexibility for the MSs engineering and results in a great improvement of their spectral performances.

## References

- [Alzar 2002] C.L.G. Alzar, M.A.G. Martinez & P. Nussenzeig, 2002. "Classical analog of electromagnetically induced transparency". *American Journal of Physics*, 70, pp.37-41.
- [Ameling 2012] R. Ameling & H. Giessen, 2012. "Microcavity plasmonics: strong coupling of photonic cavities and plasmons". *Laser & Photonics Reviews*, 7, pp.141-169.
- [Ameling 2010] R. Ameling et al., 2010. "Cavity-enhanced localized plasmon resonance sensing". *Applied Physics Letters*, 97, p.253116.
- [Aydin 2010] K. Aydin, I.M. Pryce & H.A. Atwater, 2010. "Symmetry breaking and strong coupling in planar optical metamaterials". *Optics Express*, 18, p.13407.
- [Bao 2010] K. Bao, N.A. Mirin & P. Nordlander, 2010. "Fano resonances in planar silver nanosphere clusters". *Applied Physics A*, 100, pp.333-339.
- [Beutler 1935] H. Beutler, 1935. "Über Absorptionsserien von Argon, Krypton und Xenon zu Termen zwischen den beiden Ionisierungsgrenzen  $2P\ 3/2$  und  $2P\ 1/2$ ". *Zeitschrift für Physik*, 93, pp.177-196.
- [Boltasseva 2011] A. Boltasseva & H.A. Atwater, 2011. "Low-Loss Plasmonic Metamaterials". *Science*, 331, pp.290-291.
- [Burokur 2015] S.N. Burokur, A. Lupu & A. Lustrac, 2015. "Direct dark mode excitation by symmetry matching of a single-particle-based metasurface". *Physical Review B*, 91.

- [Christ 2007] A. Christ et al., 2007. “Controlling the Fano interference in a plasmonic lattice”. *Physical Review B*, 76.
- [Christ 2008] A. Christ et al., 2008. “Symmetry Breaking in a Plasmonic Metamaterial at Optical Wavelength”. *Nano Letters*, 8, pp.2171-2175.
- [Chuntonov 2011] L. Chuntonov & G. Haran, 2011. “Trimeric Plasmonic Molecules: The Role of Symmetry”. *Nano Letters*, 11, pp.2440-2445.
- [Duan 2012] X. Duan et al., 2012. “Polarization-insensitive and wide-angle plasmonically induced transparency by planar metamaterials”. *Applied Physics Letters*, 101, p.143105.
- [Fano 1936] U. Fano, 1936. “Some Theoretical Considerations on Anomalous Diffraction Gratings”. *Physical Review*, 50, pp.573-573.
- [Fano 1961] U. Fano, 1961. “Effects of Configuration Interaction on Intensities and Phase Shifts”. *Physical Review*, 124, pp.1866-1878.
- [Fan 2003] S. Fan, W. Suh & J.D. Joannopoulos, 2003. “Temporal coupled-mode theory for the Fano resonance in optical resonators”. *Journal of the Optical Society of America A*, 20, p.569.
- [Fan 2010] J.A. Fan et al., 2010. “Self-Assembled Plasmonic Nanoparticle Clusters”. *Science*, 328, pp.1135-1138.
- [Fedotov 2007] V.A. Fedotov et al., 2007. “Sharp Trapped-Mode Resonances in Planar Metamaterials with a Broken Structural Symmetry”. *Physical Review Letters*, 99.
- [Fleischhauer 2005] M. Fleischhauer, A. Imamoglu & J.P. Marangos, 2005. “Electromagnetically induced transparency: Optics in coherent media”. *Reviews of Modern Physics*, 77, pp.633-673.

- [Forestiere 2013] C. Forestiere, L.D. Negro & G. Miano, 2013. “Theory of coupled plasmon modes and Fano-like resonances in subwavelength metal structures”. *Physical Review B*, 88.
- [Frimmer 2012] M. Frimmer, T. Coenen & A.F. Koenderink, 2012. “Signature of a Fano Resonance in a Plasmonic Metamolecule’s Local Density of Optical States”. *Physical Review Letters*, 108.
- [Gallinet 2011] B. Gallinet & O.J.F. Martin, 2011. “Influence of Electromagnetic Interactions on the Line Shape of Plasmonic Fano Resonances”. *ACS Nano*, 5, pp.8999-9008.
- [Gallinet 2013] B. Gallinet & O.J.F. Martin, 2013. “Refractive Index Sensing with Subradiant Modes: A Framework To Reduce Losses in Plasmonic Nanostructures”.
- [Gray 1978] H.R. Gray, R.M. Whitley & C.R. Stroud, 1978. “Coherent trapping of atomic populations”. *Optics Letters*, 3, p.218.
- [Gu 2012] J. Gu et al., 2012. “Active control of electromagnetically induced transparency analogue in terahertz metamaterials”. *Nature Communications*, 3, p.1151.
- [Hao 2008] F. Hao et al., 2008. “Symmetry Breaking in Plasmonic Nanocavities: Subradiant LSPR Sensing and a Tunable Fano Resonance”. *Nano Letters*, 8, pp.3983-3988.
- [Harris 1997] S.E. Harris, 1997. “Electromagnetically Induced Transparency”. *Physics Today*, 50, pp.36-42.
- [Haus 1984] H.A. Haus, 1984. *Waves and Fields in Optoelectronics* (Prentice-Hall series in solid state physical electronics).

- [Hentschel 2011] M. Hentschel et al., 2011. “Plasmonic Oligomers: The Role of Individual Particles in Collective Behavior”.
- [Hopkins 2013] B. Hopkins, A.N. Poddubny, A.E. Miroshnichenko & Y.S. Kivshar, 2013. “Revisiting the physics of Fano resonances for nanoparticle oligomers”. *Physical Review A*, 88.
- [Hu 2016] X. Hu et al., 2016. “Plasmon induced transparency and absorption in brighttextendashbright mode coupling metamaterials: a radiating two-oscillator model analysis”. *Journal of Physics D: Applied Physics*, 50, p.025301.
- [Joe 2006] Y.S. Joe, A.M. Satanin & C.S. Kim, 2006. “Classical analogy of Fano resonances”. *Physica Scripta*, 74, pp.259-266.
- [Kanjanasit 2013] K. Kanjanasit & C.H. Wang, 2013. “Fano resonance in a metamaterial consisting of two identical arrays of square metallic patch elements separated by a dielectric spacer”. *Applied Physics Letters*, 102, p.251108.
- [Kodigala 2015] A. Kodigala, T. Lepetit & B. Kante, 2015. “Engineering resonance dynamics of plasmon hybridized systems”. *Journal of Applied Physics*, 117, p.023110.
- [Lee 2015] Y.U. Lee et al., 2015. “Double Fano resonances in a composite metamaterial possessing tripod plasmonic resonances”. *Journal of Optics*, 17, p.025103.
- [Lepetit 2010] T. Lepetit, E. Akmansoy, J.-P. Ganne & J.-M. Lourtioz, 2010. “Resonance continuum coupling in high-permittivity dielectric metamaterials”. *Physical Review B*, 82.
- [Litvak 2002] A.G. Litvak & M.D. Tokman, 2002. “Electromagnetically Induced Transparency in Ensembles of Classical Oscillators”. *Physical Review*

*Letters*, 88.

- [Liu 2010] F. Liu et al., 2010. “Acoustic analog of electromagnetically induced transparency in periodic arrays of square rods”. *Physical Review E*, 82.
- [Liu 2009] N. Liu et al., 2009. “Plasmonic analogue of electromagnetically induced transparency at the Drude damping limit”. *Nature Materials*, 8, pp.758-762.
- [Lovera 2013] A. Lovera, B. Gallinet, P. Nordlander & O.J.F. Martin, 2013. “Mechanisms of Fano Resonances in Coupled Plasmonic Systems”. *ACS Nano*, 7, pp.4527-4536.
- [Lukýanchuk 2010] B. Lukýanchuk et al., 2010. “The Fano resonance in plasmonic nanostructures and metamaterials”. *Nature Materials*, 9, pp.707-715.
- [Maleki 2004] L. Maleki, A.B. Matsko, A.A. Savchenkov & V.S. Ilchenko, 2004. “Tunable delay line with interacting whispering-gallery-mode resonators”. *Optics Letters*, 29, p.626.
- [Merchiers 2007] O. Merchiers, F. Moreno, F. Gonzalez & J.M. Saiz, 2007. “Light scattering by an ensemble of interacting dipolar particles with both electric and magnetic polarizabilities”. *Physical Review A*, 76.
- [Mirin 2009] N.A. Mirin, K. Bao & P. Nordlander, 2009. “Fano Resonances in Plasmonic Nanoparticle Aggregates”. *The Journal of Physical Chemistry A*, 113, pp.4028-4034.
- [Miroshnichenko 2010] A.E. Miroshnichenko, S. Flach & Y.S. Kivshar, 2010. “Fano resonances in nanoscale structures”. *Reviews of Modern Physics*, 82, pp.2257-2298.
- [Miroshnichenko 2012] A.E. Miroshnichenko & Y.S. Kivshar, 2012. “Fano Resonances in All-Dielectric Oligomers”. *Nano Letters*, 12, pp.6459-6463.

- [Nordlander 2004] P. Nordlander et al., 2004. “Plasmon Hybridization in Nanoparticle Dimers”. *Nano Letters*, 4, pp.899-903.
- [Papasimakis 2008] N. Papasimakis, V.A. Fedotov, N.I. Zheludev & S.L. Prosvirnin, 2008. “Metamaterial Analog of Electromagnetically Induced Transparency”. *Physical Review Letters*, 101.
- [Prodan 2003] E. Prodan, 2003. “A Hybridization Model for the Plasmon Response of Complex Nanostructures”. *Science*, 302, pp.419-422.
- [Qin 2013] L. Qin et al., 2013. “Optical-magnetism-induced transparency in a metamaterial”. *Physical Review B*, 87.
- [Ratni 2017] B. Ratni et al., 2017. “Design of Phase-Modulated Metasurfaces for Beam Steering in Fabry–Perot Cavity Antennas”.
- [Ruan 2012] Z. Ruan & S. Fan, 2012. “Temporal coupled-mode theory for light scattering by an arbitrarily shaped object supporting a single resonance”. *Physical Review A*, 85.
- [Singh 2011] R. Singh et al., 2011. “Observing metamaterial induced transparency in individual Fano resonators with broken symmetry”. *Applied Physics Letters*, 99, p.201107.
- [Suh 2004] W. Suh, Z. Wang & S. Fan, 2004. “Temporal coupled-mode theory and the presence of non-orthogonal modes in lossless multimode cavities”. *IEEE Journal of Quantum Electronics*, 40, pp.1511-1518.
- [Tassin 2009] P. Tassin et al., 2009. “Low-Loss Metamaterials Based on Classical Electromagnetically Induced Transparency”. *Physical Review Letters*, 102.
- [Vahala 2003] K.J. Vahala, 2003. “Optical microcavities”. *Nature*, 424, pp.839-846.

- [Verellen 2009] N. Verellen et al., 2009. “Fano Resonances in Individual Coherent Plasmonic Nanocavities”. *Nano Letters*, 9, pp.1663-1667.
- [Wang 2006] H. Wang et al., 2006. “Symmetry breaking in individual plasmonic nanoparticles”. *Proceedings of the National Academy of Sciences*, 103, pp.10856-0860.
- [Wiersig 2006] J. Wiersig, 2006. “Formation of Long-Lived, Scarlike Modes near Avoided Resonance Crossings in Optical Microcavities”. *Physical Review Letters*, 97.
- [Wood 1935] R.W. Wood, 1935. “Anomalous Diffraction Gratings”. *Physical Review*, 48, pp.928-936.
- [Xu 2006] Q. Xu et al., 2006. “Experimental Realization of an On-Chip All-Optical Analogue to Electromagnetically Induced Transparency”. *Physical Review Letters*, 96.
- [Zhang 2008] S. Zhang et al., 2008. “Plasmon-Induced Transparency in Metamaterials”. *Physical Review Letters*, 101.



## **Chapter 3.**

### **Direct dark mode excitation mechanism based on symmetry matching**

The features of plasmon resonance in MMs open a wide field of opportunities for their applications in different areas. One of the most important concerns antennas, cloaking devices and signal control systems such as switches and filters. Furthermore, sensitivity of plasmon resonance to the refractive index variation in the environments make MMs widely used for sensing and detecting biomolecules. The essential characteristic required for sensing application is high quality factor resonance with steep intensity variation [Anker 2008; Lal 2007; Willets 2007; Zhang 2008]. However, plasmon resonance is not able to provide required sensing properties due to low quality-factor. One of the most promising solution intended to circumvent the limitation of plasmon resonance is the dark mode excitation and the phenomenon of EIT allowing to obtain much narrow resonances compared to fundamental one.

As it has been discussed in previous chapter dark modes are usually associated with phenomenon of EIT as a result of interference of bright and dark modes [Liu 2009; Prodan 2003; Chiam 2009]. In this context, dark modes cannot be directly excited, however, they can be obtained from mode hybridization induced by strong near-field coupling between elements [Lukyanchuk 2010]. Dark mode is characterized by low radiative losses and represent excitation of out-of-phase current oscillations. Hence such modes are manifested as extremely narrow resonance compared to bright modes. However, as it has been mentioned above, the hybridization mechanism is very sensitive to the variation of separation distance between elements and consequently, to the fabrication tolerances and imperfections. This makes dark mode engineering quite challenging, particularly in optics.

We will consider in the framework of my thesis, different mechanism of dark mode excitation through symmetry matching of the resonant element and the incident electromagnetic field. As well known, the form of induced dipoles is determined by symmetry of geometry with respect to the incident field [Padilla 2007]. Using the appropriate design and matching the symmetry of magnetic and electric field allows to provide dark mode resonance in individual resonator through direct field coupling not relying on mode hybridization. This greatly relaxes fabrication process in the optical domain that allows obtaining high quality factor resonances.

### 3.1. Symmetry matching approach

The electromagnetic response of MSs is based on surface plasmons which are collective oscillations of free electrons in metal excited by external field. The excited modes are associated with induced dipole moment or currents in the elements. The current flow is determined by geometry of element and its orientation with respect to the incident field. To explain resonance behavior of complex structure through resonator symmetry, group theory approach is often used, particularly when investigating anisotropic optical designs [Padilla 2007; Baena 2007; Wongkasem 2006; Reinke 2011]. However, in many cases it is possible to get an insight on the resonator behavior simply from general considerations.

Let us consider the example of a cut wire (CW) represented in Fig. 3.1a. Under normal incidence for a linearly polarized electric field  $\vec{E}$  oriented along the CW's elongation direction, the excitation of a CW represents an induced electric dipole with currents flowing from one CW's end to another. In a similar manner the excitation of a split ring resonator (SRR) with an electric field parallel to the gap direction results in a same kind of resonance behavior (Fig. 3.1b). Same result is obtained for 180° rotated structure except that, as displayed in Fig. 3.1c, the current flow have changed direction from clockwise to counter-clockwise direction. In contrast, as shown in Fig. 3.1d, when the resonator geometry is having mirror symmetry with respect to direction of incident  $\vec{E}$ -field, the excited currents will be also symmetric since electric field is even, i.e.  $E(-r) = -E(r)$ .

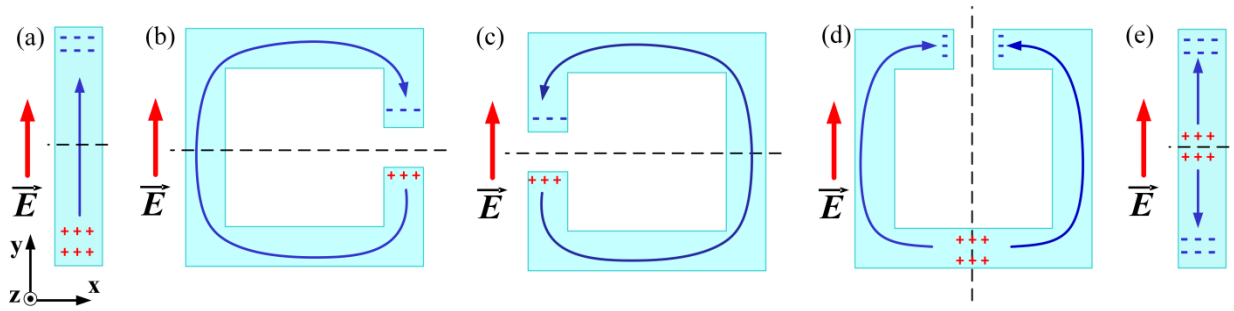


**Fig. 3.1. Schematic of excitation under normal incidence with electric field polarized along the y-axis. (a)-(d) fundamental electric dipole excitation for single CW and SRR. (e) Forbidden dark mode.**

One noteworthy symmetry property of the magnetic field is illustrated in Fig. 3.2. Owing to the axial nature of magnetic field, the circulation of induced current does not change direction when a mirror symmetry operation is applied to the SRR. This distinctly different behavior of magnetic

field as compared to that of electric field will be used in the following to match the symmetry of resonator's geometry with that of incident electromagnetic field.

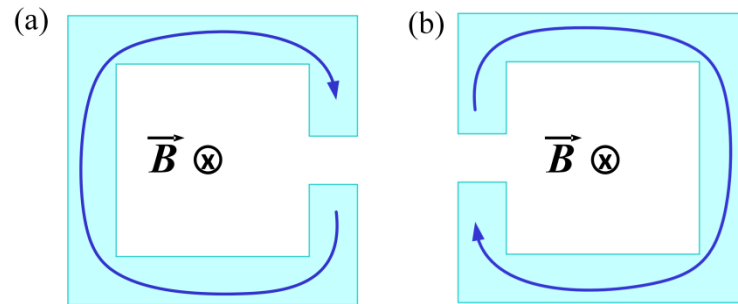


**Fig. 3.2.** Schematic of induced by magnetic field current for (a) SRR and (b) rotated SRR on  $180^\circ$ .

On the base of above considerations, the analysis of optimal geometry for dark mode excitation is now considered. As it has been discussed in Chapter 2, the dark mode is weakly coupled to the free space because of vanishingly low projection of its electric dipolar momentum on the electric component of the incident field. One of possible configurations of dark mode is schematically depicted in Fig. 3.1e, where the two dipolar momentum are oriented in opposite directions. The issue is that such an antisymmetric mode can't be directly excited by the electric field of a normally incident plane wave. The problem addressed in the following is how to achieve the direct excitation of such an antisymmetric mode without making use of some hybridization mechanism and what should be the optimal resonator geometry in this case?

One point important to note in this context is that the geometry of the resonator supporting such antisymmetric mode excitation should not possess mirror symmetry with respect to the electric field component of the incident plane wave. This is necessary to prevent a current distribution like that shown in Fig. 3.1d. According to the quasistatic approximation, since the dimensions of resonators are much smaller than the wavelength, the induced dipole moment  $\mathbf{p}$  is linearly proportional to the amplitude of incident field [Sersic 2012].

So the interaction of induced dipole with external E-field is more efficient when they are parallel. For this reason, both the ends and the center of the resonator's pattern should lie on the axis parallel to the orientation of the E-component of the field.

One of the simplest geometry satisfying above requirements is shown in Fig. 3.3a. It consists of two inverted V-antennas aligned along the  $y$ -axis.

The fact that dark mode is forbidden means that it cannot be excited due to zero net electric dipolar momentum. One of the conventional solutions used to achieve dark mode excitation is the symmetry breaking. It leads to an unbalance between two oppositely oriented dipoles [Tassin 2009; Cao 2012]. For instance, introducing different length of V-elements with respect to the center of the structure results in non-zero net electric dipolar momentum. The interaction with the external field becomes then allowed. The coupling with the incident field is directly proportional to the value of the resulting from unbalance dipolar momentum. This situation is however somewhat trivial. By the following we will focus our attention on the case when there is no any unbalance and the two electric dipoles associated with the antisymmetric mode perfectly cancel each other.

To this end we consider another excitation mechanism that is rather based on the interaction with the magnetic component of the incident field and orient our study on resonators with inversion symmetry geometry. Such symmetry matching approach for dark mode excitation was initially introduced in [Burokur 2015]. Let us consider its operation principle. Magnetic field is axial and therefore is invariant under the inversion of coordinates. Hence the magnetic momenta induced by opposite currents in the top and bottom V-antennas are oriented in the same direction resulting in a net non-zero magnetic dipolar momentum. Thus, as illustrated in Fig. 3.2, under oblique incidence the magnetic component of the incident field can produce a direct excitation of the antisymmetric dark mode. This symmetry matching leads to magnetic dipole excitation and allows to considerably reducing radiation losses.

To examine the electromagnetic behavior of two connected inverted V-antennas, numerical simulations of transmission and reflection characteristics were performed in the microwave domain. For the sample, the metal is assumed to be ideal and the dielectric substrate for the sample is copper-clad epoxy with a permittivity  $\epsilon_r = 3.9$ , tangential losses  $\tan\delta = 0.02$  and a thickness of 0.4 mm. The unit cell dimensions are  $p_x = 6.9$  mm and  $p_y = 15.8$  mm. The wire length is 16.3 mm and the width is 0.3 mm. The opening angle of each V element is  $120^\circ$ . The polarization of electric field is orientated along the  $y$ -axis that is perpendicular to the oblique incidence  $xoz$  plane (Fig. 3.3a).

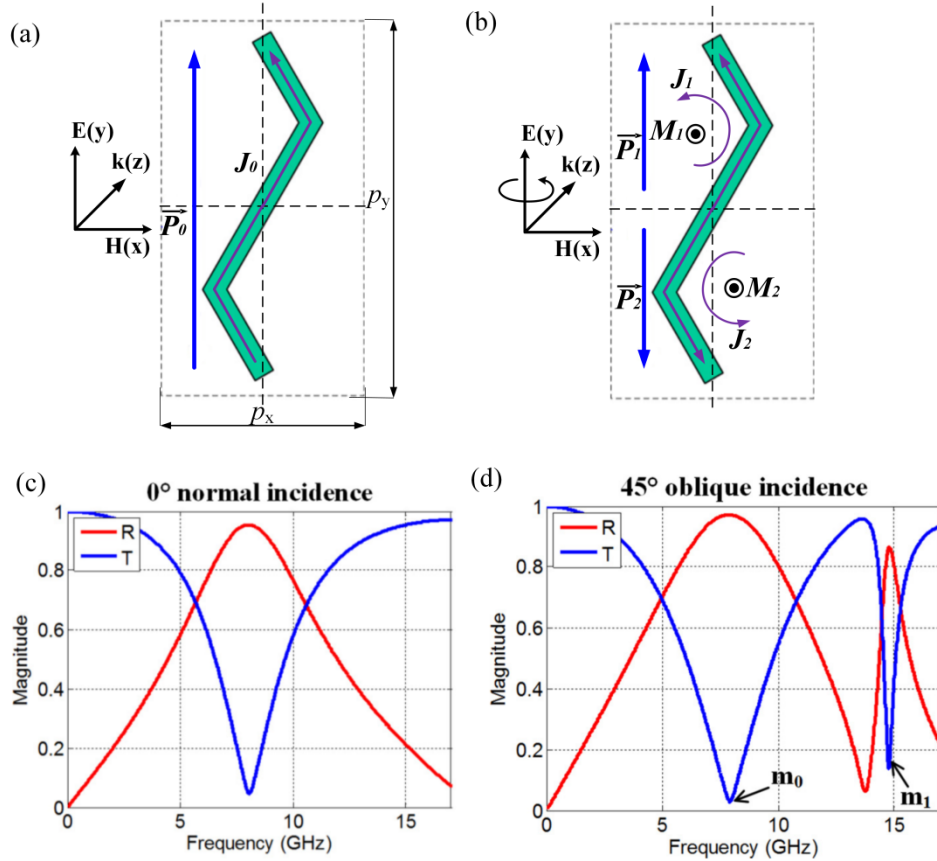


**Fig. 3.3. Schematic of fundamental TE (a) and first higher order mode (b) excitations in connected V-antennas. (c) Simulated transmission and reflection spectra under normal incidence. (d) Oblique incidence simulated spectral response [Burokur 2015].**

For this configuration under normal incidence the structure exhibits only fundamental electric dipole excitation at 8.1 GHz, as depicted in Fig. 3.3a, c. The excitation of the first higher order mode is forbidden since electric field cannot interact with this antisymmetric dark mode due to zero net dipole moment. However, under oblique incidence the interaction with the magnetic component of the incident field brings allowed excitation of this dark mode. As it can be seen from Fig. 3.3d, under oblique incidence the transmission and reflection spectra exhibit not only fundamental dipolar mode at 8.1 GHz but also an additional resonance at 14.8 GHz related to the magnetic dipole excitation. Note that the quality factor of the dark mode ( $Q = 9.5$ ) is almost an order of magnitude higher as compared to that of fundamental resonance ( $Q = 1.1$ ). The provided above results show that even with a raw design that was not subjected to any optimization the excitation at 14.8 GHz of the magnetic dipole instead of electric one indeed provides a significant improvement of the spectral response selectivity. By consequence it seems possible to have a room for further amelioration of performances. To this end for a fixed resonator length we consider a more compact unit cell design. Two V-antennas are transformed to the Z-shaped

resonator with two legs perpendicular to the E-field as displayed in Fig. 3.4. The dimensions of the unit cell is  $p_x = p_y = 6$  mm. The length of the Z-element along x- and y-directions is, respectively,  $l_x = 5.8$  mm and  $l_y = 5.7$  mm, and the width is 0.3 mm.

Similarly to two asymmetric V-antennas design, under normal incidence the Z-shaped resonator displays only one resonance at 4.5 GHz corresponding to the fundamental mode excitation. This is confirmed by instantaneous current distributions shown in Fig. 3.5a. Under oblique incidence transmission and reflection spectra exhibit an additional resonance feature at 13.7 GHz related to the dark mode excitation. As it can be seen from Fig. 3.5b, at this resonance two opposite currents are excited leading to non-zero magnetic moment. While having a behavior similar to that of two connected V-antennas, Z-shape design brings a notable improvement of the dark mode resonance.

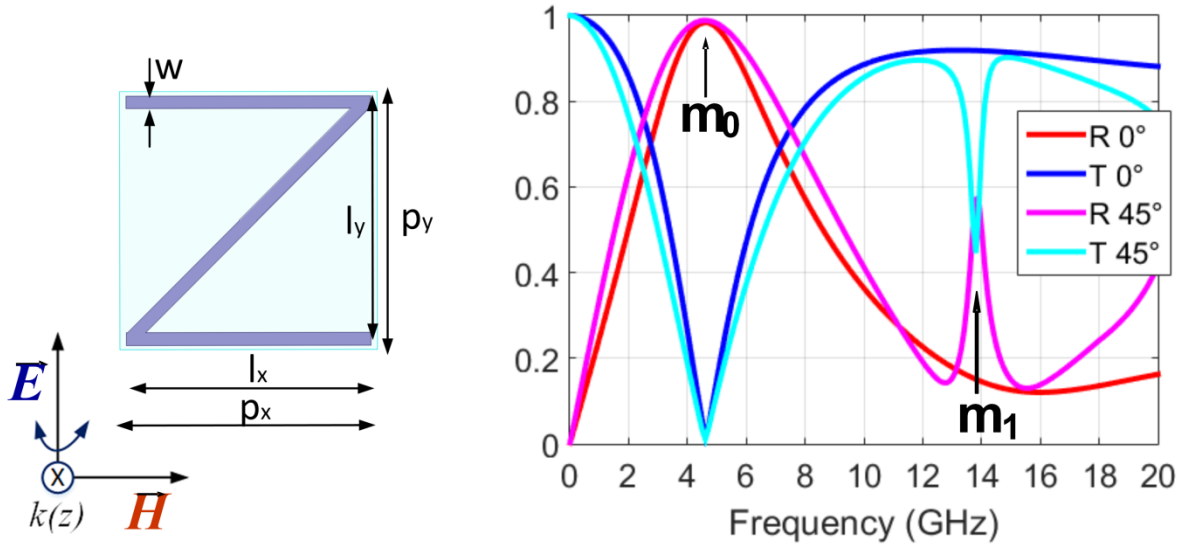


**Fig. 3.4. Dark mode excitation in Z-shaped resonator. Simulated transmission and reflection spectra under normal and oblique incidence for TE mode configuration.**

As it can be observed from Figs. 3.3 and 3.4, for an identical resonator length, passing from two V-antennas to Z-shape design reduce the induced electric dipole projection on the direction of external electric field. The narrowing of the fundamental mode frequency bandwidth, which is of 7.3 GHz for V-antennas and 6.9 GHz for Z design, proves this. The bandwidth narrowing of the antisymmetric dark mode from 1.5 GHz for V-antennas to 0.6 GHz for Z turns out to be much more significant. In summary for Z-shape design, the quality factor of fundamental and dark mode resonances is  $Q_{\text{fund}} = 0.9$  and  $Q_{\text{dark}} = 23$ , respectively. The issue however is that the increase of the resonance quality factor is accompanied by the decrease of the contrast related to

### 3.1 Symmetry matching approach

the amplitude of the resonant spectral response variation. The amplitude of dark mode excitation in reflection is  $A = 0.81$  for connected V-antennas and  $A = 0.43$  for Z-shape design. The limitation induced by this issue becomes particularly stringent when moving to optical frequencies where other factors additionally contribute to lowering the resonance contrast. Solving this issue by further amelioration of design is presented in the next section on the example of MSs operating in the optical domain.

It should be emphasized, that dark mode resonance does not rely on coupling between adjacent resonators and is related only to the excitations in individual elements that is evidenced by spectral characteristics for increased dimensions of unit cell in Fig. 3.6. As it can be seen, both the dark mode and fundamental mode are present when the period of unit cell becomes equal to  $p_x = p_y = 9$  mm. The influence of resonators coupling manifests as frequency shift of resonance positions from 4.5 GHz to 6.9 GHz and from 13.7 GHz to 12.8 GHz for fundamental and dark mode, respectively. In terms of LC-contour the frequency shift can be explained as the variation of capacitance formed by the top and bottom legs of two adjacent Z (Fig. 3.7). The fundamental resonance moves to higher frequency since the capacitance is decreased when the separation distance between legs is increased. In contrast the frequency of dark mode moves to lower frequency because of same sign charges accumulation on the legs of Z.

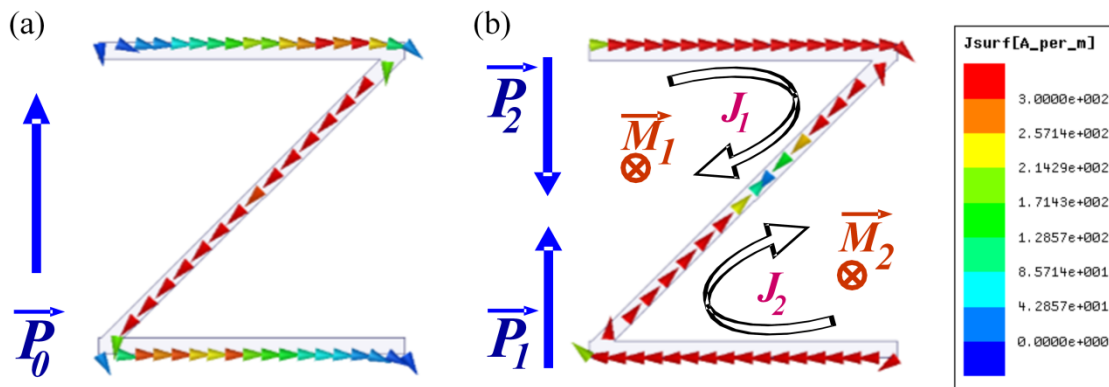


**Fig. 3.5. Instantaneous current distributions correspond to (a) fundamental TE resonance at 4.5 GHz and (b) first higher order mode at 13.7 GHz.**

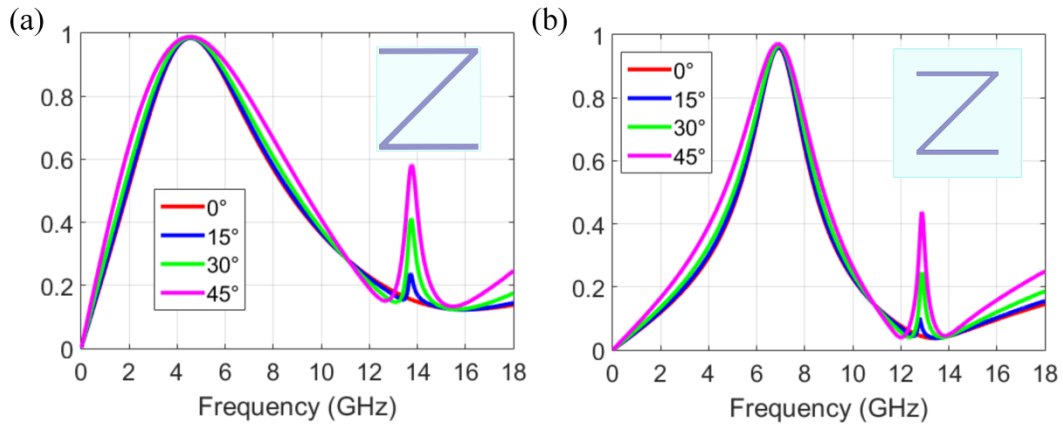


**Fig. 3.6. Reflection under normal and oblique incidence for Z-elements with period of unit cell. (a)  $p_x = p_y = 6$  mm and (b)  $p_x = p_y = 9$  mm.**

It is worthy to mention that the fundamental resonance for TE mode is practically non-sensitive to the variation of incidence angle while the amplitude of dark mode excitation noticeably increases with the incidence angle, as it can be seen in Fig. 3.6. It is because the resonance amplitude is increased for higher projection of the magnetic component of the incident field penetrating the structure. This feature represents an additional evidence of magnetic nature of the dark mode resonance.

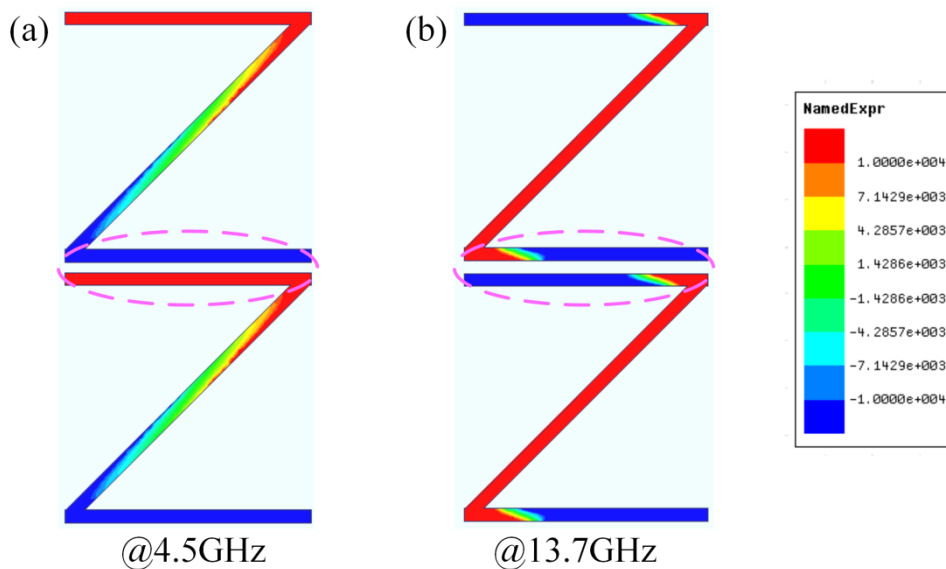


**Fig. 3.7. Instantaneous charge distributions corresponding to (a) fundamental resonance and (b) magnetic dipole excitation. The dashed line shows the area of capacitance.**

The considered examples show that dark mode indeed provides lower radiative losses through suppression of the electric dipole and resonant excitation of the magnetic dipole instead. The

excitation does not rely on coupling between elements, i.e. mode hybridization, and is related to direct interaction with magnetic field component. The conditions required for antisymmetric dark mode excitation are based only on symmetry matching considerations. By consequence such a design is expected to be more robust with respect to technology imperfections. The fabrication tolerances can be greatly relaxed, especially in the optical domain [Liu 2010].

### 3.2. Control of magnetic dipole mode

#### 3.2.1. Split Ring Resonator

In the following considered above excitation direct dark mode mechanism based on the interaction with the magnetic component of the field will be extended to the optical domain. As known, natural materials does not exhibit magnetic response in frequencies above several GHz. MMs enable to overcome this limitation and provide magnetic activity at much higher frequencies. Magnetism of conventional atoms basically originates from internal and orbital magnetic moment of electrons. Magnetic moment in MMs is determined by displacement or conducting currents. The basic resonant element used to provide magnetic resonance is SRR [Smith 2006]. The behavior of such resonator is commonly explained using LC-circuit analogy represented in Fig. 3.8a. Here the metallic coil is associated with inductance and the gap serves as capacitance [Linden 2004; Linden 2006]. The interaction with the incident electromagnetic

field leads to the excitation of LC-resonance at frequency  $\omega_{LC} = \frac{1}{2\pi\sqrt{LC}}$  through either coupling to the inductance by means of non-zero magnetic component normal to the plane of SSR or by means of capacitance coupling with the electric field. At the resonance frequency where the current loop is excited, SRR exhibits magnetic activity. However, LC-interpretation can lead to incorrect understanding of how the polarization of the external field influences on the excitation and how the electric field interacts with the structure.

Initially, it was considered that electric field is coupled to SRR only when its polarization is parallel to the gap, as shown in Fig. 3.9b. Otherwise the interaction with the electric component of the field does not occur [Linden 2006; Enkrich 2005]. For instance, under normal incidence the resonance near 1500 nm shown in Fig. 3.9b was attributed to the E-field coupling through capacitance. Under oblique incidence, H-field additionally contributes to the resonance. In contrast, for configuration shown in Fig. 3.9a, the normally incident field cannot couple neither with electric nor magnetic components. The coupling becomes possible only under oblique incidence when H-field penetrates through the SRR.

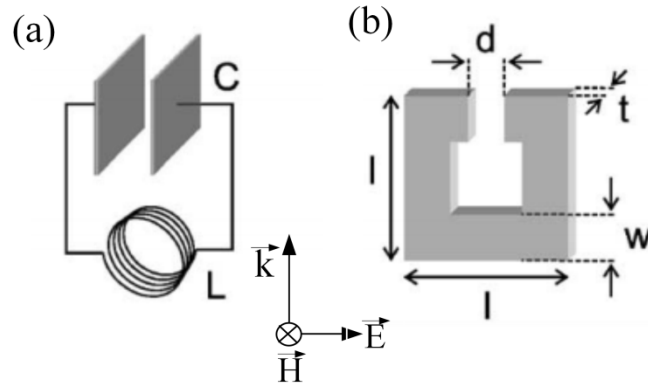


**Fig. 3.8. (a) LC-circuit analogy of SRR. (b) Characteristic dimensions of SRR and polarization of incident field [Linden 2004].**

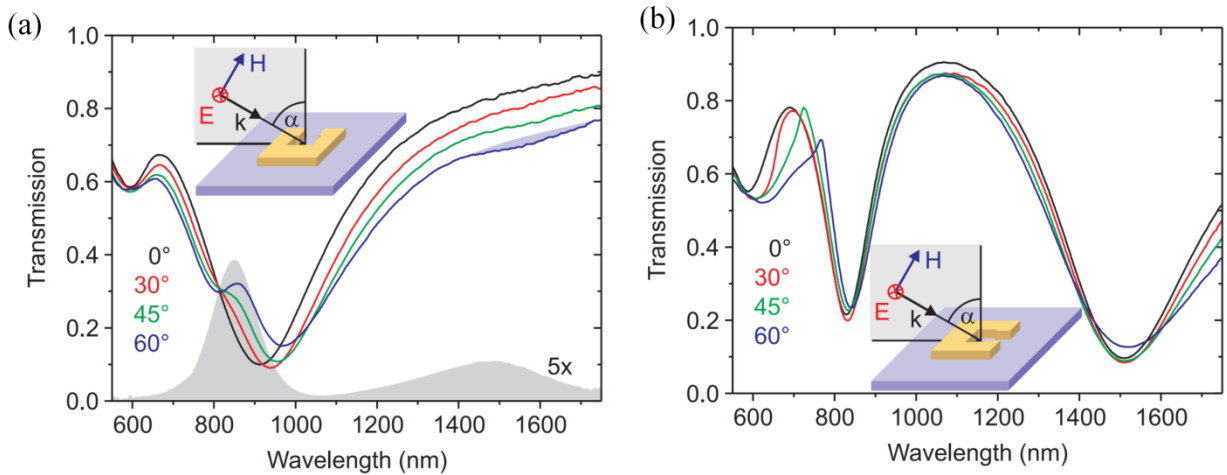


**Fig. 3.9. SRR under normal and oblique incidence. (a) E-field is perpendicular to the gap. (b) E-field is parallel to the gap. H-field penetrates structure under oblique incidence for both cases [Enkrich 2005].**

In a linear approximation the incident field electric and magnetic components and electric  $\vec{p}$  and magnetic  $\vec{m}$  dipoles are related through polarizability matrix  $\alpha$ . In Eq. (3.1),  $\alpha$  is a  $6 \times 6$  polarizability tensor consisting of four  $3 \times 3$  blocks that describes the dipole response to the electric or magnetic component of the incident. The off-diagonal block  $\alpha_c$  quantifies the magneto-electric coupling [Sersic 2012; Sersic 2011]:

$$\begin{pmatrix} \vec{p} \\ \vec{m} \end{pmatrix} = \begin{pmatrix} \alpha_E & i\alpha_C \\ -i\alpha_C^T & \alpha_H \end{pmatrix} \begin{pmatrix} \vec{E} \\ \vec{H} \end{pmatrix} \quad (3.1)$$

Research studies devoted to magneto-electric coupling in SRR confirm strong cross coupling terms in SRR caused by the geometry features which provides induced magnetic moment by H-

field in the same degree as by E-field [Katsarakis 2004; Marqués 2002]. Though magneto-electric coupling can be desirable for optical activity properties, it can also lead to negative effects, namely the increase of the electric dipole moment resulting in broadening of the resonance line.

SRR design operates well in microwave and near THz region, but doesn't demonstrate efficient magnetic response at optical frequencies. Besides the technological difficulties related to the fabrication of deep submicron size resonant metallic nanostructures, there are also fundamental issues related to the losses in metals at optical frequency that leads to saturation of the magnetic moment [Zhou 2005; Linden 2004; Enkrich 2005; Klein 2006; Khurgin 2012]. At the optical frequency the incident field penetrates into the metal on the skin depth that is comparable with the thickness of metallic resonator [Laman 2008]. The light energy is absorbed due to significant deviation of conductivity from that of a perfect metal and the inter-band transitions of electrons at high frequency.

The dispersion relation in metals is described by the Drude approximation, according to which the dielectric constant and conductivity depend on the frequency as:

$$\varepsilon(\omega) = 1 - \frac{\omega_p^2}{\omega^2 + i\omega\gamma} \quad (3.2)$$

$$\sigma(\omega) = \frac{\sigma_{DC}}{1 + i\frac{\omega}{\gamma}} \quad (3.3)$$

where  $\omega_p$  is plasma frequency,  $\gamma$  is relaxation rate and  $\sigma_{DC}$  is the DC conductivity of the metal. Hence, for far-THz frequencies, metals cannot be considered as perfect due to significant increase of absorption losses, contrary to the microwave and even near-THz domain. Now, accounting for the Drude conductivity, one can write the total energy density in a plasmonic resonator as [Urzhumov 2008]:

$$U_{tot} = \int_{V_m+V_v} d^2x \left( \frac{H_z^2}{8\pi} + \frac{E^2}{8\pi} \frac{\partial(\omega\varepsilon)}{\partial\omega} \right) = \int_{V_v} d^2x \frac{E^2}{8\pi} + \varepsilon_b \int_{V_m} d^2x \frac{E^2}{8\pi} + \frac{\omega_p^2}{\omega^2} \int_{V_m} d^2x \frac{E^2}{8\pi} + \int_{V_m+V_v} d^2x \frac{H_z^2}{8\pi} \quad (3.4)$$

where  $V_v$  and  $V_m$  are the vacuum and metallic volume respectively. The sum of the two first terms is the electric field energy  $U_E$ , the third one represents the kinetic energy of plasma electrons  $U_k$  and the fourth one defines the magnetic energy  $U_m$ . Magnetic energy similarly to the kinetic energy are of the order of  $\omega^{-2}$ , hence energy conservation is written as:

$$U_M + U_K = U_E \quad (3.5)$$

Thus, energy in resonator is stored quarter of period in the form of electric energy and the other quarter of period as sum of magnetic and kinetic energy of electrons that is further dissipated as thermal heat through collisions with phonons [Khurgin 2012]. The kinetic energy for convenience is usually expressed as additional inductance:

$$U_K = L_e I^2 / 2 \quad (3.6)$$

where  $L_e$  is the electron self-inductance determined electron inertia in metals. Notably,  $L_e$  scales inversely with size [Linden 2006], while the magnetic field inductance  $L_m$  scales proportionally to the character dimensions of SRR. For this reason, at high frequencies when the kinetic energy becomes prevailing it prevents efficient resonant behavior [Klein 2006; Urzhumov 2008; Khurgin 2012].

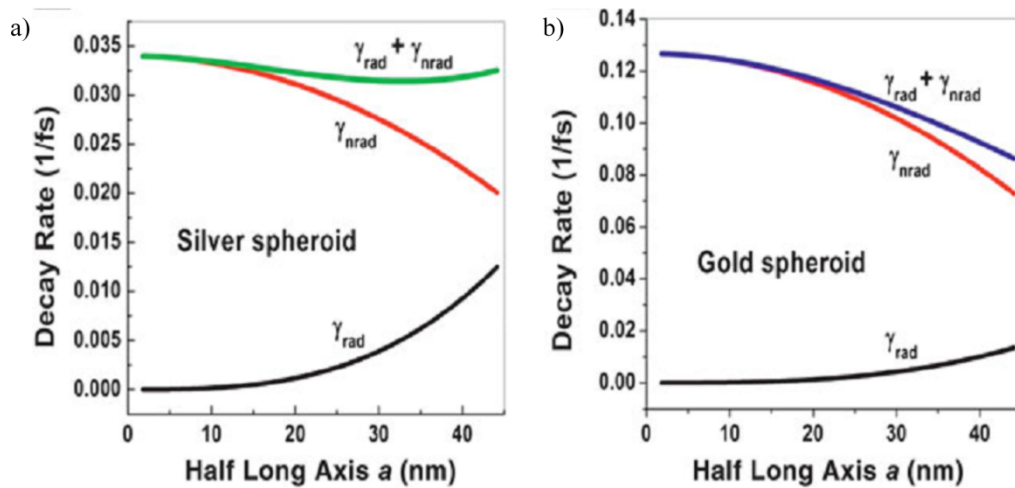


**Fig. 3.10.** Decay rate dependence of (a) silver and (b) gold spheroid from characteristic size [Khurgin 2012].

By consequence it was considered that when scaling down the size of subwavelength resonators at optical frequencies, the losses are for essential due to the non-radiative absorption in metals [Khurgin 2012]. However, as it can be seen from Fig. 3.10, when the size of a spherical metal scattering particle is 50 nm or higher, the contribution of radiative losses becomes comparable to the non-radiative one.

It follows from the above, that the issues for obtaining efficient magnetic response in high frequency region is are not only due to the limitations imposed by finite metal conductivity, but also because of radiative losses that are far from being negligible. The main contribution to radiative losses is brought through an electric dipole emission. By consequence the reduction of direct electric dipole excitation mechanism, as well as that caused by electro-magnetic coupling

is the key to the reduction of radiative losses. To achieve this we consider the symmetry matching approach introduced in the previous sections.

### 3.2.2. Symmetry matching for SRR

We start by considering the influence of magneto-electric coupling and symmetry matching with incident field polarization in a gold SRR at THz. We will focus on the oblique incidence configuration when magnetic field possesses non-zero normal projection in order to investigate SRR magnetic properties.

To this end we consider metallic resonant elements made of gold and use conductivity parameters given by Palik [Palik 1997]. The substrate used for simulations is glass with refractive index of 1.45 and zero tangential losses and the metal thickness is 50 nm. The design of single ring resonator is shown in Fig. 3.11. The unit cell dimensions are 600 nm by 470 nm. SRR inner and outer radius are 75 nm and 175 nm, respectively. The opening angle of the SRR's is  $120^\circ$ . The resonance frequency of SRR's with considered design falls in the NIR spectral region of 150-180 THz ( $1.66 - 2 \mu\text{m}$ ).

The SRR's design and incident field configuration is illustrated in Fig. 3.11. Under normal incidence for an electric field oriented along the  $y$ -axis the SRR's fundamental resonance occurs at 175 THz. The magnetic field does not contribute to the excitation of the fundamental resonance due to the absence of magnetic projection to the normal of the SRR. Hence, the induced current flow corresponds to that of  $y$ -axis oriented electric dipole. Under oblique incidence the extinction cross section depends only on  $\alpha_E$  and  $\alpha_H$  and is entirely independent of the magneto-electric coupling term  $\alpha_C$  [Sersic 2011].

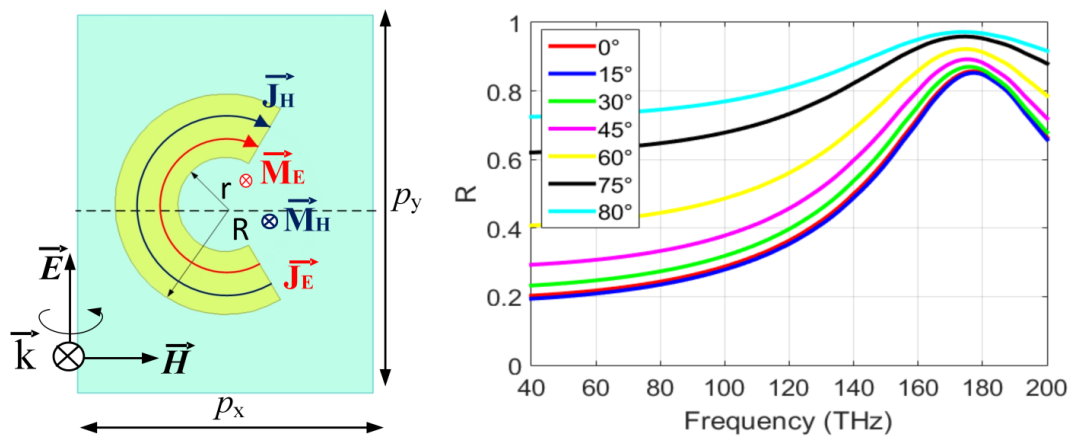


**Fig. 3.11. SRR under normal and oblique incidence when H-field penetrates the plane of SRR. Unit cell periods are  $p_x = 600$  nm and  $p_y = 470$  nm.**

It is intuitively clear that any notable contribution induced by the magnetic coupling  $\alpha_H$  may occur only in the vicinity of the resonance. Far from the resonance the contribution of this effect should be negligible. With this in mind, the important change of the reflection spectra as function of the incidence angle occurring, as it is evident from Fig. 3.11, even far from the resonance, cannot be attributed, at least totally, to the magnetic coupling. It is logically to suppose that the observed variation of reflection with the incidence angle is rather due to the change of Fresnel coefficients under oblique reflection from metasurface.

To verify this assumption and evaluate the importance of the contribution induced by the magnetic field component to the spectral response of SRR we use the effective medium approach. It consists to consider the MS as a homogeneous layer, which thickness is equal to that of a metal resonator (Fig. 3.12a). The effective dielectric permittivity is found in this case through the Nicolson-Ross-Weir (NRW) retrieval procedure greatly popularized in [Smith 2002]. The validity of such an approach when applied to a single metasurface layer operating in the optical domain was established in [Dubrovina 2012].

The first step of the employed procedure consisted in calculating the effective medium layer permittivity from complex reflection -  $S_{11}$  and transmission -  $S_{21}$  coefficients obtained by HFSS numerical modeling for normally incident on the SRR metasurface electromagnetic wave. Thus obtained permittivity, which closely follow a Lorentzian dispersion law, is used then to calculate oblique incidence reflection and transmission from effective medium layer using well-known textbook formula [Born 1975]. The superposed HFSS reflection spectra and those obtained by using effective medium layer model are traced in Fig. 3.12b. It can be seen that except in the near vicinity of the resonance frequency there is an almost perfect coincidence of two families of curves. The maximal deviation in reflection doesn't exceed 1%. Furthermore, it is doubtful that even this small deviation can be attributed to the magnetic coupling since some secondary effects, such as reported in some studies shift of the MS resonance frequency with the incidence angle were not taken into account. Otherwise the difference between HFSS and effective medium model results would be even smaller. By consequence, for this incident field configuration when the electric component is oriented along the y-axis, SRR's response is for essential determined by the induced electric dipole meaning that  $\alpha_E \gg \alpha_H$ .

To further verify this assumption we consider now the oblique incidence configuration depicted in Fig. 3.13 when the electric field coincides with SRR's symmetry axis. In this case, SRR polarizability depends only of  $\alpha_H$  [Sersic 2011]. Note that the two symmetrically distributed across SRR mirror axis currents are excited at a resonance frequency that is roughly twice higher

as compared to that of fundamental SRR mode. This resonance mode occurs out of the considered modeling frequency range and is not visible in the HFSS reflection spectra shown in Fig. 3.13. Meanwhile, for incidence angles higher than  $30^\circ$  a well distinguishable resonant feature can be observed in the frequency region of 170 THz that corresponds to the fundamental SRR resonance.

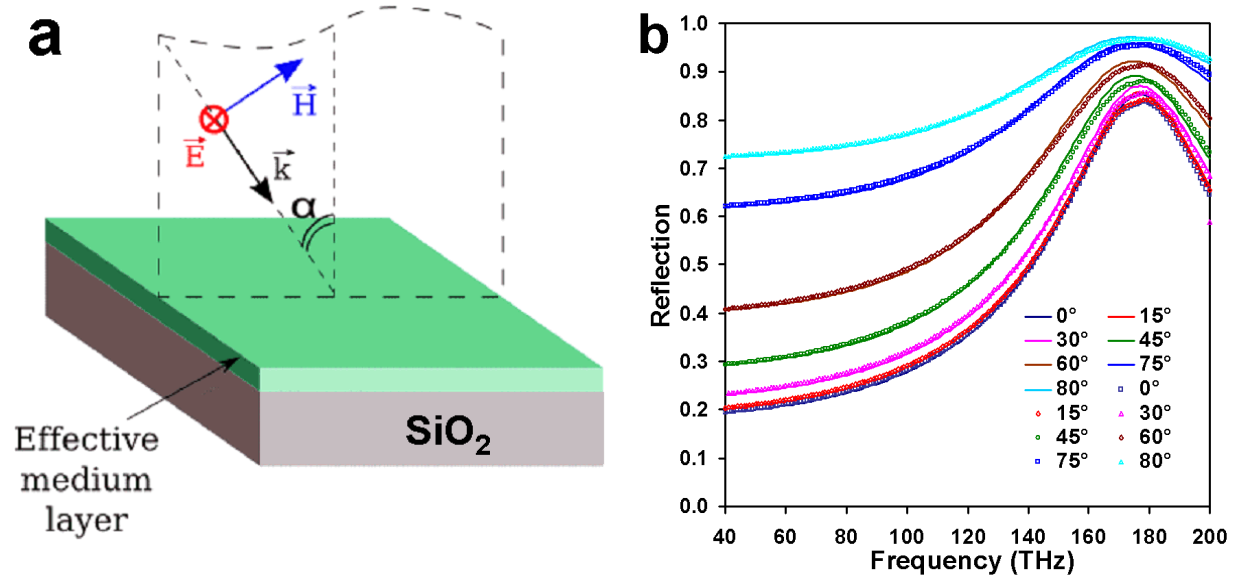


Fig. 3.12. (a) Effective medium layer model approximating single layer metasurface behavior in the optical domain. (b) SRR metasurface reflection spectra for different oblique incidence angles. Solid lines – HFSS numerical modeling results, symbols – effective medium layer model.

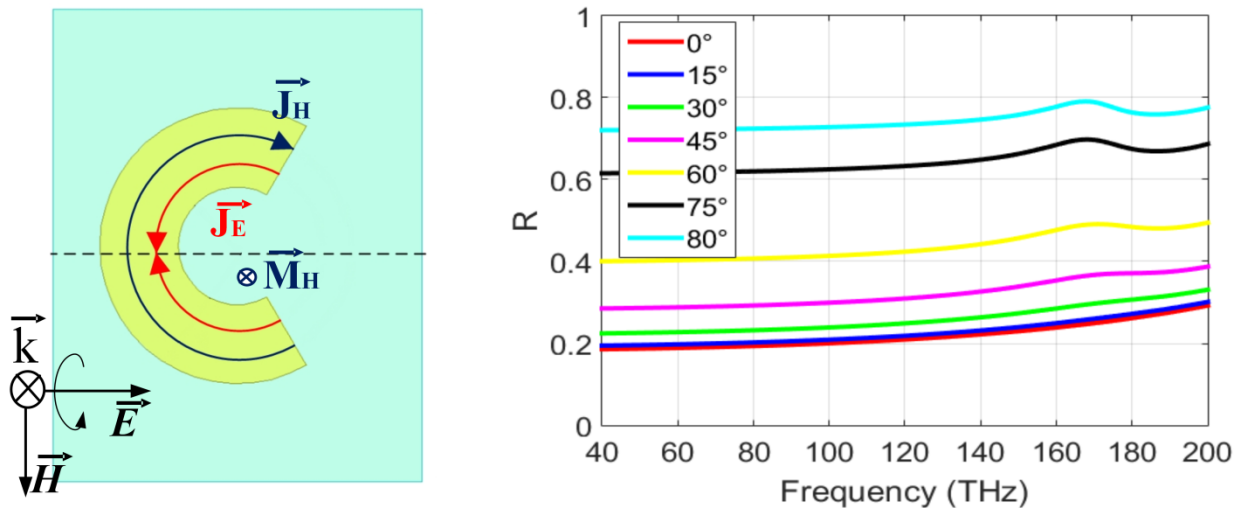
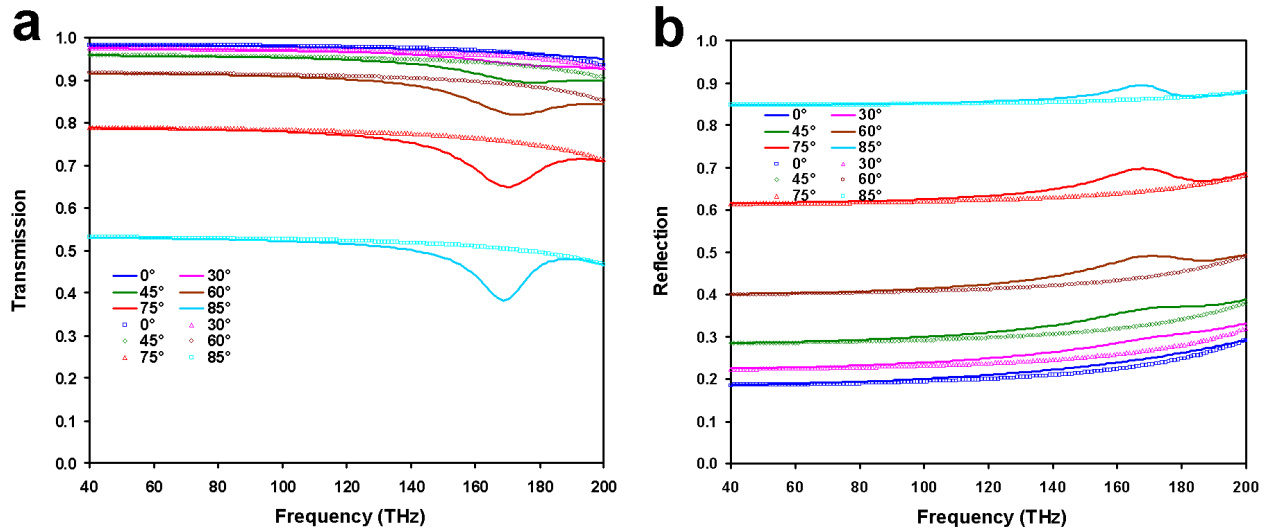


Fig. 3.13. SRR under normal and oblique incidence when E-field penetrates the plane of SRR. Unit cell periods are  $p_x = 470$  nm and  $p_y = 600$  nm.



**Fig. 3.14. SRR metasurface spectral characteristics. Solid lines – HFSS numerical modeling results, symbols – effective medium layer model. (a) Transmission. (b) Reflection.**

To separate the magnetic field component contribution from that induced by a mere variation under oblique of incidence Fresnel reflection coefficient, we apply the detailed above effective medium layer model. The superposed HFSS transmission and reflection spectra as well as those obtained by using effective medium layer model are traced in Fig. 3.14. It can be seen that this time there is a deviation between the two families of curves in the vicinity of the resonance frequency. However the maximal contrast in resonant reflection observed at the incidence angle of 75% is only around 10%. It is approximately twice higher  $\sim 20\%$  in transmission because of additional contribution of resonant absorption to the total extinction.

### 3.2.3. Magnetic dipole excitation based on symmetry matching

As follows from the above, using conventional design SRR at optical frequencies does not provide satisfactory results. The achievement of higher resonance quality factor requires the suppression of electric dipole contribution to the scattering process. As detailed in the section 3.1 this can be done by applying the symmetry matching approach and considering an antisymmetric arrangement of two connected SRR forming an S-shape resonator depicted in Fig. 3.15b. Such transformation results in inversion symmetry of resonant element relative to the polarization of E-field. As it has been discussed in the section devoted to the dark mode resonance mechanism of Z-shaped element, matching electric and magnetic symmetries with the resonator geometry strongly reduces the electric dipole moment. This excitation owing to symmetry features support net magnetic response as a sum of magnetic moments in the top and bottom part of S, which are

induced by magnetic coupling. Thus, this mechanism can greatly improve the magnetic response at the optical frequencies where losses are the principle obstacle.

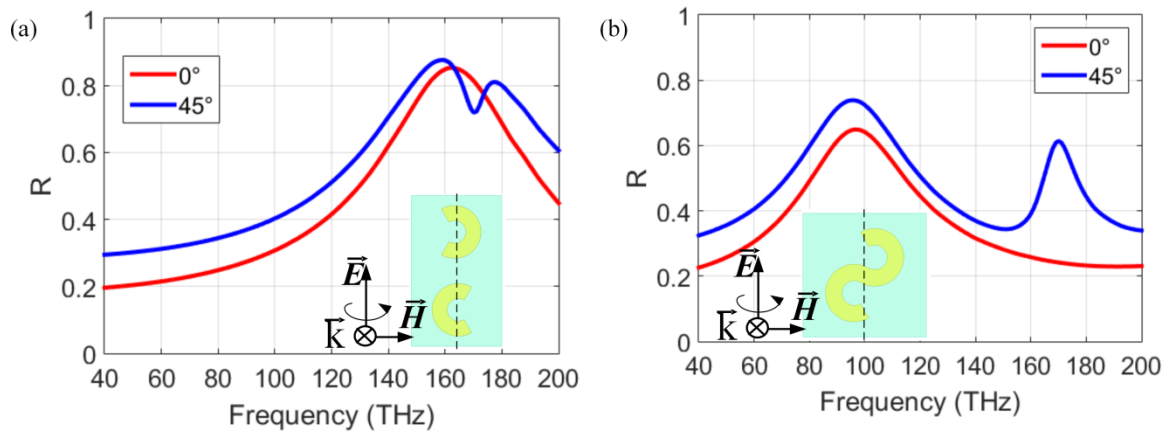


**Fig. 3.15. Normal and 45° oblique incidence reflection. (a) Two vertically aligned disconnected SRRs. (b) and S-element aligned along the direction of incident E-field.**

To demonstrate the difference between S-resonator and two vertically orientated SRRs we consider normal and 45° oblique incidence configurations represented in Fig. 3.15. The spectra obtained under normal incidence show that the fundamental resonance of S-MS occurs at the frequency of 98 THz (Fig. 3.15b). This resonance frequency is twice lower as compared with 178 THz in the case of two SRRs (Fig. 3.15a). The difference is due to the twice higher resonator length of S-element. Under oblique incidence in the S-MS a pronounced resonance is excited at 170 THz. It corresponds to the half of the S-resonator length. As evident, the contrast of the magnetic field component induced antisymmetric dark mode resonance occurring at 170 THz is notably higher as that of either a single SRR (Figs 3.11 and 3.13) or two disconnected SRRs (Fig. 3.15a).

Further below, the mechanism of resonance excitations in S-MS is detailed. Under normal incidence the interaction of S-MS with the electric component of the incident field leads to the excitation of fundamental electric dipole mode at 98 THz. The excitation of the first higher order mode is forbidden by symmetry. The antisymmetric dark mode is excited under oblique incidence through the magnetic component. At the dark mode resonance frequency two opposite currents are excited, as shown in Fig. 3.16c. The two magnetic dipoles induced by oppositely circulating currents in the loops formed by two antisymmetrically connected SRRs add together and contribute thus to the enhancement of  $\alpha_H$ . In contrast, the electric dipole moments induced by oppositely directed instantaneous currents cancel each other and resulting  $\alpha_E = 0$ . In the virtue of the optical stating that  $\alpha_C \leq \sqrt{\alpha_E \alpha_H}$  it follows that magneto-electric is also cancelled [Sersic

2011; Sersic 2012]. On this point there is a fundamental difference with the conventional SRR where  $\alpha_E \neq 0$  but magneto-electric coupling is null due to a particular orientation of linearly polarized light with respect to the SRR geometry [Sersic 2011]. Furthermore, following the fact that  $\alpha_C = 0$  and  $\alpha_E = 0$  it may be inferred that  $\alpha_H \approx 1$ , but the proof of this assertion requires an additional thorough theoretical analysis.

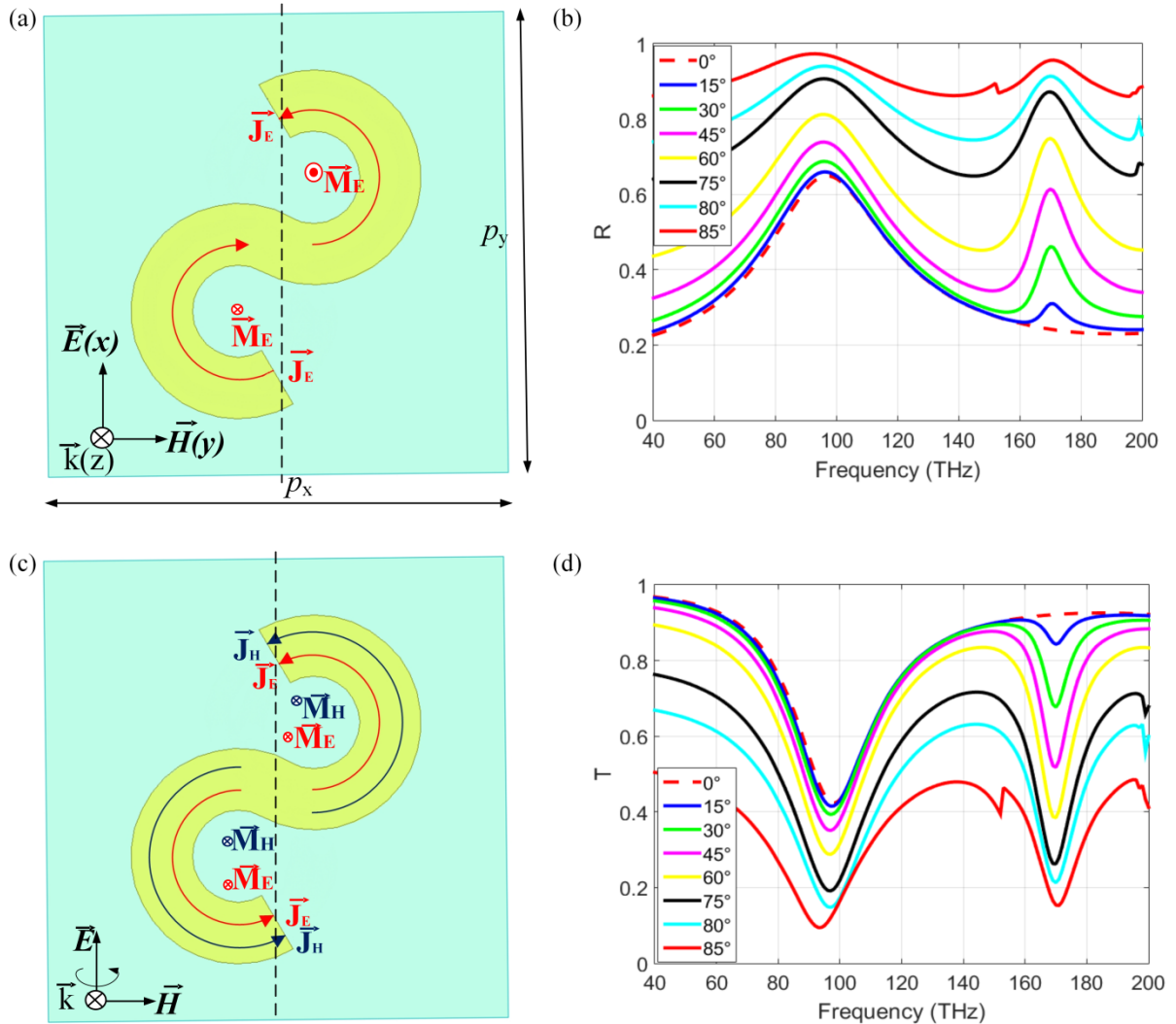


**Fig. 3.16. Sketch of S-shaped element under normal and oblique incidence. Unit cell dimensions are  $p_x = p_y = 750$  nm. (a) Schematic of fundamental mode instantaneous currents distribution. (b) HFSS numerical modeling results for reflection. (c) Schematic of dark mode instantaneous currents distribution. (d) HFSS numerical modeling results for transmission.**

As it can be noticed from transmission and reflection spectra shown in Fig. 3.16, the dark mode resonance contrast increases with the incidence angle due to the increased projection of magnetic field component penetrating the metasurface and, by consequence magnetic dipole excitation.

To demonstrate that magnetic field plays a substantial role for such dark mode excitation, transmission and reflection spectra obtained under different oblique incidence configuration are displayed in Fig. 3.17. Here under oblique incidence H-field remains parallel to the plane of S-metasurface and consequently, does not interact with the resonant element. In this case a fundamental resonance at 95 THz corresponding to the S-resonator length is observed similar to the previous configuration. The resonance at around 170 THz is only weakly excited under oblique incidence. This excitation is related to the different phase distribution of electric field in the unit cell. Thus, this additionally proves the magnetic nature of dark mode excitation provided by the considered symmetry matching approach.

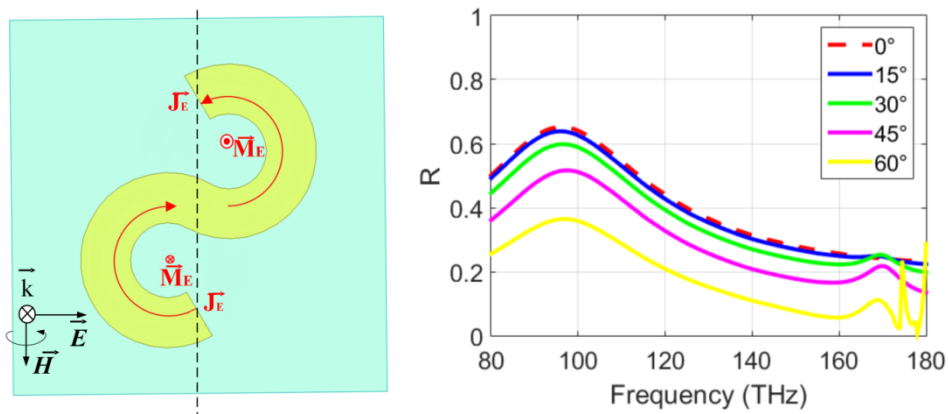


**Fig. 3.17. S-shaped element under normal and oblique incidence with H-field parallel to the plane of metasurface.**

#### 3.2.4. Design optimization

It should be noticed, that design of S-shaped resonator has been developed as a result of the parametric analysis. As has been discussed at the beginning of this Chapter, to maximize the dark mode resonance amplitude the edges and the center of the element should be aligned along the same axis parallel to the direction of the incident E-field. Z-shaped resonator, which functioning is quite acceptable in microwave frequency region, would be rather inefficient at optical frequencies. In the basic design of two connected V-antennas a key role is played by the opening angle or distance  $a$ , which is responsible for the strength of electric dipole moment, as shown in Fig. 3.18a. To demonstrate the influence of parameter  $a$  two different designs with  $a = 2.85$  mm and  $a = 4$  mm are presented in Figs. 3.18a and 3.18b, respectively. The rest of parameters such as resonator length  $l = 19.5$  mm, width  $w = 0.3$  mm and unit cell period  $p_x = p_y = 10$  mm are fixed. From reflection spectra shown in Figs. 3.18d and 3.18e is evident that dark

mode resonance is more intense for  $a = 4$  mm. For this design at the resonance the intensity of reflection  $I = 0.71$  is higher as compared to  $I = 0.55$  for the design with  $a = 2.85$  mm. Although the resonance line width also increases with intensity leading to reducing quality factor ( $Q = 16$  for  $a = 4$  mm and  $Q = 23$  for  $a = 2.85$  mm), significant enhancement of resonance strength is preferable due to considerably higher losses that would occur at optical frequencies.

Since the dark mode relies on interaction with magnetic field, it is important to optimize the design to maximize the surface of contour penetrated by magnetic field. The solution is the transformation of V-shaped geometry to the SRR resulting in S-shaped MS, as depicted in Fig. 3.18c. For fixed geometrical parameters, in particular  $a = 4$  mm, the surface of two V-antennas (Fig. 3.18b) and that of the S-resonator are  $S_v = 17.12$  mm and  $S_s = 27.6$  mm, respectively. As can be seen from respective spectra shown in in Fig. 3.18e and 3.18f, the intensity of dark mode is higher and of its intensity reaches  $I = 0.8$ , that is than  $I = 0.71$  for two V-antennas. However, the enhancement of magnetic dipole excitation provided by S-design, is accompanied by increase of radiative losses. For this reason the S resonator quality factor is lower  $Q = 13$ .

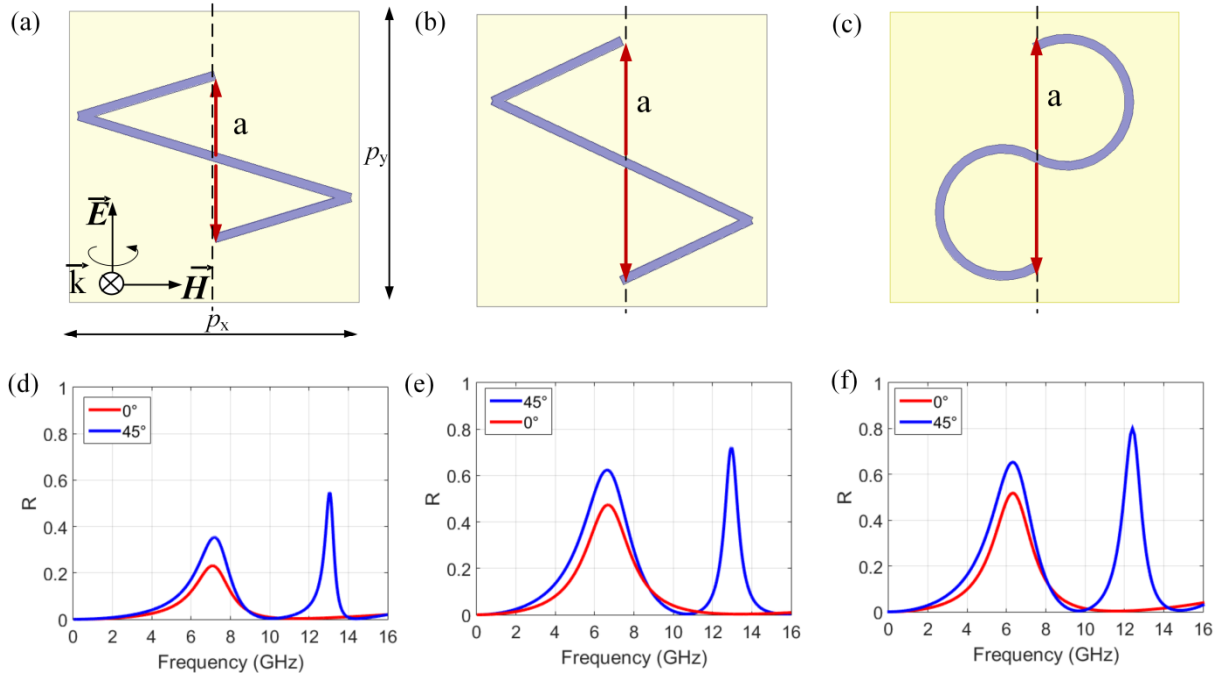


**Fig. 3.18. Design optimization for maximal dark mode amplitude.** Unit cell dimensions  $p_x = p_y = 10$  mm, resonator length  $l = 19.5$  mm, width of metallic wire  $w = 0.3$  mm, dielectric substrate is epoxy with  $\epsilon_r = 3.9$  and  $\tan \delta = 0.02$ . (a) and (b) two connected V-antennas with different distance  $a = 2.85$  mm and  $a = 4$  mm, respectively. (c) S-elements with  $a = 4$  mm. (d)-(f) Corresponding reflection intensity for normal and  $45^\circ$  oblique incidence.

The optimization of resonator shape in microwave domain is limited to considerations related to radiative losses. Further analysis is performed in optics to account for the specific high frequency operation regime.

Further discussion is devoted to selection of optimal S-design with respect to the arc length forming the S-element. To characterize this parameter we introduce the opening angle  $\alpha$ , as depicted in Fig. 3.19. As mentioned, to enhance the dark mode resonance in such type of design it is necessary to maximize the distance  $a$  and the surface of current contour interacting with magnetic field. The distance  $a$  is maximal for the opening angle  $\alpha = 90^\circ$ , as presented in Fig. 3.19a, however, this figure leads to minimal surface and decrease of resonator length. It is obvious, that surface becomes maximal for the entire circle. Hence, to find a balance between two parameters, two intermediate cases of  $\alpha = 60^\circ$  and  $\alpha = 45^\circ$  are considered as depicted in Figs. 3.19b and 3.19c. The unit cell dimensions used for numerical simulations are  $p_x = p_y = 750$  nm, the metal thickness  $h = 50$  nm, the outer and inner radius is  $R = 175$  nm and  $r = 75$  nm, respectively. The thickness of silicon dioxide substrate is  $3 \mu\text{m}$ . Such dimensions have been chosen to shift the resonance frequency in near infra-red optical region around 170 THz. From the calculated reflection spectra of two S-designs presented in Fig. 3.20a and 3.20b it can be observed that the amplitude of dark mode excitation is higher when  $\alpha = 60^\circ$ . For comparison, quality factors calculated for reflection intensity are  $Q = 12.5$  at intensity  $I = 0.24$  and  $Q = 13.1$  at  $I = 0.29$  for S with  $\alpha = 60^\circ$  and  $\alpha = 45^\circ$ , respectively.

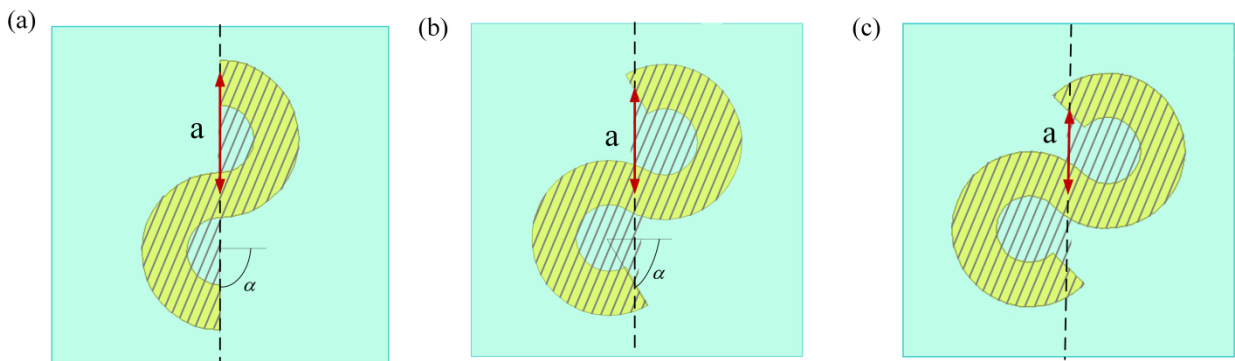


**Fig. 3.19. Evolution of S-design with decrease of opening angle  $\alpha$ . (a)  $\alpha = 90^\circ$ . (b)  $\alpha = 60^\circ$ . (c)  $\alpha = 45^\circ$ . Shaded area corresponds to effective surface of contour interacting with magnetic field.**

It should be emphasized that for an efficient dark mode excitation the orientation of S-element should correspond to the maximal projection of induced electric dipole with respect to the direction of incident electric field. As shown in Fig. 3.20c, the dark mode excited in vertical S is significantly weaker ( $I = 0.15$ ) as compared to S-design aligned to E-field shown in Fig. 3.20a.

In the optical frequency range because of the skin effect the position of resonance frequency strongly depends of the width of metallic resonant elements. For this reason, the analysis of how variation of resonator width influences on dark mode resonance was performed. At fixed outer radius the width is varied from 80 to 110 nm. The results obtained from numerical simulations are presented in Fig. 3.21 and Table 3.1. The case of  $w = 110$  nm exhibits narrowest resonance line, however, the resonance is shifted to higher frequencies where diffraction effect are observed. Hence, for experimental realization design with  $w = 100$  nm providing maximal intensity variation at resonance was selected.

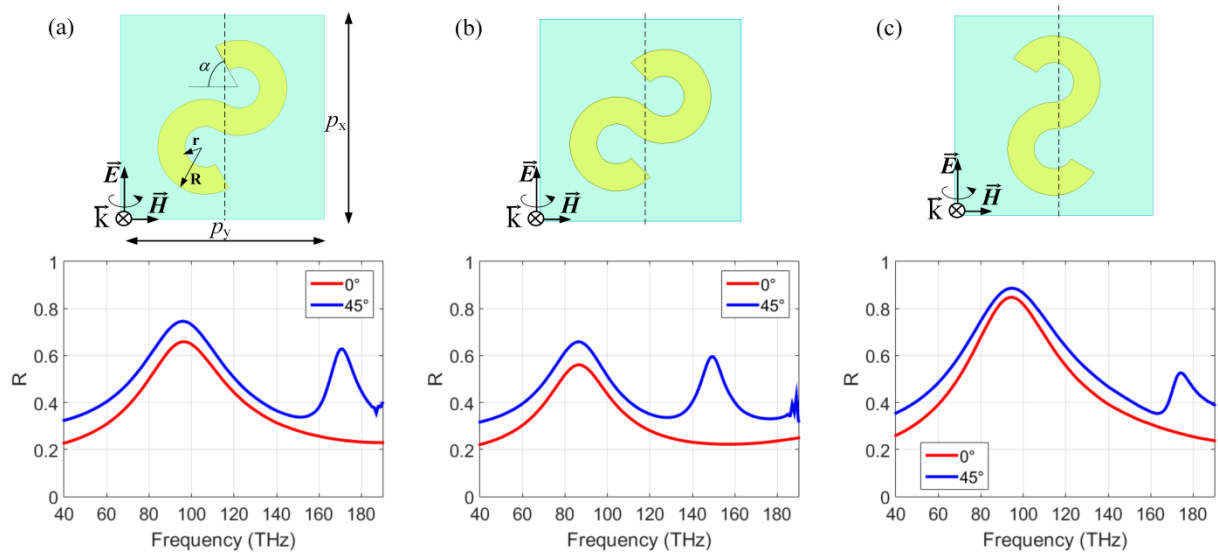


**Fig. 3.20. Design optimization.** Unit cell periods are  $p_x = p_y = 750$  nm, metallic thickness is  $h = 50$  nm, outer radius  $R = 175$  nm, inner radius  $r = 75$  nm, dielectric substrate is silicon dioxide. S-shaped elements with opening angle  $\alpha = 60^\circ$  (a),  $\alpha = 45^\circ$  (b). (c) Vertically aligned S-resonator with  $\alpha = 60^\circ$ .

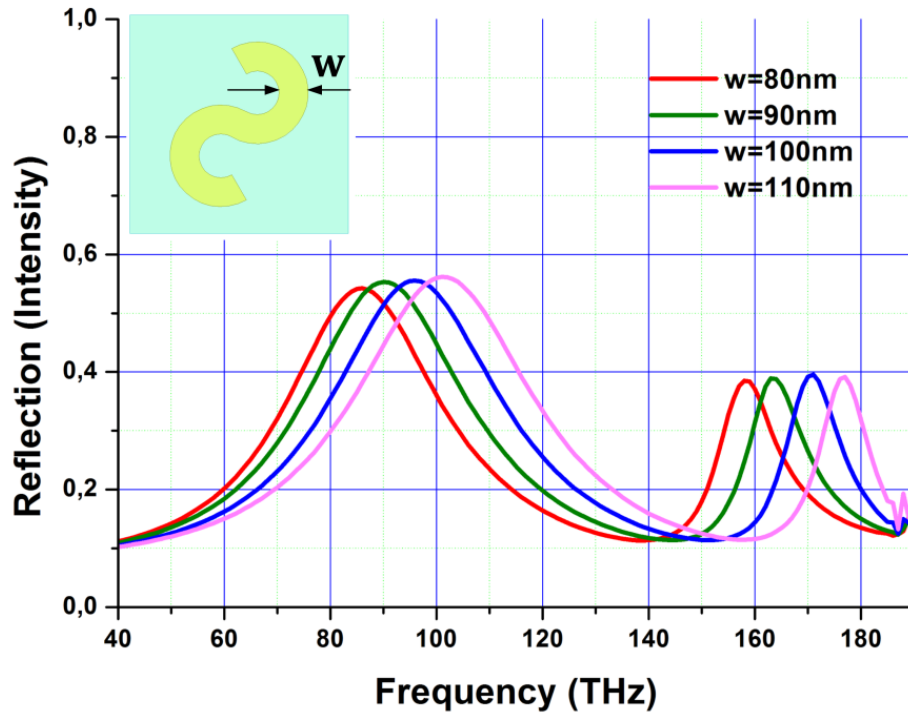


Fig. 3.21. Width variation for S-shaped element.

Width (nm)	Frequency (THz)	Intensity	Resonance width (THz)
80	159	0.27	13.5
90	164	0.28	13.5
100	171	0.29	13
110	176	0.28	11.3

Table. 3.1. Influence of resonant element width on dark mode resonance in S-shaped resonator.

### 3.2.5. Measurements

The defined through detailed above optimization procedure design was used for the fabrication of an experimental sample. Fabrication process is described in Section 2.6. The scanning electron microscope (SEM) image of the prototype is shown in Fig. 3.22. The experimental reflection spectra at normal and oblique incidence for TE and TM configurations are presented in Fig. 3.23a and b, respectively. The HFSS numerical simulations corresponding to this design are displayed in Figs. 3.16 and 3.17. As it can be seen in Fig. 3.23a a pronounced resonance appears at 170 THz for the TE mode at oblique incidence where the magnetic field component penetrates the S-resonator contour. In contrast, no excitation of dark mode resonance at 170 THz is observed for the oblique incidence configuration represented in Fig. 3.23b where H field

component remains parallel the plane of S-MS. The ensemble of experimental data are in excellent agreement with modeling results. Thus, the dark mode resonance related to the magnetic dipole excitation has been demonstrated numerically as well as experimentally in near infra-red optical domain.

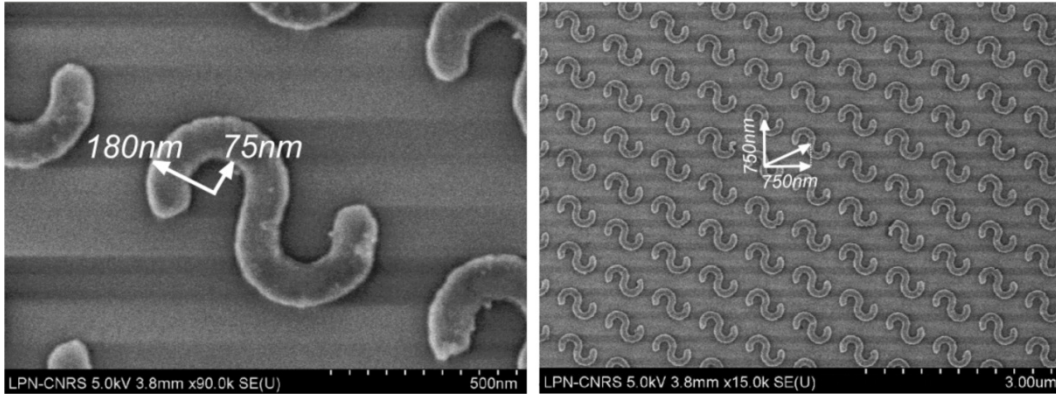


Fig. 3.22. Scanning electron microscope image of S-metasurface

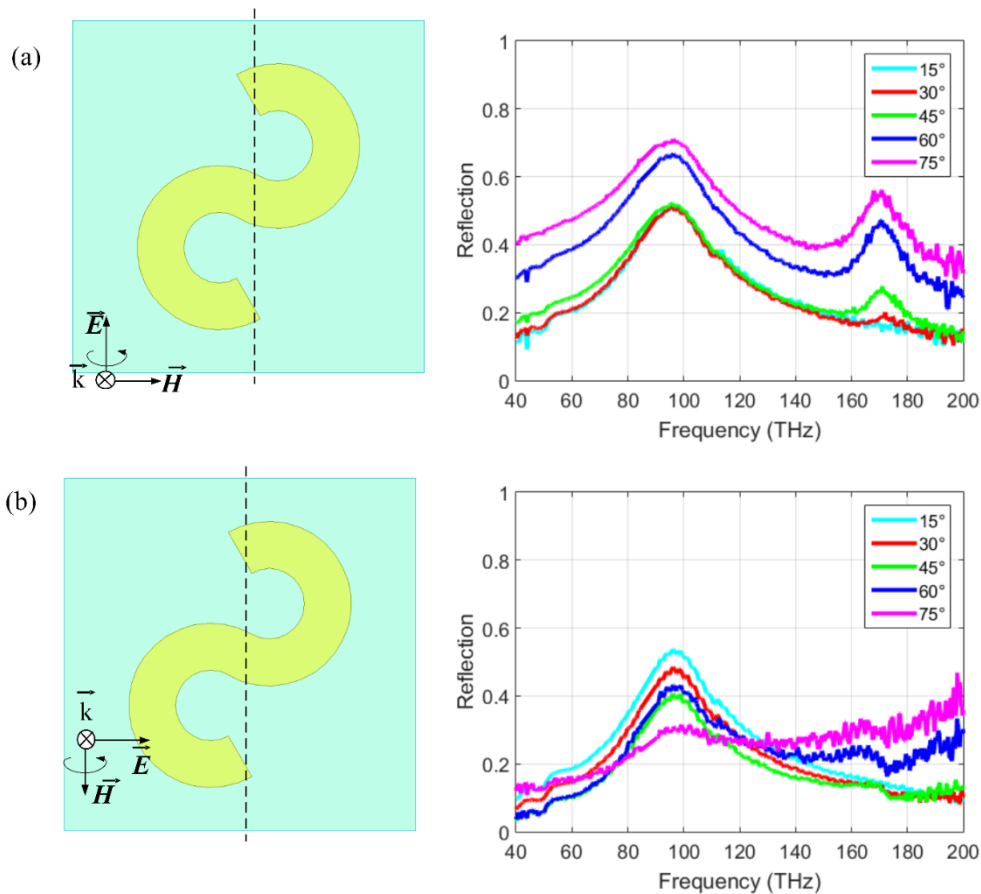


Fig. 3.23. Experimental results of dark mode magnetic dipole excitation in the S-shaped resonator. (a) Magnetic field penetrates the structure (TE mode). (b) Electric field penetrates the structure (TM mode).

### 3.3. Dark mode engineering based on complementary MSs

#### 3.3.1. Babinet's principle

The concept of complementary structure is an alternative way to engineer MSs. Such approach allows achieving electromagnetic behavior dual to original design [Guo 2012; Nakata 2013; Navarro-Ca 2010; Jia 2014; Liu 2008]. Engineering of complementary MSs is based on Babinet's principle which relates the total field of origin structure to the complementary configuration. For a thin, perfectly conducting plane metallic element **A** located at  $z = 0$  and illuminated from the region  $z < 0$  by incident field  $\mathbf{E}^0, \mathbf{B}^0$ , the complementary state is obtained as infinite thin metallic screen **B** with aperture which is identical to **A** and with complementary incident field  $\mathbf{E}_c^0$  and  $\mathbf{B}_c^0$  defined as [Jackson 1998]:

$$\begin{aligned}\vec{E}_c^0 &= c\vec{B}^0 \\ \vec{B}_c^0 &= -\frac{1}{c}\vec{E}^0\end{aligned}\quad (3.7)$$

Thus, the incident field with vertically polarized electric component and horizontally directed magnetic component for the metallic strip **A** is replaced by the vertical magnetic field and horizontal electric for complement structure **B** as it can be seen from Fig. 3.24. The total field for the origin structure in the shadowed side  $z > 0$  is given by the sum of source field and scattered field:

$$\mathbf{E} = \mathbf{E}^0 + \mathbf{E}'; \quad \mathbf{B} = \mathbf{B}^0 + \mathbf{B}'; \quad (3.8)$$

The scattered field of the complementary screen in the region  $z > 0$  are  $\vec{E}_c'$  and  $\vec{B}_c'$ , then the total field for the  $z < 0$  is written as [Falcone 2004; Baena 2005]:

$$\begin{aligned}\vec{E}_c &= \vec{E}_c^0 + \vec{E}_c^{0,r} + \vec{E}_c' \\ \vec{B}_c &= \vec{B}_c^0 + \vec{B}_c^{0,r} + \vec{B}_c'\end{aligned}\quad (3.9)$$

where  $\vec{E}_c^{0,r}$  and  $\vec{B}_c^{0,r}$  is the electric and magnetic field that would be reflected by metallic screen without any aperture. From the diffraction theory follows the relations between total field of the original structure and the scattered field for the complementary screen in the shadowed side  $z > 0$ :

$$\begin{aligned}E &= cB' \\ B &= -E'_c / c\end{aligned}\quad (3.10)$$

Hence, the total electric field from the original screen is related to scattered magnetic field from the complementary structure in the shadowed side  $z > 0$ . The equations relating the total field in the region  $z > 0$  for the original and complementary cases define Babinet's principle and are given as:

$$\begin{aligned} E - cB_c &= E^{(0)} \\ B + E_c / c &= B^{(0)} \end{aligned} \quad (3.11)$$

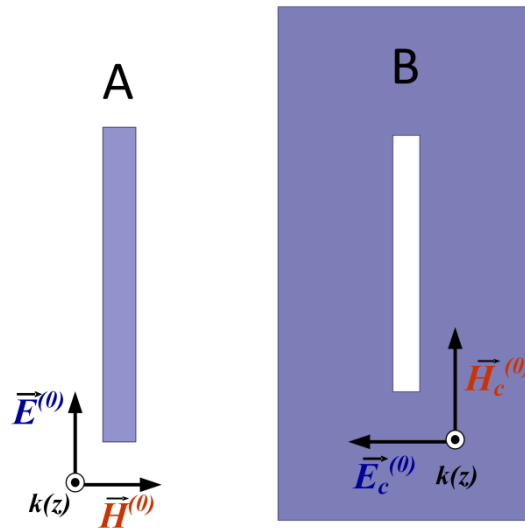


**Fig. 3.24. Original and complementary screens according to Babinet's principle. A is the metallic strip, B is infinite metallic screen with aperture which is equivalent to the strip A.**

The schematic behavior of electromagnetic field for the dual elements are presented in Fig. 3.25. Thus, according to Babinet's principle applied to the screens in Fig. 3.24, the radiation from the strip **A** with polarization of incident E-field along the strip is the same as that of metallic screen with slit aperture illuminated by the incident field with electric component perpendicular to the aperture. The scattered field of the metallic strip **A** is basically formed by the induced electric moment  $\mathbf{p}$ , then the screen **B** behaves as magnetic moment  $\mathbf{m}$  orientated as  $\mathbf{p}$  in the region  $z < 0$ . However, the continuity of the tangential/normal electric/magnetic field leads to the change of sign of induced polarizability at the transition from one side of the metallic plane to the other as shown in Fig. 3.25. Thus, for the metallic screen the normal component of electric field and the tangential component of magnetic field are oppositely directed with respect to the metallic plane.

This result can be extended to the case of an array of strips and slits if the subwavelength dimensions of the considered pattern are respected. The array of the strips at the resonance frequency produces the electric dipole moments and reflect all the incident radiation, while the

metallic plane consisting of the array of slits transmits the electromagnetic power, due to the interference with radiation reflected by metallic screen as it observed from equation (3.9).

It is important to point out, that Babinet's principle is totally valid only for infinite, thin perfectly conducting metallic screen, i.e. the behavior for original and complementary structures is absolutely dual. However, variation of these conditions such as finite metallic thickness, ohmic losses and the influence of dielectric substrate results in deviation from duality.

$$\begin{array}{ccc}
 \text{(a)} & & \text{(b)} \\
 E = E^0 + E' & E_c = E_c^0 + E_c^{0,r} + E' & E_c = E' \\
 B = B^0 + B' & B_c = B_c^0 + B_c^{0,r} + B' & B_c = B' \\
 \vec{p} \uparrow & & \vec{m} \uparrow \quad \vec{-m} \downarrow \\
 z < 0 \quad | \quad z > 0 & & z < 0 \quad | \quad z > 0
 \end{array}$$

**Fig. 3.25. Electromagnetic behavior of a metallic strip (a) and corresponding screen with aperture (b) illuminated by electromagnetic field from  $z < 0$ . The excited electric dipole in the strip corresponds to excitation of magnetic moment for the complementary screen, which change the sign according to the continuity principle.**

To conclude, complementary structures provide an engineering of dual electromagnetic properties, which allow to substitute resonance response from reflection to transmission and change the magnetic activity to electric and vice versa. It is obvious, that the phenomenon of dark mode and EIT can be also observed for the aperture designs which are complementary to the conventional metallic resonators. Several works have been devoted to EIT in metallic slot MSs based on strong coupling between apertures i.e. hybridization effect [Guo 2012; Liu 2008]. In with work, we will focus on the investigation of dark mode mechanism based on symmetry matching in a single element complementary structure. The study is performed at microwave frequencies by using as the original design the Z-shaped MSs described in the section 3.1.

### 3.3.2. Dark mode excitation in complementary MSs

Let us briefly remind the physics of the resonances excitation in the Z-shaped structure. The characteristic dimensions and incident field configuration are given in Fig. 3.26a. Under normal

incidence electric field orientated along y-axis excites the fundamental resonance at 4.6 GHz, corresponding to the induced electric dipole moment along the resonator length, as demonstrated on charge distribution in Fig. 3.26c. Under oblique incidence, when the electric field is parallel to the plane of MSs, but magnetic field penetrates the plane of structure, the additional resonance is observed at 13.7 GHz (Fig. 3.26b). This excitation represents two induced currents flowing in the opposite directions such that the net electric dipole moment is strongly suppressed, contrary to the net magnetic moment formed by current loops.

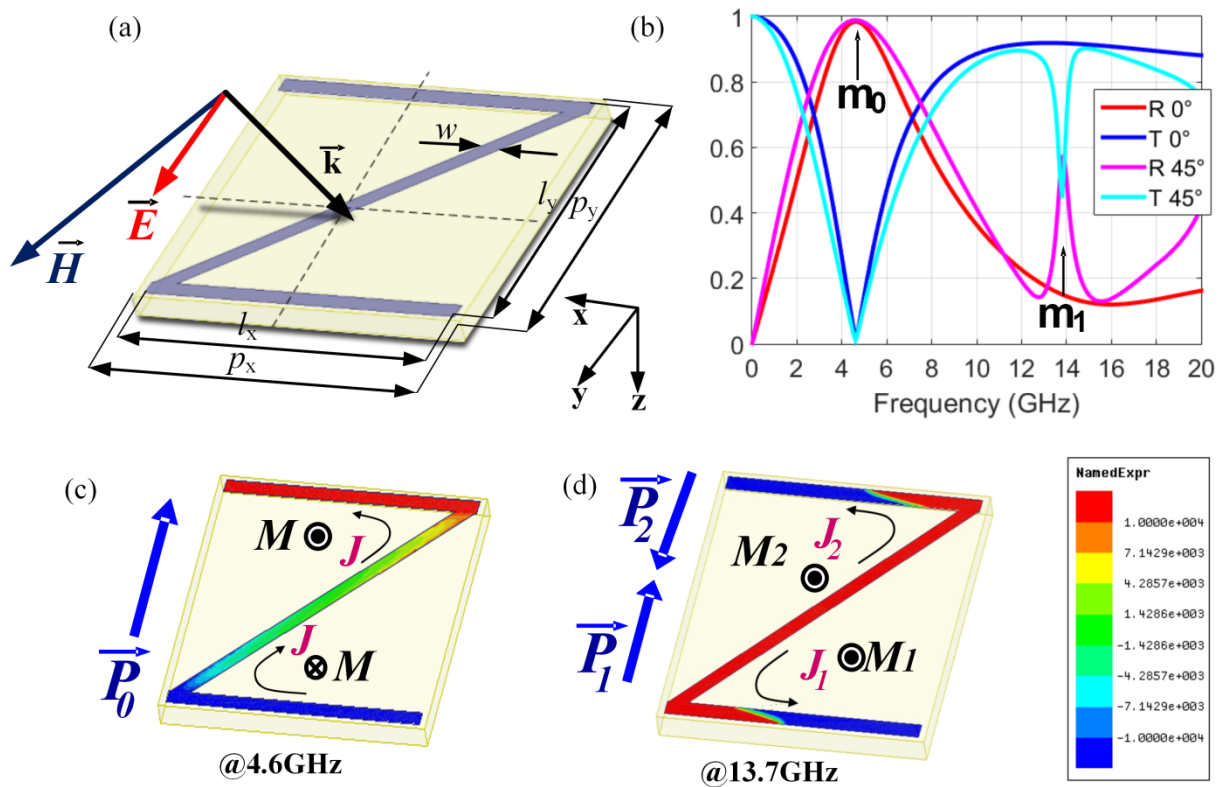
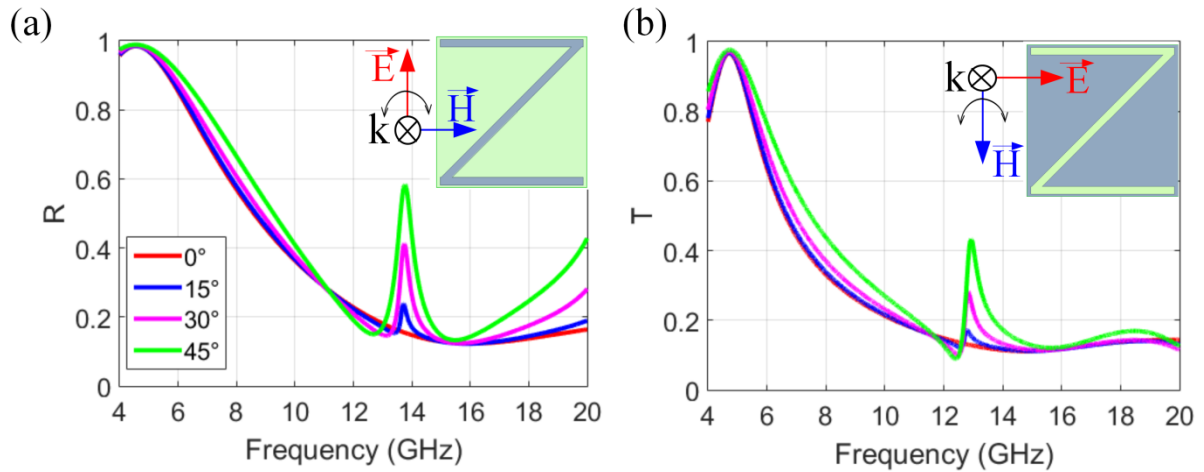


Fig. 3.26. Dark mode excitation in the Z-shaped MSs. (a) Schematic design. (b) Spectral characteristics under normal and oblique incidence. Charge distribution for (c) fundamental at 4.6 GHz and (d) dark mode at 13.7 GHz resonances.

Now we introduce complementary screen for the Z-shaped metasurface as displayed in the inset of Fig. 3.27b. According to Babinet's principle, polarization of complementary incident field is such that electric field becomes horizontally orientated while the magnetic field is vertically polarized. As it has been expected, the peak in transmission for dual structure replaces the maximum in reflection for the original case. The slight difference in the positions of resonance frequency and deviation in the line shape can be explained by the presence of dielectric substrate supporting metal sheet in the complementary design. As can be seen from Fig. 3.27b, the dark

mode is excited at 12.9 GHz under oblique incidence when electric field penetrates through the metasurface. The resonance amplitude increases with the incident angle due to augmentation of normal projection of external E-field, while the original metasurface is sensitive to normal magnetic field component.



**Fig. 3.27. Dual behavior for Z-shaped resonator. (a) Reflection for the original Z. (b) Transmission for the complementary Z.**

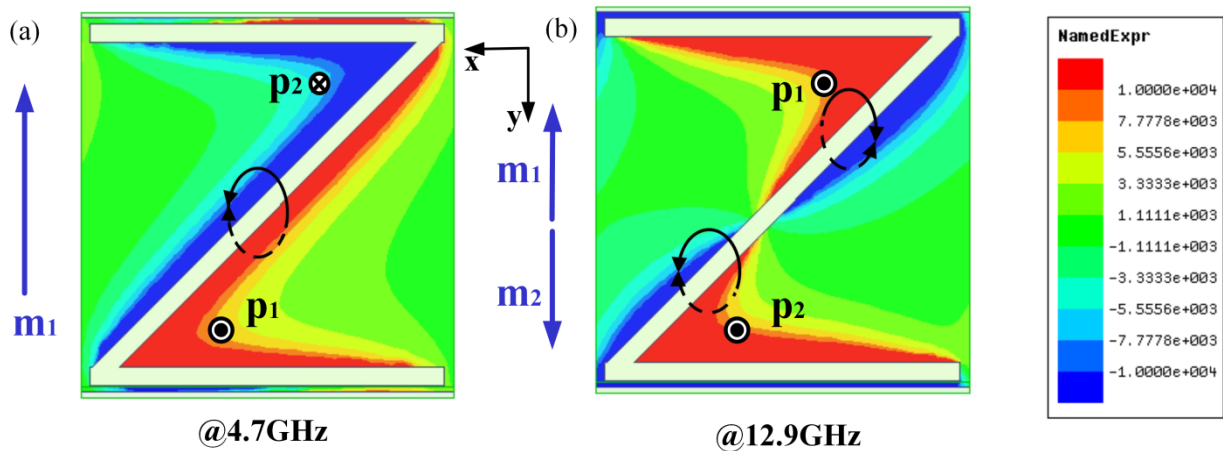


**Fig. 3.28. Charge distribution for complementary Z-structure. (a) Fundamental mode. (b) Dark mode.**

To understand excitation mechanism, let us demonstrate the agreement between simulated charge distribution for both fundamental and dark modes with predictions given by Babinet's principle. If fundamental resonance of Z corresponds to electric dipole excitation along y-axis, then according to Babinet's principle the resonance in the Z-shaped aperture is related to the magnetic dipole excitation, as illustrated in Fig. 3.24a. This magnetic field induces axial electric field as shown in Fig. 3.28a. The mirror symmetry of the electric lines with respect to the

metallic plane relies on the continuity of normal component of electric field. The electric field vectors coincide with excited charge distribution, where the positive and negative charges are located on the different sides of slot. It should be noticed that two opposite magnetic moments  $\mathbf{M}$  orthogonal to the MSs formed by the current loops in the original Z-element (Fig. 3.26c). For the complementary Z, there are two areas with positive and negative charge in the corners of Z-resonator, characterized by opposite electric vectors for the each semi-space with respect to the metallic plane.

As it has been shown and detailed in the section 3.3.1, the dark mode resonance in the Z-MSs corresponds to the excitation of two co-directional magnetic dipole moment along  $z$ -axis and two opposite electric moments parallel to the  $x$ -axis resulting in vanishingly low net electric dipole radiation (Fig. 3.26d). Therefore, corresponding dark mode for complementary Z observed at 12.9 GHz is related to the excitation of two opposite magnetic dipoles along  $y$ -axis as depicted in Fig. 3.28b. Consequently, two different directions of axial electric field are induced as it can be evidenced by charge distribution in Fig. 3.28b. Two co-directed normal magnetic moments excited in simple Z correspond to two normal electric moments (for each side of metasurface) orientated in the same direction that agree with identical charge in the corners of Z.

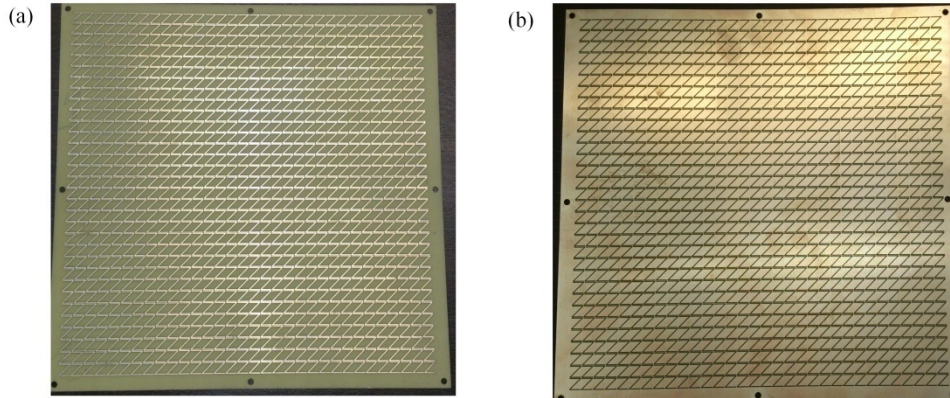


**Fig. 3.29. Prototypes of Z-MS (a) and complementary configuration (b).**

It should be noticed that dark mode for complementary structure also exhibits significant increase of quality factor of  $Q_{\text{fund}} = 1.8$  compared to fundamental resonance  $Q_{\text{dark}} = 27$  as shown in Fig. 3.30b and d. The deviation from original Z-MS, where  $Q_{\text{fund}} = 0.85$  and  $Q_{\text{dark}} = 28$ , results from less absorption in dielectric substrate due to less uncovered dielectric surface.

In order to validate the presented results experimentally, prototypes of Z-shaped and complementary Z metasurface were fabricated (Fig. 3.29). Total sample size is  $35 \times 35$  cells on a  $210 \text{ mm} \times 210 \text{ mm}$  dielectric substrate. The material parameters of the substrate and the

### 3.3 Dark mode engineering based on complementary MSs

geometrical dimensions used for the experimental validation are the same as in numerical simulations. The experimental setup for microwave transmission measurements has been described in Chapter 2. Experimental results are in a excellent agreement with numerical modeling as shown in Fig. 3.30.

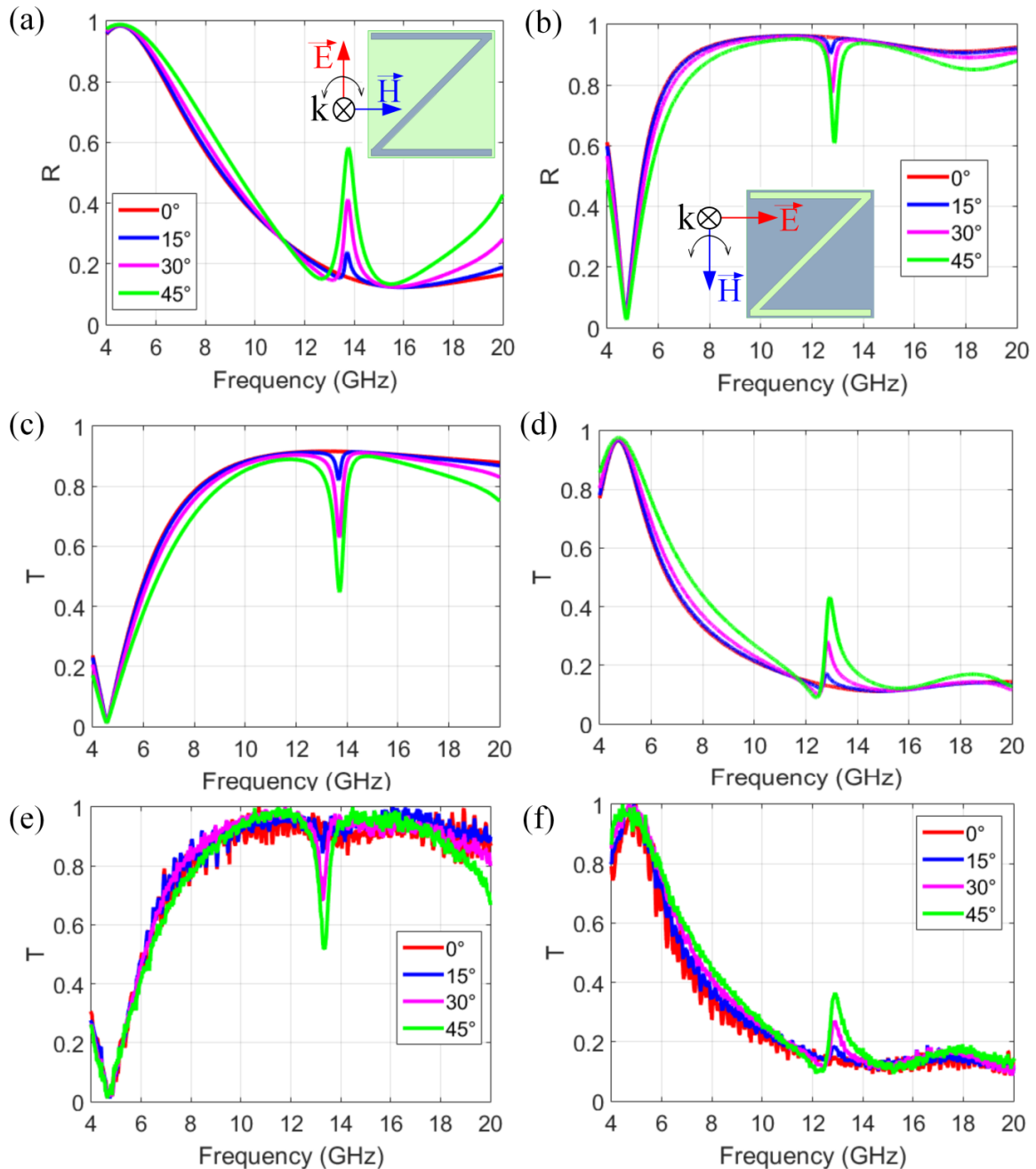


**Fig. 3.30. Simulated (a)-(d) and measured (e)-(f) spectral characteristics under normal and oblique incidence for simple (left column) and complementary (right column) Z-resonator.**

Thus, dual electromagnetic behavior provided by complementary MSs has been demonstrated not only for fundamental resonance but also for the dark mode resonance. In turn, this allows

obtaining higher quality factor resonance for maximum in reflection as well as maximum in transmission depending on the type of MSs used. Moreover, the proposed dark mode resonance mechanism based on symmetry matching conditions allows enhancing the efficiency of magnetic dipole excitation or electric dipole excitation by engineering metallic or complementary designs.

### **3.4. Conclusion**

To conclude, dark mode resonance allows achieving sharper spectral response as compared to the fundamental resonance. This feature is highly beneficial for sensing applications and also for optic modulation and switching. Most of the approaches reported in the literature are based on the hybridization mechanism of two resonant elements associated with bright and dark mode. In contrast, our method is not related to any mode hybridization and relies only on symmetry matching approach. It consists to design appropriate geometry that allows matching currents excited by the incident electric and magnetic fields to provide dark mode excitation. Such resonance represents magnetic dipole excitation with vanishingly low net electric dipole moment. It has been demonstrated, that proposed approach allows achieving more efficient magnetic response compared to conventional split ring resonator at optical frequencies. Moreover, symmetry matching approach has been extended to the complementary MSs providing more flexibility in dark mode engineering.

## References

- [Anker 2008] J.N. Anker et al., 2008. “Biosensing with plasmonic nanosensors”. *Nature Materials*, 7, pp.442-453.
- [Baena 2005] J.D. Baena et al., 2005. “Equivalent-circuit models for split-ring resonators and complementary split-ring resonators coupled to planar transmission lines”. *IEEE Transactions on Microwave Theory and Techniques*, 53, pp.1451-1461.
- [Baena 2007] J.D. Baena, L. Jelinek & R. Marqués, 2007. “Towards a systematic design of isotropic bulk magnetic metamaterials using the cubic point groups of symmetry”. *Physical Review B*, 76.
- [Born 1975] M. Born & E. Wolf, 1975. Principles of Optics: Electromagnetic Theory of Propagation, Interference and Diffraction of Light.
- [Burokur 2015] S.N. Burokur, A. Lupu & A. Lustrac, 2015. “Direct dark mode excitation by symmetry matching of a single-particle-based metasurface”. *Physical Review B*, 91.
- [Cao 2012] W. Cao et al., 2012. “Low-loss ultra-high-Q dark mode plasmonic Fano metamaterials”. *Optics Letters*, 37, p.3366.
- [Chiam 2009] S.-Y. Chiam et al., 2009. “Analogue of electromagnetically induced transparency in a terahertz metamaterial”. *Physical Review B*, 80.
- [Dubrovina 2012] N. Dubrovina et al., 2012. “Single metafilm effective medium behavior in optical domain: Maxwell–Garnett approximation and beyond”. *Applied Physics A*, 109, pp.901-906.
- [Enkrich 2005] C. Enkrich et al., 2005. “Magnetic Metamaterials at Telecommunication and

Visible Frequencies”. *Physical Review Letters*, 95.

- [Falcone 2004] F. Falcone et al., 2004. “Babinet Principle Applied to the Design of Metasurfaces and Metamaterials”. *Physical Review Letters*, 93.
- [Guo 2012] Y. Guo et al., 2012. “Electromagnetically induced transparency (EIT)-like transmission in side-coupled complementary split-ring resonators”. *Optics Express*, 20, p.24348.
- [Jackson 1998] J.D. Jackson, 1998. *Classical Electrodynamics*.
- [Jia 2014] Y.-P. Jia et al., 2014. “Complementary chiral metasurface with strong broadband optical activity and enhanced transmission”. *Applied Physics Letters*, 104, p.011108.
- [Katsarakis 2004] N. Katsarakis et al., 2004. “Electric coupling to the magnetic resonance of split ring resonators”. *Applied Physics Letters*, 84, pp.2943-2945.
- [Khurgin 2012] J.B. Khurgin & A. Boltasseva, 2012. “Reflecting upon the losses in plasmonics and metamaterials”. *MRS Bulletin*, 37, pp.768-779.
- [Klein 2006] M.W. Klein et al., 2006. “Single-slit split-ring resonators at optical frequencies: limits of size scaling”. *Optics Letters*, 31, p.1259.
- [Lal 2007] S. Lal, S. Link & N.J. Halas, 2007. “Nano-optics from sensing to waveguiding”. *Nature Photonics*, 1, pp.641-648.
- [Laman 2008] N. Laman & D. Grischkowsky, 2008. “Terahertz conductivity of thin metal films”. *Applied Physics Letters*, 93, p.051105.
- [Linden 2004] S. Linden, 2004. “Magnetic Response of Metamaterials at 100 Terahertz”. *Science*, 306, pp.1351-1353.

- [Linden 2006] S. Linden et al., 2006. "Photonic Metamaterials: Magnetism at Optical Frequencies". *IEEE Journal of Selected Topics in Quantum Electronics*, 12, pp.1097-1105.
- [Liu 2008] N. Liu, S. Kaiser & H. Giessen, 2008. "Magnetoinductive and Electroinductive Coupling in Plasmonic Metamaterial Molecules". *Advanced Materials*, 20, pp.4521-4525.
- [Liu 2009] N. Liu et al., 2009. "Plasmonic analogue of electromagnetically induced transparency at the Drude damping limit". *Nature Materials*, 8, pp.758-762.
- [Liu 2010] N. Liu et al., 2010. "Planar Metamaterial Analogue of Electromagnetically Induced Transparency for Plasmonic Sensing". *Nano Letters*, 10, pp.1103-1107.
- [Luk'yanchuk 2010] B. Luk'yanchuk et al., 2010. "The Fano resonance in plasmonic nanostructures and metamaterials". *Nature Materials*, 9, pp.707-715.
- [Marques 2002] R. Marques, F. Medina & R.R. El-Idrissi, 2002. "Role of bianisotropy in negative permeability and left-handed metamaterials". *Physical Review B*, 65.
- [Nakata 2013] Y. Nakata, Y. Urade, T. Nakanishi & M. Kitano, 2013. "Plane-wave scattering by self-complementary metasurfaces in terms of electromagnetic duality and Babinet's principle". *Physical Review B*, 88.
- [Navarro-Ca 2010] M. Navarro-Ca et al., 2010. "Stacked complementary metasurfaces for ultraslow microwave metamaterials". *Applied Physics Letters*, 96, p.164103.
- [Padilla 2007] W.J. Padilla, 2007. "Group theoretical description of artificial electromagnetic metamaterials". *Optics Express*, 15, p.1639.
- [Palik 1997] E.D. Palik, 1997. Handbook of Optical Constants of Solids.

- [Prodan 2003] E. Prodan, 2003. "A Hybridization Model for the Plasmon Response of Complex Nanostructures". *Science*, 302, pp.419-422.
- [Reinke 2011] C.M. Reinke et al., 2011. "Group-theory approach to tailored electromagnetic properties of metamaterials: An inverse-problem solution". *Physical Review E*, 83.
- [Sersic 2011] I. Sersic, C. Tuambilangana, T. Kampfrath & A.F. Koenderink, 2011. "Magnetoelectric point scattering theory for metamaterial scatterers". *Physical Review B*, 83.
- [Sersic 2012] I. Sersic, M.A. van de Haar, F.B. Arango & A.F. Koenderink, 2012. "Ubiquity of Optical Activity in Planar Metamaterial Scatterers". *Physical Review Letters*, 108.
- [Smith 2002] D.R. Smith, S. Schultz, P. Marko & C.M. Soukoulis, 2002. "Determination of effective permittivity and permeability of metamaterials from reflection and transmission coefficients". *Physical Review B*, 65.
- [Smith 2006] D.R. Smith, D. Schurig & J.J. Mock, 2006. "Characterization of a planar artificial magnetic metamaterial surface". *Physical Review E*, 74.
- [Tassin 2009] P. Tassin et al., 2009. "Low-Loss Metamaterials Based on Classical Electromagnetically Induced Transparency". *Physical Review Letters*, 102.
- [Urzhumov 2008] Y.A. Urzhumov & G. Shvets, 2008. "Optical magnetism and negative refraction in plasmonic metamaterials". *Solid State Communications*, 146, pp.208-220.
- [Willetts 2007] K.A. Willetts & R.P.V. Duyne, 2007. "Localized Surface Plasmon Resonance Spectroscopy and Sensing". *Annual Review of Physical Chemistry*, 58, pp.267-297.

- [Wongkasem 2006] N. Wongkasem, A. Akyurtlu & K.A. Marx, 2006. "Group theory based design of isotropic negative refractive index metamaterial". *Progress In Electromagnetics Research*, 63, pp.295-310.
- [Zhang 2008] S. Zhang et al., 2008. "Plasmon-Induced Transparency in Metamaterials". *Physical Review Letters*, 101.
- [Zhou 2005] J. Zhou et al., 2005. "Saturation of the Magnetic Response of Split-Ring Resonators at Optical Frequencies". *Physical Review Letters*, 95.



## Chapter 4.

### Fano resonance in Metasurface cavity

After discussing of methods providing narrow resonance characteristics in individual element, the resonance phenomena in the more complex structures of coupled resonators are considered. The interaction between resonant particles essentially depends on the separation distance between resonant elements and their arrangement. Two fundamentally different coupling mechanisms can be distinguished in relation to the separation distance between elements: coupling via near-field and coupling via far-field (Fig. 4.1). Near-field coupling may lead to plasmon resonance frequency shift or to mode hybridization resulting in appearance of two normal modes. As it has been discussed in Chapter 2, sharp Fano resonance can be observed in the vicinity of anti-symmetric mode. Near-field coupling attenuates with increased separation distance between two layers of resonant particles. When the separation distance becomes larger than the wavelength corresponding to plasmon resonance, the resonators couple through far-field due to significant phase difference of electromagnetic field for the elements. This provides the ultra-narrow cavity modes in the vicinity of the plasmon resonance frequency similarly to conventional Fabry-Perot cavity. Thus, metasurface cavity provides narrow resonance characteristics for different interaction regimes. The aim of this Chapter is to find the optimal geometry configuration and separation distance of metasurface cavity in view of sensing ability.

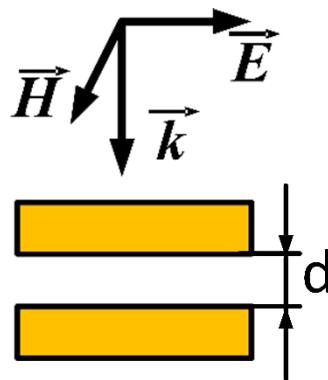


Fig. 4.1. Schematic of two coupled plasmon resonators with separation distance  $d$ .

To describe the resonance process in coupled resonator system we used theoretical approach based on coupled mode theory. The conventional methods intended to describe resonance behavior in the plasmon system of coupled resonators, such as fitting with classical phenomenological models of coupled oscillators [Klein 2005; Lovera 2013] and fitting with a

Fano model [Genet 2003; Gallinet 2011], rely only on interaction between resonance modes without accounting for the open character of plasmon MSs systems, i.e. free coupling to propagation radiation. In contrast, temporal coupled mode theory (TCMT) developed for optical resonators takes into account features of open system, namely, the existence of two scattering pathways, either direct propagation or indirect one via resonance [Suh 2004; Fan 2003; Lepetit 2010; Yoon 2012; Kodigala 2015]. The interference of these two channels may lead to asymmetric Fano resonance. By using TCMT one can predict scattering parameters on basis of resonator characteristics such as resonators frequencies, damping factors and near field coupling coefficients. Moreover, TCMT can be used to describe the behavior of metasurface cavity with large separation distance since it accounts for the far-field coupling. Further, the basic ideas of this approach are presented.

#### 4.1. Basic equations of Temporal Coupled Mode Theory

Formalism of TCMT was developed by Haus [Haus 1984] for optical cavity systems. Later, this method was exploited to describe Fano resonance in photonic crystal structures [Suh 2005; Fan 2003]. TCMT is valid for a weak coupling regime when the resonance width is smaller than the resonance frequency that allows to assume the coupling constant as frequency independent.

For the simplest case of closed system the dynamic equation for resonance amplitudes is described as:

$$\frac{d\mathbf{a}}{dt} = j\mathbf{\Omega}\mathbf{a} \quad (4.1)$$

where  $\mathbf{\Omega}$  represents resonance frequencies. If the system possesses  $n$  resonance modes, which can couple to each other, the off-diagonal elements of  $\mathbf{\Omega}$  represent coupling between resonances. Since the system is conservative in the absence of gain and loss,  $\mathbf{\Omega}$  is Hermitian matrix and, consequently, the eigenmodes of this matrix are real and form an orthogonal basis.

For the open system, when the resonator freely interacts with propagation radiation, the evolution of the system is due to the sum of resonance contribution and non-resonance propagation. The general form of dynamics equations for the open system can be given by a set of coupled ordinary differential equations [Suh 2005; Suh 2004; Fan 2003]:

$$\frac{d\mathbf{a}}{dt} = j(\mathbf{\Omega} + j\mathbf{\Gamma}_A + j\mathbf{\Gamma}_R)\mathbf{a} + \mathbf{K}_+^T \mathbf{s}_+ \quad (4.2)$$

$$\mathbf{s}_- = \mathbf{C}\mathbf{s}_+ + \mathbf{K}_- \mathbf{a} \quad (4.3)$$

Код п  
 Отфо  
 (Фран  
 правс  
 Код п  
 Код п  
 Отфо  
 (Фран  
 правс  
 Код п  
 Код п  
 Отфо  
 (Фран  
 правс  
 Отфо  
 (Фран  
 правс

## 4.1 Basic equations of Temporal Coupled Mode Theory

Here, lowercase bold letters designate vectors whereas uppercase bold letters designate matrices.  $\boldsymbol{\Omega}$  describes resonance frequencies,  $\boldsymbol{\Gamma}_A$  corresponds to partial decay rates due to absorption and  $\boldsymbol{\Gamma}_R$  corresponds to partial decay rates due to radiation. Thus, the resonance frequencies for the open system are no longer real due to the decay contribution. The resonance modes are excited by the incoming waves  $s_+$  with the coupling strength  $\mathbf{K}_+$ . The resonance modes couple to the outgoing waves from the system  $s_-$  with  $\mathbf{K}_-$ . In addition to the indirect resonant pathways for scattering, the radiation can propagate directly between the ports that is described by matrix  $\mathbf{C}$ .

Owing to the presence of non-resonant pathway, Fano interference becomes possible resulting from the interference of resonance with back-scattering. In general, the set of equations 4.2-4.3 describes behavior of various MSs including single and multilayer configurations.

Considering the overall system including both the resonances and ports in the absence of additional losses, one can conclude that the system is energy conservative. Therefore, the radiation decay  $\boldsymbol{\Gamma}_R$  results from coupling of resonance to the ports. In addition to energy conservation, using reciprocity and time-reversal symmetry considerations, the rigorous constraints on the parameters  $\boldsymbol{\Gamma}_R$ ,  $\mathbf{K}_+$ ,  $\mathbf{K}_-$  and  $\mathbf{C}$  can be derived, as was demonstrated by Suh [Suh 2004]:

$$\mathbf{K}_- = \mathbf{K}_+ = \mathbf{K} \quad (4.44)$$

$$\boldsymbol{\Gamma}_R = \frac{1}{2} \mathbf{K}^\dagger \mathbf{K} \quad (4.55)$$

$$\mathbf{C} \mathbf{K}^* = -\mathbf{K} \quad (4.6)$$

where  $\mathbf{K}^\dagger$  and  $\mathbf{K}^*$  is the Hermitian transpose and complex conjugate of matrix  $\mathbf{K}$ , respectively. As follows from the equation 4.4, the coupling with incoming and outgoing waves is equal. The expression in Eq. 4.5 is the consequence of energy conservation. For example, in the absence of incoming waves the decay of resonance amplitude transfer entirely to the outgoing waves. Eq. 4.6 indicates that coupling constant is not arbitrary and is defined by direct propagation process.

For such general system the expression of the effective Hamiltonian can be introduced as [Dittes 2000]:

$$\mathbf{H}_{\text{eff}} = \boldsymbol{\Omega} + j\boldsymbol{\Gamma}_A + j\boldsymbol{\Gamma}_R \quad (4.7)$$

Since the system is open, the effective Hamiltonian is non-Hermitian resulting in complex energies. The eigenvalues of effective Hamiltonian at the same time represent poles of scattering

matrix  $\mathbf{S}$ . In the frequency domain, the scattering matrix that relates incoming and outgoing waves is given by [Lepetit 2010]:

$$\mathbf{S} = \mathbf{C} \left( \mathbf{I} + j\mathbf{K}^* [\omega\mathbf{I} - \mathbf{H}_{\text{eff}}]^{-1} \mathbf{K}^T \right) \quad (4.88)$$

Here  $\mathbf{C}$  is background scattering, i.e. non-resonant propagation,  $\mathbf{K}$  denotes coupling to external radiation. The above expression can be further expanded by using the eigenvalues and eigenvectors of the effective Hamiltonian:

$$\mathbf{S} = \mathbf{C} \left( \mathbf{I} + j \sum_k \frac{\mathbf{K}^* \mathbf{x}_k^R \mathbf{x}_k^L \mathbf{K}^T}{\omega - \omega_k} \right) \quad (4.9)$$

Here,  $\omega_k$  are the eigenvalues and  $\mathbf{x}_k^{R,L}$  the right/left eigenvectors of the effective Hamiltonian. Since it is non-Hermitian, eigenvalues are not real but possess an imaginary part to account for decay. In a given frequency range, the scattering matrix behavior is essentially governed by a finite number of poles.

## 4.2. Resonance coupling

In the previous section the general open system has been described. The transport process in such system results in Fano resonance due to the existence of two propagating pathways: direct non-resonant and indirect through the resonance coupling. However, more often systems possess several resonances which can additionally couple to each other if they coexist in a frequency range on the order of their linewidth [Lepetit 2010]. Let us briefly consider three main cases, where for simplicity we are limited by two coupling modes.

### 4.2.1. Coupling between modes in individual resonator

It is assumed that two modes corresponding to individual resonator are present in the single layer MS. These modes possess close resonance frequencies and can couple to each other. According to Eq. 4.7, the equation of effective Hamiltonian for such system can be written as:

$$\mathbf{H}_{\text{eff}} = \mathbf{\Omega} + j\mathbf{\Gamma}_A + j\mathbf{\Gamma}_R \quad (4.10)$$

where corresponding matrices of  $\mathbf{\Omega}$  and  $\mathbf{\Gamma}_R$  are:

$$\mathbf{\Omega} = \begin{pmatrix} \omega_1 & 0 \\ 0 & \omega_2 \end{pmatrix} \quad (4.11)$$

## 4.2 Resonance coupling

$$\mathbf{\Gamma}_R = \begin{pmatrix} \gamma_1 & \gamma_0 \\ \gamma_0 & \gamma_2 \end{pmatrix} \quad (4.12)$$

$$\mathbf{\Gamma}_A = \gamma_s \mathbf{I} \quad (4.13)$$

$\omega_{i,2}$  is the resonance frequency of each resonance.  $\gamma_s$  is the partial decay rate due to absorption. The diagonal terms  $\gamma_1$  and  $\gamma_2$  of matrix  $\mathbf{\Gamma}_R$  in eq. 4.12 are the partial decay rates due to radiation towards port 1 and 2 and the off-diagonal term  $\gamma_0$  corresponds to the coupling between resonance modes.

To write the scattering matrix for this case according to eq. 4.8, the coupling constants  $\mathbf{C}$  and  $\mathbf{K}$  are necessary to be defined. Defining matrix  $\mathbf{C}$ , we neglect non-resonant losses. Hence  $\mathbf{C}$  must be a unitary matrix:

$$\mathbf{C}\mathbf{C}^\dagger = \mathbf{I} \quad (4.14)$$

where  $\mathbf{C}^\dagger$  is Hermitian transpose of matrix  $\mathbf{C}$ . Hence the scattering matrix of non-resonant process in the symmetric system is also symmetric, i.e. phase quadrature then holds, generally we have:

$$\mathbf{C} = e^{j\varphi} \begin{pmatrix} r & jt \\ jt & r \end{pmatrix} \quad (4.15)$$

Here,  $r$  and  $t$  describe non-resonant, real reflection and transmission coefficients ( $r^2 + t^2 = 1$ ).  $\varphi$  is the phase between port 1 and 2, that in the case of single resonator is zero.

To determine matrix  $\mathbf{K}$  from the eq. 4.4-4.6, we have:

$$\mathbf{K} = \begin{pmatrix} \sqrt{\gamma_1} e^{j\theta_{11}} & \sqrt{\gamma_2} e^{j\theta_{12}} \\ \sqrt{\gamma_1} e^{j\theta_{21}} & \sqrt{\gamma_2} e^{j\theta_{22}} \end{pmatrix} \quad (4.16)$$

$$e^{j(\theta_{12}-\theta_{11})} + e^{j(\theta_{22}-\theta_{21})} = \frac{2\gamma_0}{\sqrt{\gamma_1\gamma_2}} \quad (4.17)$$

where  $\theta_{ij}$  is corresponding phase of  $i$ -resonance at  $j$ -port.

Since the system is symmetric with respect to mirror plane perpendicular to the radiation propagation between the ports, the resonance modes can propagate to the ports symmetrically or anti-symmetrically. Thus, we obtain:

$$e^{j(\theta_{12}-\theta_{11})} = \pm e^{j(\theta_{22}-\theta_{21})} \quad (4.18)$$

If symmetry of two resonances is distinct (even-odd modes), it follows from the eq. 4.17 that  $\gamma_0 = 0$ , i.e. the resonances separately couple to the continuum without coupling to each other. If the resonant modes have the same symmetry, they can couple through the radiation with coupling constant  $\gamma_0 = \pm\sqrt{\gamma_1\gamma_2}$ .

Let us consider the case when the resonance frequencies are equal, i.e.  $\omega_1 = \omega_2 = \omega_0$ . Then, diagonalization of matrix  $\mathbf{H}_{eff}$  gives rise to final expression for eigenmodes of effective Hamiltonian, as it has been shown in [Lepetit 2010]:

$$\begin{aligned} E_1 &= \omega_0 + j(\gamma_1 + \gamma_2 + \gamma_s) \\ E_2 &= \omega_0 + \gamma_s \end{aligned} \quad (4.19)$$

The imaginary part of eigenmodes  $E_2$  is determined by only absorption and is not related to the radiation losses, i.e. this mode is dark. Thus, owing to the coupling between two modes in the system, an extremely sharp resonance can be obtained.

#### 4.2.2. Near-field coupling between modes of different resonators

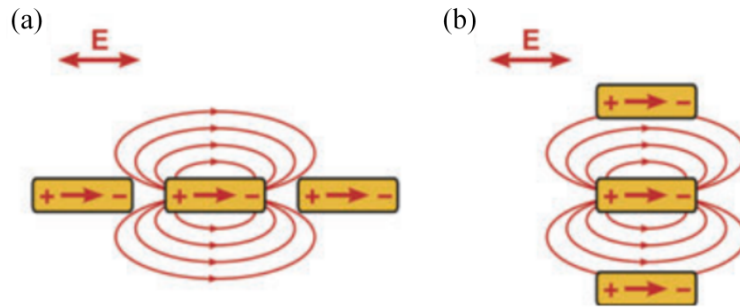
In MSs consisting of arrangement of sub-wavelength particles, resonance coupling most often occurs between modes of distinct resonators. Systems with different resonators coupled through the near-field are commonly used to achieve electromagnetically induced transparency (EIT) [Luk'yanchuk 2010]. The degree of interaction essentially depends on the separation distance between resonant elements and their arrangement [Ameling 2010; Luk'yanchuk 2010]. Among the diversity of possible structures, the configuration of vertically stacked elements along the direction of incident field results in stronger coupling for two reasons. Firstly, phase difference between the excitation of the elements breaks spatial forward-backward symmetry that allows to excite antisymmetric hybridized mode even in the case of identical resonators (Fig. 4.2).



Fig. 4.2. Asymmetric mode with excited opposite currents.

Secondly, contrary to the planar arrangement, the radiation field from dipole type elements arranged along the direction of the electric field is directed toward the other dipoles leading to

enhanced coupling effect as shown in Fig. 4.3 [Taubert 2011; Ameling 2010]. For this reason, we will limit our reasoning by considering the situation of two stacked elements.



**Fig. 4.3. Near-field coupling of resonators in MS. (a) planar arrangement along E-field. (b) Arrangement of elements perpendicular to the direction of E-field [Ameling 2010].**

For simplicity, let us consider the case of identical resonators. The schematic model of such system is presented in Fig. 4.4 where each element couples to the ports through the radiation and in the same time interacts with the other resonator through the near-field.

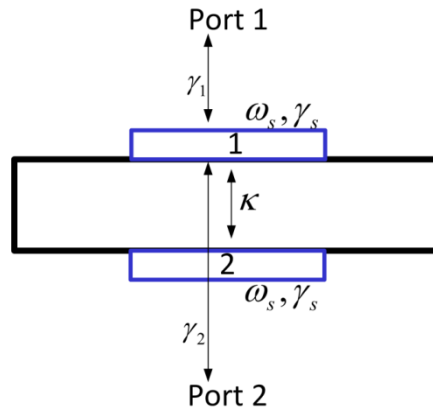


**Fig. 4.4. Schematic model of two identical coupled resonators.  $\omega_s$  is resonance frequency,  $\gamma_s$  is decay due to absorption,  $\gamma_1, \gamma_2$ , correspond to partial radiative decay towards port 1 and 2 respectively,  $\kappa$  is near-field coupling constant.**

Writing the effective Hamiltonian and the scattering matrix for such system according to eq. 4.7 and 4.8, it is necessary to define constituent terms. Since the resonators are identical, the matrix  $\mathbf{\Omega}$ , which defines resonance frequencies in the absence of external coupling to the ports, is symmetrical:

$$\mathbf{\Omega} = \begin{pmatrix} \omega_0 & \kappa \\ \kappa & \omega_0 \end{pmatrix} \quad (4.20)$$

where  $\omega_0$  is the resonance frequency of a single and uncoupled resonator,  $\kappa$  is the near-field coupling coefficient between both resonators.

Since the system is symmetric with respect to the mirror plane the coupling constant  $\mathbf{K}$  describing coupling to the ports is given by:

$$\mathbf{K} = \begin{pmatrix} \sqrt{\gamma_1} e^{j\theta_1} & \sqrt{\gamma_2} e^{j\theta_2} \\ \sqrt{\gamma_2} e^{j\theta_2} & \sqrt{\gamma_1} e^{j\theta_1} \end{pmatrix} \quad (4.21)$$

$\gamma_1$  and  $\gamma_2$  are the partial damping rates towards port 1 and 2, respectively.  $\theta_1$  and  $\theta_2$  are their corresponding phases. Applying the constraints to the matrices  $\mathbf{K}$  and  $\mathbf{\Gamma}_R$  from eq. 4.4-4.6, we have:

$$\mathbf{\Gamma}_R = \frac{1}{2} \begin{pmatrix} \gamma_1 + \gamma_2 & 2\sqrt{\gamma_1\gamma_2} \cos(\theta_1 - \theta_2) \\ 2\sqrt{\gamma_1\gamma_2} \cos(\theta_1 - \theta_2) & \gamma_1 + \gamma_2 \end{pmatrix} \quad (4.22)$$

$$\mathbf{\Gamma}_A = \gamma_s \mathbf{I} \quad (4.23)$$

Similarly to the case of single resonator in eq. 4.15, the background scattering for the evanescent coupled resonators is written as:

$$\mathbf{C} = \begin{pmatrix} r & jt \\ jt & r \end{pmatrix} \quad (4.24)$$

The final expression for the effective Hamiltonian is:

$$\mathbf{H}_{\text{eff}} = \begin{pmatrix} \omega_0 & \kappa \\ \kappa & \omega_0 \end{pmatrix} + \frac{1}{2} j \begin{pmatrix} \gamma_1 + \gamma_2 & 2\sqrt{\gamma_1\gamma_2} \cos(\theta_1 - \theta_2) \\ 2\sqrt{\gamma_1\gamma_2} \cos(\theta_1 - \theta_2) & \gamma_1 + \gamma_2 \end{pmatrix} \quad (4.25)$$

The eigenvalues of the effective Hamiltonian can be found by solving the characteristic polynomial:

$$\text{Re}(\omega_{\pm}) = \omega_0 \pm \kappa \quad (4.26)$$

$$\text{Im}(\omega_{\pm}) = \gamma_s + \frac{\gamma_1 + \gamma_2}{2} \pm \sqrt{\gamma_1\gamma_2} \cos(\theta_1 - \theta_2) \quad (4.27)$$

## 4.2 Resonance coupling

The eigenmodes can be classified as either even or odd (symmetric or antisymmetric). As it can be seen from eq. 4.26, the symmetric mode  $\omega_+$  has the highest resonance frequency, while the antisymmetric mode  $\omega_-$  mode has the lowest one.

In turn, the quality factor of each resonance is given by:

$$Q_{\pm} = \frac{\omega_s \pm \kappa}{2\gamma_s + \gamma_1 + \gamma_2 \pm 2\sqrt{\gamma_1\gamma_2} \cos(\theta_1 - \theta_2)} \quad (4.28)$$

In the limit of vanishing substrate thickness, partial decay rates due to radiation towards ports 1 and 2 tend towards each other.

$$\lim_{t \rightarrow 0} \gamma_1 = \lim_{t \rightarrow 0} \gamma_2 \rightarrow \gamma_0 \quad (4.29)$$

$$\lim_{t \rightarrow 0} \theta_1 = \lim_{t \rightarrow 0} \theta_2 \rightarrow \theta_0 \quad (4.30)$$

$$\lim_{t \rightarrow 0} \omega_{\pm} \rightarrow \omega_0 + j\gamma_s + j\gamma_0 \pm [\kappa + j\gamma_0] \quad (4.31)$$

This has interesting consequences for the Q-factor:

$$\lim_{t \rightarrow 0} Q_+ = \frac{\omega_s + \kappa}{2\gamma_s + 4\gamma_0} \quad (4.32)$$

$$\lim_{t \rightarrow 0} Q_- = \frac{\omega_s - \kappa}{2\gamma_s} \quad (4.33)$$

Now, we see that the Q-factor of the antisymmetric mode is not limited by radiation, *i.e.*, it is infinite in the limit of vanishing absorption. The important conclusion following from this analysis is that, for thin substrates, radiation losses are intrinsically lower for the antisymmetric mode  $\omega_-$  and it thus acts as a dark mode whereas the symmetric mode  $\omega_+$  acts as a bright mode.

### 4.2.3. Far-field coupling between modes of different resonators

In the system consisting of two stacked resonant particles the near-field coupling exponentially vanishes with increasing inter plane separation distance. However, when the distance becomes higher than the wavelength in the medium confined by two MSs, far-field interactions start to play a role, and the behavior of structure becomes similar to a Fabry-Perot cavity as shown in Fig. 4.5b. Plasmon resonances of each layer interacting via far-field lead to appearance of cavity modes with higher quality factor than for conventional plasmonic resonance allowing to improve sensing properties of MMs [Ameling 2010].

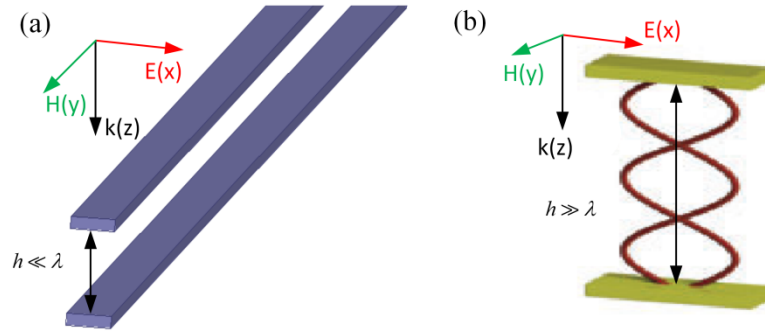


Fig. 4.5. MS cavity based on near-field coupling (a) and far-field coupling (b).

The effective Hamiltonian is similar to that of the evanescent coupled MSs (eq. 4.25) except for the influence of near-field coupling. We have:

$$\mathbf{H}_{\text{eff}} = \begin{pmatrix} \omega_0 & 0 \\ 0 & \omega_0 \end{pmatrix} + \frac{1}{2} j \begin{pmatrix} \gamma_1 + \gamma_2 & 2\sqrt{\gamma_1 \gamma_2} \cos(\theta_1 - \theta_2) \\ 2\sqrt{\gamma_1 \gamma_2} \cos(\theta_1 - \theta_2) & \gamma_1 + \gamma_2 \end{pmatrix} \quad (4.34)$$

Since the distance between resonators is large, the phase incursion of propagation from 1 element to the other becomes considerable, i.e. comparable to the wavelength of interest.

Therefore, eq. 4.15 for the non-resonant propagation is written as:

$$\mathbf{C} = \begin{pmatrix} r & jt \cos \varphi \\ jt \cos \varphi & r \end{pmatrix} \quad (4.35)$$

where  $\varphi = \omega n h / c$  is the phase incursion between stacked MSs,  $n$  and  $h$  is the refractive index and the thickness of dielectric spacer between MSs, respectively. Thus, the transmission coefficient is a periodic function and reaches maximum when  $\varphi$  is a multiple of  $\pi$ .

As it has been shown in the sections 4.2.1-4.2.3, narrow resonances appears as a result of coupling modes in an individual element as well as in the system of coupled resonators through near- and far-field. However, the configuration of two stacked MSs representing the MS cavity with deeply sub-wavelength spacing between MSs, presents several advantages. Firstly, while concerning operation in the optical domain it is difficult to fabricate with existing planar technologies closely located resonant elements and control their separation with few nanometers precision. In contrast, it is much easier to do this for the control of the dielectric film thickness separating two stacked elements. Secondly, the resonance frequency of anti-symmetric mode can be tuned through near-field coupling between resonant elements that makes such systems more flexible for sensing applications.

### 4.3. Metasurface cavity

In this section we consider MSs cavities in view of sensing applications and perform analysis of their operation in the near-field and far-field coupling regimes with particular emphasis on the engineering of radiation losses.

#### 4.3.1. Transmission and reflection characteristics

Using eq. 4.9, we can obtain an explicit expression of the scattering matrix. In our case, determination of  $\mathbf{x}_k^{R,L}$  is greatly facilitated by the fact that eigenmodes are either even or odd:

$$\mathbf{x}_{\pm}^R = (\mathbf{x}_{\pm}^L)^T = \frac{1}{\sqrt{2}} \begin{pmatrix} 1 \\ \pm 1 \end{pmatrix} \quad (4.36)$$

Therefore, the expression for scattering matrix is reduced to:

$$\mathbf{S} = \mathbf{C} \left( \mathbf{I} + j \left[ \frac{\mathbf{K}^* \mathbf{x}_k^R \mathbf{x}_k^L \mathbf{K}^T}{\omega - \omega_+} + \frac{\mathbf{K}^* \mathbf{x}_k^R \mathbf{x}_k^L \mathbf{K}^T}{\omega - \omega_-} \right] \right) \quad (4.37)$$

In the end, we obtain the following expressions for the reflection and transmission coefficients:

$$S_{11} = r + j \sum_{\pm} \frac{(r \pm jt)(\gamma_1 + \gamma_2 \pm 2\sqrt{\gamma_1 \gamma_2})}{\omega - \omega_{\pm}} \quad (4.38)$$

$$S_{21} = jt + j \sum_{\pm} \frac{(jt \pm r)(\gamma_1 + \gamma_2 \pm 2\sqrt{\gamma_1 \gamma_2})}{\omega - \omega_{\pm}} \quad (4.39)$$

These expressions are consistent with analysis results presented in section 4.2.2 revealing the fact that the odd mode is much less excited than the even mode. This is true for both reflection and transmission coefficients. In the limit of vanishing substrate thickness, when  $\gamma_1 = \gamma_2$ , the radiation decay is totally suppressed and odd mode becomes completely uncoupled resulting in infinite Q-factor.

#### 4.3.2. Engineering of radiation losses

As it has been shown in Chapter 3, the radiative damping rate increases with the resonant element size due to increase of induced electric dipole moment [Dahmen 2007; Wokaun 1982]. Thus, an elongated shape aspect ratio exhibits higher radiation losses. They can be decreased by designing geometry with constituent parts perpendicular to the polarization of incident electric field [Burokur 2015]. Such configuration allows reducing projection of induced dipole electric

moment and, consequently, results in decreased radiative losses. For instance, resonance bandwidth of Z-shaped resonator with legs perpendicular to the vertical E-field polarization is noticeably decreased as compared with two connected V-antennas (Figs. 3.3-3.4).

It is obvious from eq. 4.23 that for a finite substrate thickness the quality factors of symmetric and anti-symmetric modes depends on the decay rate of each individual element. Therefore, the decrease of each MS radiative losses leads to the narrowing of MS cavity resonance bandwidth. To demonstrate the validity of such strategy for radiative loss reduction we perform a comparative analysis of evanescently coupled cavities with three different type of MS resonant elements. We consider the evolution from the simplest dipole type resonant element such as cut wire to the square Z-shaped resonant element through the intermediate case of oblong Z-element (Fig. 4.6).

A uniform electromagnetic plane wave normally incident on the MSs is considered. Reflection and transmission coefficients are calculated numerically using a finite-element commercial code HFSS by ANSYS. The numerical simulations are performed according to the description in the Chapter 2.

Since Fano resonance is related to interference effect and strongly influenced by absorption losses, for experimental realization of MS cavity we use composite material ArlonAD450 with relative permittivity  $\epsilon_r = 4.5$  and small tangential losses  $\tan \delta = 0.0035$ . To facilitate the measurement of asymmetric sharp spectral characteristics of Fano resonance, the size of the resonant element and unit cell are adjusted in order to get the resonance frequency of anti-symmetric mode at about 10 GHz where the spectral analyzer is having highest sensitivity.

To investigate the impact of radiation losses, we consider for the presented simulation in Fig. 4.5, that absorption losses are negligibly small, i.e., the metal is assumed as a perfect conductor and the absorption of dielectric substrate is absent ( $\tan \delta = 0$ ). The thickness of the lossless dielectric substrate for all three cases is  $h = 0.5$  mm.

The unit cells are designed such that the filling factor corresponding to the ratio of occupied by their surface and the length of the resonant elements are identical for all three structures. The geometrical dimensions of considered three types of resonant elements and their respective unit cell are detailed in the caption of Fig. 4.5.

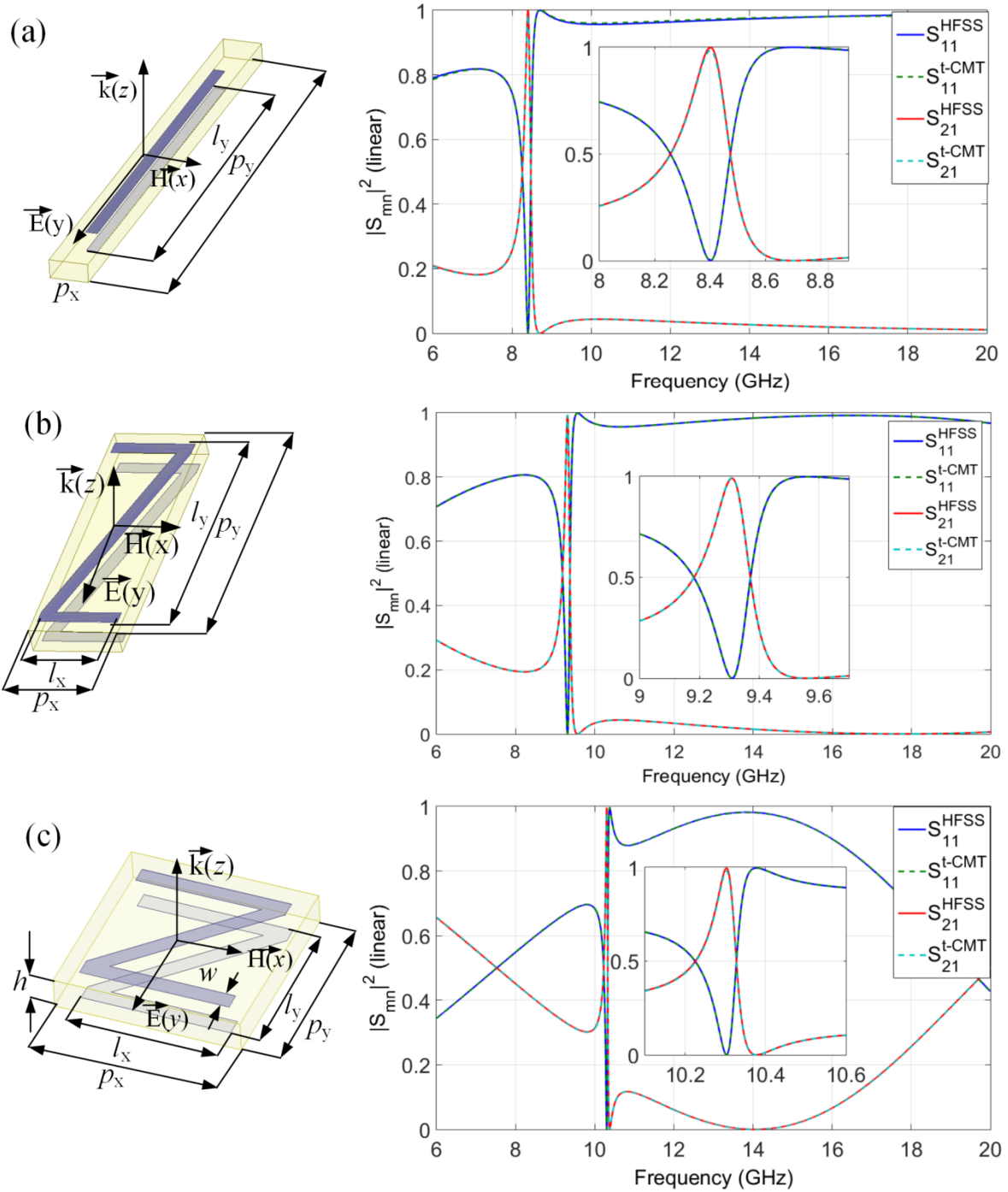


**Fig. 4.6.** Schematic of MS cavity resonant elements and computed reflection and transmission coefficients under normal incidence (HFSS– solid lines, CMT – dotted lines). (a) Array of superposed CW with dimensions,  $l_y = 9$  mm:  $p_y = 9.42$  mm,  $p_x = 1.3$  mm. (b) Array of superposed oblong Z-shaped resonators:  $p_y = 6.44$  mm,  $p_x = 1.9$  mm,  $l_y = 5.7$  mm,  $l_x = 1.8$  mm. (c) Array of superposed squared Z:  $l_x = l_y = 2.8$  mm,  $w = 0.3$  mm,  $p_x = p_y = 3.5$  mm.

Transmission and reflection spectra corresponding to all these structures displayed in Fig. 4.6, exhibit a sharp Fano resonance in the vicinity of anti-symmetric mode frequency and a wide

resonance corresponding to the symmetric mode. As it can be seen, the symmetric resonance is so broad that it goes far beyond the considered frequency range. The resonance frequency position of symmetric mode is higher than 20 GHz for pair of CWs and is at 18 GHz and 14 GHz for pair of oblong and square Z, respectively. The following neat tendency can be observed: the resonance becomes narrower when CW is progressively transformed into the square Z. The same tendency holds also for the anti-symmetric mode. The quality factor of this mode is  $Q_{CW} = 44$ ,  $Q_{Zr} = 55$ ,  $Q_{Zs} = 229$  for the CW, oblong and square Z MSs, respectively. Thus, spectra of the resonators show that the spectral width of both symmetric  $\omega_+$  and antisymmetric  $\omega_-$  modes is reduced when CW is transformed to squared Z. This result indicates that radiation losses are reduced when the size of the resonant element along the direction of the incident electric field is decreased.

The instantaneous current distribution for Z-MS cavity presented in Fig. 4.7 shows that anti-symmetric mode at 10.3 GHz is characterized by an opposite current flow in the pair of resonant elements forming, while symmetric mode at 14 GHz exhibits in-phase currents.

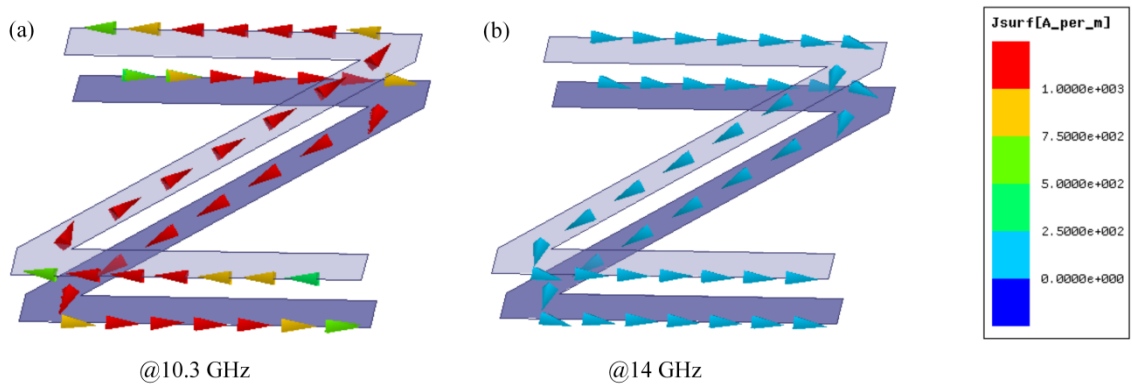


**Fig. 4.7. Current distribution of eigenmodes for squared Z. (a) Anti-symmetric mode. (b) Symmetric mode.**

### 4.3.3. CMT mode analysis

To better understand the underlying hybridization mechanism leading to symmetric and anti-symmetric modes, we fit full-wave simulation results with TCMT. Furthermore, to fit these modes independently we separate them via an even/odd analysis [Lin 2014]. As mentioned, a resonance mode in a symmetric system can interact with two ports in-phase or out-of-phase i.e. even and odd mode, respectively. Thus, even and odd modes can be expressed through transmission and reflection scattering parameters:

$$S_e = S_{11} + S_{21} \quad (4.40)$$

$$S_o = S_{11} - S_{21} \quad (4.41)$$

Therefore, using equations 4.38 and 4.39 we have final expression for even/odd modes:

$$S_e = (r + jt) \left[ 1 + j2 \frac{(\gamma_1 + \gamma_2 + 2\sqrt{\gamma_1\gamma_2})}{\omega - \omega_+} \right] \quad (4.42)$$

$$S_o = (r - jt) \left[ 1 + j2 \frac{(\gamma_1 + \gamma_2 - 2\sqrt{\gamma_1\gamma_2})}{\omega - \omega_-} \right] \quad (4.43)$$

Here,  $S_e$  and  $S_o$  are respectively the even and odd scattering parameters. In practice, the parameters  $S_e$  and  $S_o$  can be computed directly with a 1-port simulation terminated by a PMC/PEC boundary bisecting the geometry with the mirror plane normal to the propagation direction (Fig. 4.8). Since there is no phase shift for magnetic boundary, it serves to compute even mode, while odd mode is calculated by using electric boundary conditions. To confirm, that the considered symmetric and anti-symmetric modes are indeed even and odd, both 2-ports and 1-port simulations have been done. The results demonstrated in Fig. 4.9 show an excellent agreement between scattering parameters  $S_{11}$  and  $S_{21}$  obtained from 2-ports simulations and calculated from relations 4.40-4.41 by using  $S_e$  and  $S_o$  extracted from 1-port simulation.

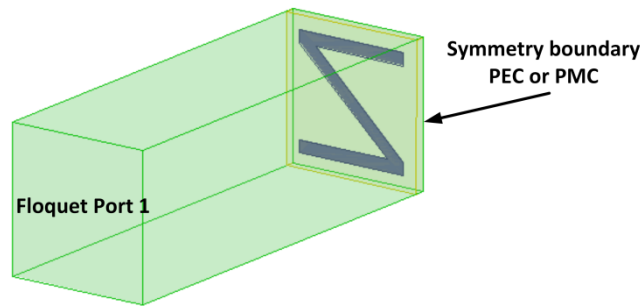


**Fig. 4.8.** 1-port simulations with symmetry boundary for either perfect electric or perfect magnetic conductivity.

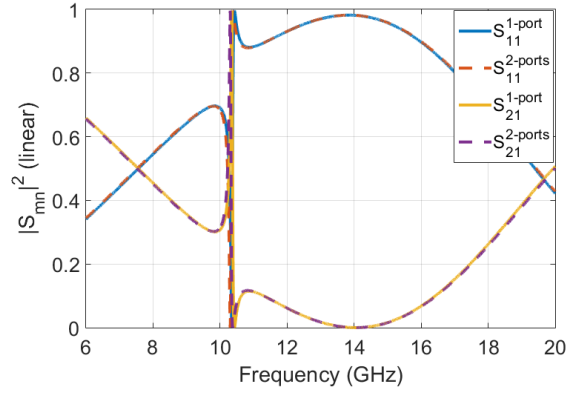


**Fig. 4.9. Transmission and reflection scattering parameters for square  $Z$  MS-cavity calculated with 1- and 2-ports simulations.**

Reflection and transmission coefficients  $r$  and  $t$  are non-resonant contributions to the scattering matrix. However, the distinction between resonant and non-resonant contributions is only meaningful with respect to a frequency range of interest (FRI). All modes inside of FRI are considered individually while all modes outside of the FRI are lumped together into  $C$ :

$$C_e = (r + jt) = \sum_{\omega_{e,k} \notin \text{FRI}} \frac{r_{e,k}}{\omega - \omega_{e,k}} \quad (4.44)$$

$$C_o = (r - jt) = \sum_{\omega_{o,k} \notin \text{FRI}} \frac{r_{o,k}}{\omega - \omega_{o,k}} \quad (4.45)$$

Thus,  $r$  and  $t$  are only weakly frequency-dependent. In practice, we rely on Vector Fitting to obtain a partial fractions expansion of the even/odd scattering parameters [Sautter 2015]. Vector Fitting is a robust numerical method to provide rational approximation in the frequency domain using poles and residues. In this study we use rational function fit algorithm of Matlab to fit simulated HFSS data. It is clearly seen from the Fig. 4.10a, that two resonances manifest separately in even/odd spectra. The fitting results for scattering parameters and background radiation are presented in Fig. 4.10b.

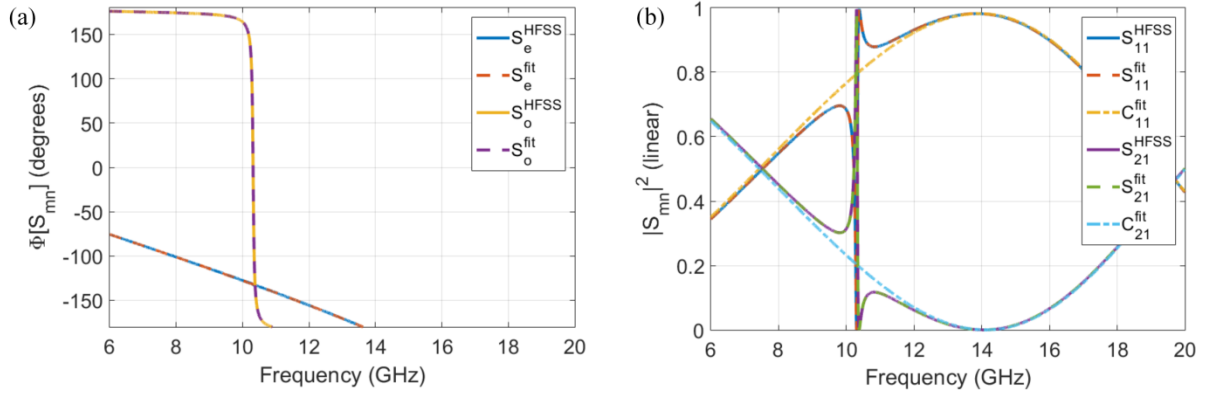


**Fig. 4.10.** Computed scattering parameters for bi-layered squared Z MS. (a) Phase dependency for even/odd modes (solid line - HFSS, dotted line - TCMT). (b) Reflection and transmission (solid line - HFSS, dotted line - TCMT) and fitted background radiation  $C_{11}$  and  $C_{21}$ .

The TCMT modeling results are in excellent agreement with those obtained by numerical HFSS simulations for all considered MS cavities as displayed in Fig. 4.6. They also confirm the fact that transforming the resonant element geometry from CWs to Z leads to a strong decrease of resonant element radiation losses.

#### 4.3.4. Non-radiative losses

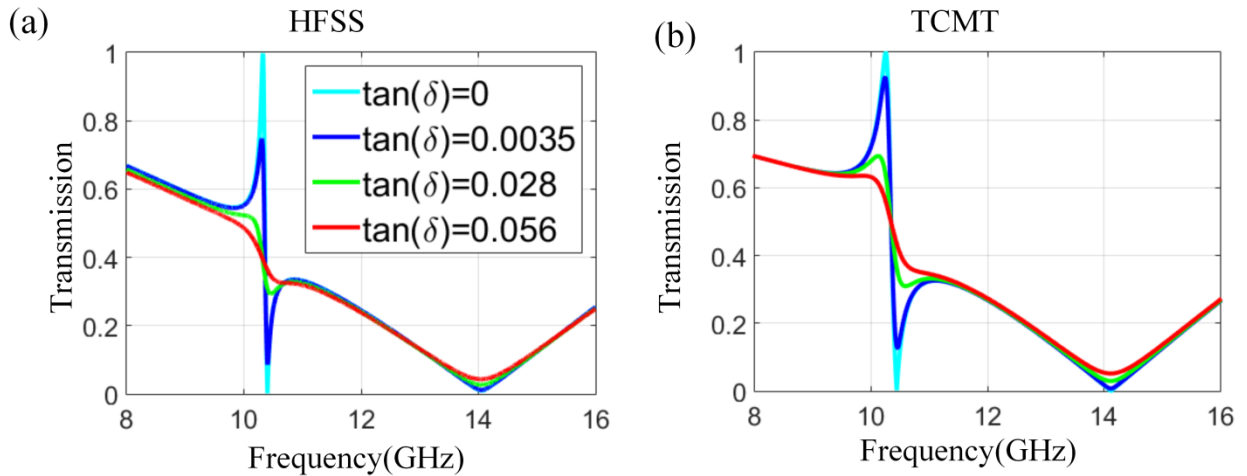


**Fig. 4.11.** Transmission magnitude for different absorption losses in dielectric substrate corresponding to the value of tangential loss. (a) Full-wave simulation. (b) Analytical model based on TCMT.

Apart from radiation losses, practical structures can be subjected to residual absorption losses that are present even for MMs operating in the microwave domain. Since metal is assumed

perfect for the microwave, absorption is related only to dielectric losses. To evaluate the importance of these residual dielectric losses we consider more realistic examples of MS cavity.

Transmission and reflection spectra calculated by both HFSS and TCMT models and corresponding to the square Z MSs cavity with different level of  $\tan\delta$  for 0.5 mm thickness of dielectric substrate are shown in Fig. 4.11. As it can be observed, the contrast and the sharpness of the Fano resonance are strongly affected by the presence of absorption losses. The increase of absorption losses leads to practically vanishing resonance. Nevertheless, for the realistic case of  $\tan\delta = 0.0035$  of the ArlonAD450 substrate, Fano resonant feature is still well pronounced.

#### 4.3.5. Experimental results

To validate modeling results, a prototype of the Z-MSs cavity has been fabricated using classical printed circuit board technology. The geometrical dimensions of Z design and unit cell are the same as for numerical calculation described previously. The sample consists of  $56 \times 56$  cells on a  $210 \text{ mm} \times 210 \text{ mm}$  dielectric substrate. The dielectric substrate is ArlonAD450 with relative permittivity  $\epsilon_r = 4.5$  and  $\tan\delta = 0.0035$ . Microwave transmission measurements based on the experimental setup described in Chapter 2 have been done for an electromagnetic wave normally incident on Z-MS cavity.

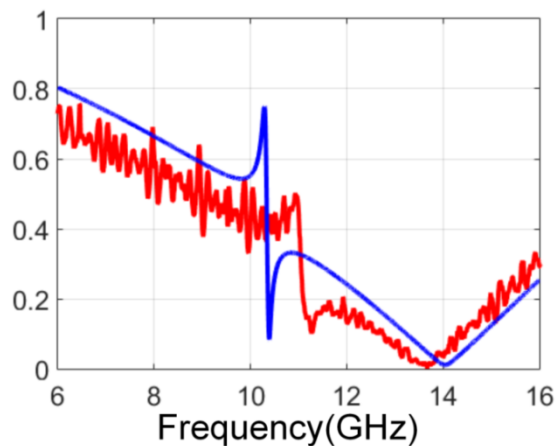


**Fig. 4.12. Measured (red curve) and HFSS-simulated (blue curve) transmission spectra under normal incidence for bi-layered Z MSs with  $\tan\delta = 0.0035$ .**

Measured transmission spectrum exhibit a marked Fano resonance with steep intensity variation shown in Fig. 4.12. There is a good qualitative agreement between measurements and simulation results. The presence of noisy features can be due to the Fabry-Perot interferences occurring for normal incidence when the antenna emission element and MSs are forming a parallel plates

resonant cavity. Also, the slight shift between experimental and modeling results for the resonance frequencies can be due to the deviations of the geometry of fabricated MS with respect to the nominal one and also to the permittivity tolerance of the dielectric substrate.

#### 4.4. Sensing capability

The final goal of our study is the demonstration of the enhanced sensitivity of deeply sub-wavelength thickness cavity formed by two evanescently coupled MSs with respect to the far-field coupled Fabry-Perot cavity. To this end, we calculate numerically the sensitivity  $S$  as the intensity variation  $\Delta I$  for a given intra-cavity index variation  $\Delta n$  defined by Ameling (Fig. 4.13) [Ameling 2010]:

$$S = \partial I / \partial n \quad (4.46)$$

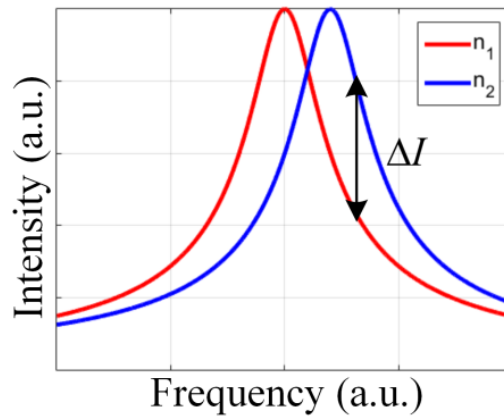


**Fig. 4.13. Definition of sensitivity as intensity variation  $\Delta I$  induced by index variation  $\Delta n$  at plasmon resonance frequency.**

The calculations are performed by using the TCMT model [Suh 2005] by taking also into account the variation of the localized surface plasmon (LSP) resonance frequency caused by intra-cavity index variation. The resonance contribution is determined by means of HFSS numerical modeling for single Z metasurface with identical permittivity  $\varepsilon = 4.5$  lossless dielectric substrate. The resulting transmitted intensity and sensitivity as function of frequency and cavity thickness variation are displayed in Fig. 4.14. Three characteristic regions can be differentiated. For small cavity thickness  $h < 1$  mm ( $h \ll \lambda_0 n$ , where  $\lambda_0 = 11.7$  mm is the resonance wavelength for uncoupled MSs resonant element) the spectral response exhibits sharp Fano resonance and broad symmetric mode as it has been discussed above in section 4.2. The sensitivity is reaching very high values, up to  $10^5$  (50 dB on a log scale) at the Fano resonance

frequency of 8.3 GHz. For intermediary cavity thickness  $1 \text{ mm} < h < 10 \text{ mm}$  ( $h \sim \lambda_0$ ) the spectra does not present any narrow resonance features and sensitivity are relatively low over the whole frequency region. It is evident that operation in this region is not suited for sensing applications. For large cavity thickness ( $h > 10 \text{ mm}$ ) far-field interaction between MSs leads to Fabry-Perot cavity modes. The dependence of the transmitted intensity and sensitivity for certain frequency is not monotonous with cavity thickness. Extremely sharp peaks in transmission occur only when the frequency of a Fabry-Perot cavity mode coincides with plasmon resonance of single MS, i.e. close to 11.7 GHz.

At these points of cavity mode excitation the sensitivity is very high. The sensitivity dependence on refractive index variation can be explained by the reasoning performed in section 3.2. For the small cavity ( $h \ll \lambda_0 n$ ) besides the contribution of LSP resonance, the strong sensitivity is related to the near-field coupling  $\kappa \sim e^{-jn}$ , where  $h$  is a distance between MSs and  $n$  is refractive index of dielectric spacer. For the large cavity ( $h > \lambda_0 n$ ) near field coupling becomes zero. However, the phase incursion  $\varphi = \omega h n / c$  starts to play a role that is also dependent on refractive index.

Furthermore, the sensitivity of the Fabry-Perot cavity doesn't overwhelm that of sub-wavelength thickness Fano resonance cavity. It is evident, that introducing even small absorption losses in dielectric medium will significantly influence on the resonances due to the large volume of Fabry-Perot MSs cavity. As evidence, the results of HFSS simulation of cavity system formed by two squared Z MSs with separation distance of  $h = 51.2 \text{ mm}$  is shown in Fig. 4.15. In contrast to the similar analysis performed for near-field coupling in section 4.3.4, where Fano resonance is well pronounced for the realistic case of  $\tan\delta = 0.0035$ , Fabry-Perot cavity modes almost vanish.

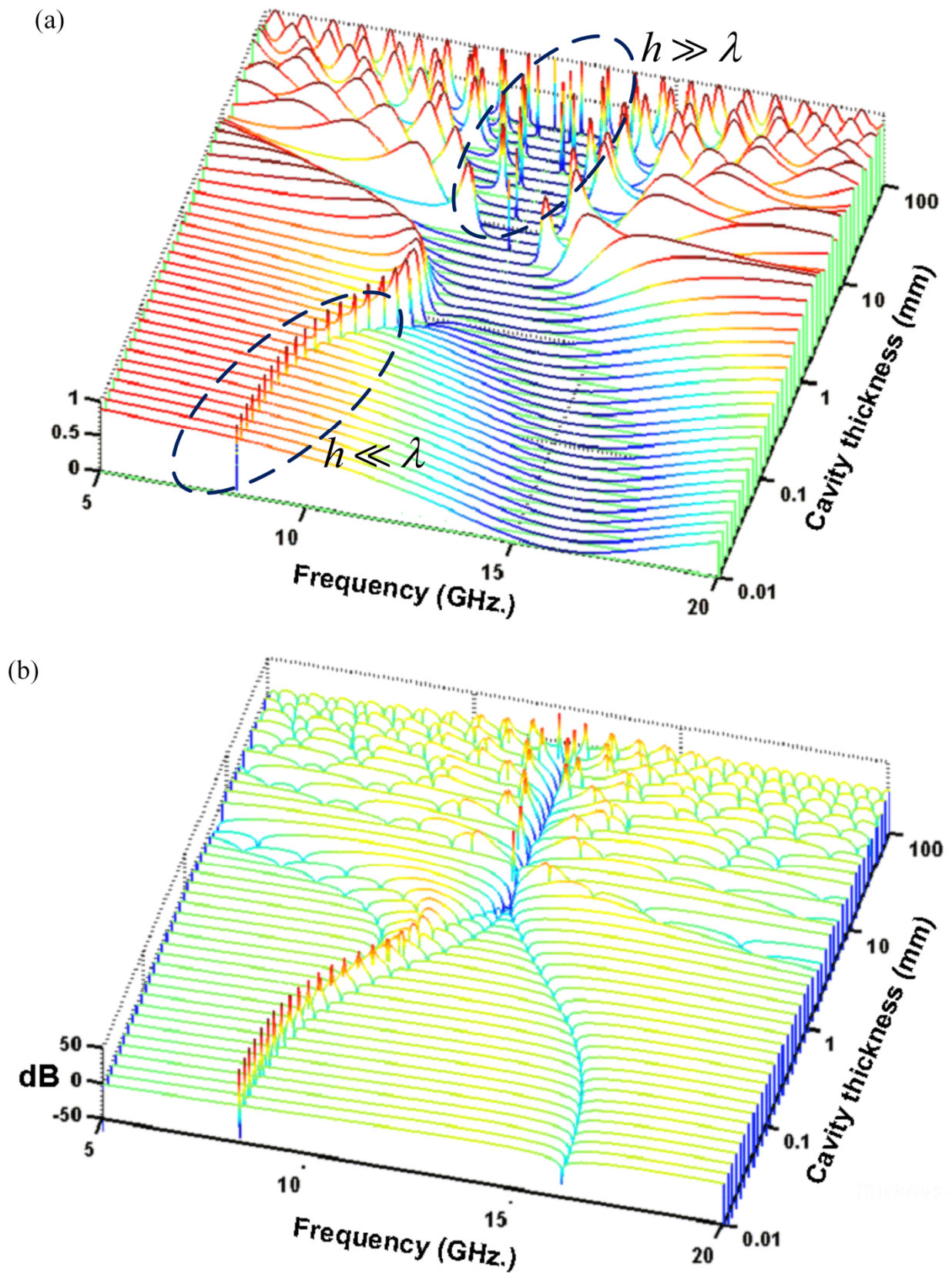
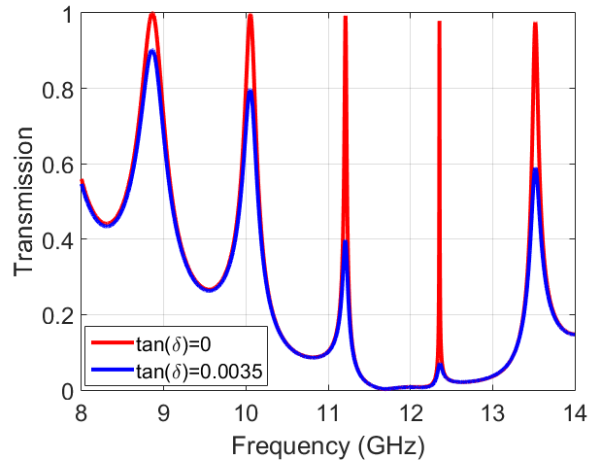


Fig. 4.14. CMT numerical results: a) Transmitted intensity (linear scale); b) Intra-cavity refractive index variation sensitivity (dB scale).



**Fig. 4.15. Transmission magnitude for Fabry-Perot cavity formed by two squared Z MSs for lossless and lossy dielectric spacer.**

#### 4.5. Conclusion

In this Chapter the theoretical analysis of Fano resonance in MSs cavity system is performed by using TCMT accounting for the open character of MSs systems. The existence of two propagation pathways either through indirect resonance coupling or direct free-space propagation leads to Fano resonance excitation. The TCMT modeling has shown that Fano resonance appears at the vicinity of high quality factor anti-symmetric or odd mode. Furthermore, it has been confirmed that radiation losses can be reduced by using Z-shaped resonant element for MS-cavity that noticeably increases resonance quality factor. The proposed method of evanescently coupled MSs is promising for the sensing applications.

## References

- [Ameling 2010] R. Ameling et al., 2010. “Cavity-enhanced localized plasmon resonance sensing”. *Applied Physics Letters*, 97, p.253116.
- [Burokur 2015] S.N. Burokur, A. Lupu & A. Lustrac, 2015. “Direct dark mode excitation by symmetry matching of a single-particle-based metasurface”. *Physical Review B*, 91.
- [Dahmen 2007] C. Dahmen, B. Schmidt & G. Plessen, 2007. “Radiation Damping in Metal Nanoparticle Pairs”. *Nano Letters*, 7, pp.318-322.
- [Dittes 2000] F. Dittes, 2000. “The decay of quantum systems with a small number of open channels”. *Physics Reports*, 339, pp.215-316.
- [Fan 2003] S. Fan, W. Suh & J.D. Joannopoulos, 2003. “Temporal coupled-mode theory for the Fano resonance in optical resonators”. *Journal of the Optical Society of America A*, 20, p.569.
- [Haus 1984] H.A. Haus, 1984. *Waves and Fields in Optoelectronics* (Prentice-Hall series in solid state physical electronics).
- [Lepetit 2010] T. Lepetit, E. Akmansoy, J.-P. Ganne & J.-M. Lourtioz, 2010. “Resonance continuum coupling in high-permittivity dielectric metamaterials”. *Physical Review B*, 82.
- [Lin 2014] D. Lin, P. Fan, E. Hasman & M.L. Brongersma, 2014. “Dielectric gradient metasurface optical elements”. *Science*, 345, pp.298-302.
- [Luk'yanchuk 2010] B. Luk'yanchuk et al., 2010. “The Fano resonance in plasmonic nanostructures and metamaterials”. *Nature Materials*, 9, pp.707-715.

- [Sautter 2015] J. Sautter et al., 2015. “Active Tuning of All-Dielectric Metasurfaces”. ACS Nano, 9, pp.4308-4315.
- [Suh 2005] W. Suh, O. Solgaard & S. Fan, 2005. “Displacement sensing using evanescent tunneling between guided resonances in photonic crystal slabs”. Journal of Applied Physics, 98, p.033102.
- [Suh 2004] W. Suh, Z. Wang & S. Fan, 2004. “Temporal coupled-mode theory and the presence of non-orthogonal modes in lossless multimode cavities”. IEEE Journal of Quantum Electronics, 40, pp.1511-1518.
- [Taubert 2011] R. Taubert et al., 2011. “From Near-Field to Far-Field Coupling in the Third Dimension: Retarded Interaction of Particle Plasmons”. Nano Letters, 11, pp.4421-4424.
- [Wokaun 1982] A. Wokaun, J.P. Gordon & P.F. Liao, 1982. “Radiation Damping in Surface-Enhanced Raman Scattering”. Physical Review Letters, 48, pp.957-960.

## Chapter 5.

### Control of Fano Resonance in Metasurfaces

In this chapter we consider enantiomeric structure where one element is rotated with respect to other in contrast to symmetric system presented in previous chapter. Commonly, structures with broken mirror symmetry with respect to propagation direction is used for optical activity applications [Alpeggiani 2017; Maslovski 2009; Parappurath 2017]. However here, we will analyze resonance behavior of enantiomeric configuration in order to obtain sharp spectral characteristics.

#### 5.1. Control of Fano resonance in enantiomeric metasurface

We perform a study to control the quality factor of Fano resonance by using enantiomeric MS composed of identical Z-shaped resonators disposed on the two sides of the dielectric substrate. Let us start with a system of two coupled non-overlapping enantiomeric Z as shown in Fig. 5.1. For the sample, the unit cell period along  $x$ -axis and  $y$ -axis is  $p_x = p_y = 6$  mm, the dimensions are  $l_y = 5.8$  mm,  $l_x = 2.85$  mm and the width of metallic wire is  $w = 0.3$  mm. The dielectric substrate used for the series of enantiomeric designs has relative permittivity  $\epsilon_r = 2.2$  and tangential loss  $\tan\delta = 0.0009$ . The simulated spectral characteristics of the latter metasurface under normal plane wave incidence with electric field oriented along  $x$ - and  $y$ -axes are shown in Figs. 5.2a and b, respectively.

Calculated coefficients of reflection  $r$  and transmission  $t$  spectra of bi-layered Z structure illuminated by a normally incident electromagnetic wave are shown in Fig. 5.2. With electric field polarized along  $y$ -axis (Fig. 5.2a) the spectrum exhibits wide Lorentz resonance at 10 GHz, while for orthogonal polarization (Fig. 5.2b) a marked Fano resonance with a reflection maximum at  $f_0 = 10.9$  GHz and minimum at  $f_1 = 13.9$  GHz is visible in the spectral response. The excited Fano resonance exhibits wide asymmetric line, *i.e.* strongly radiates to the free-space. Since the geometry is not trivial let us analyze the observed Fano resonance in more details.

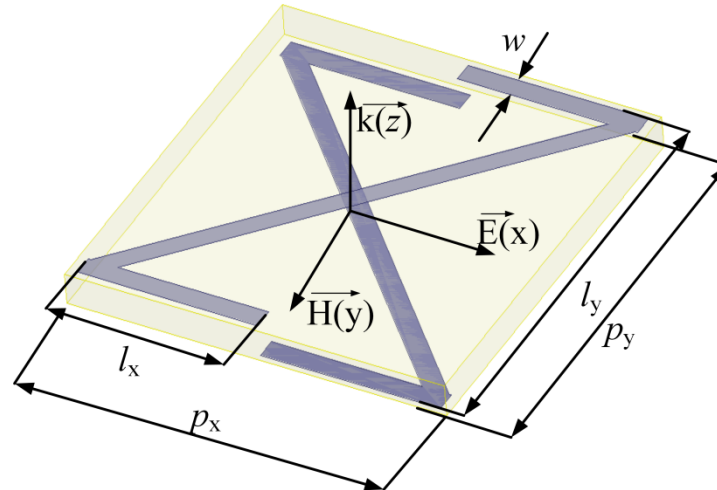


Fig. 5.1. Schematic of unit cell for enantiomeric Z-shaped Ms.

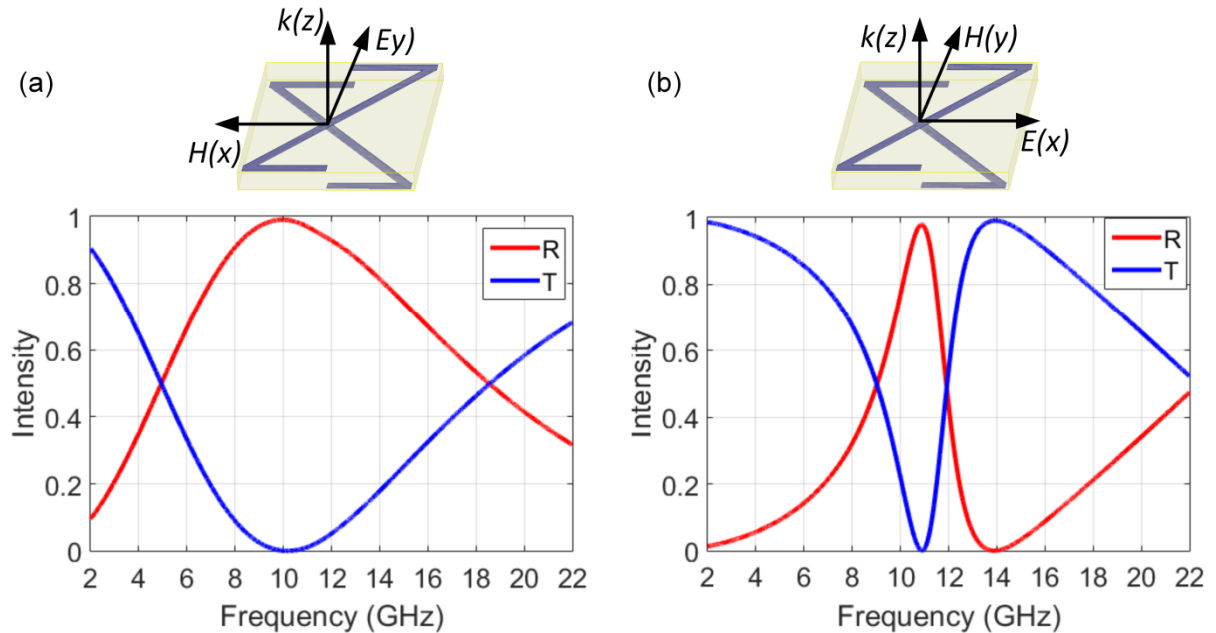
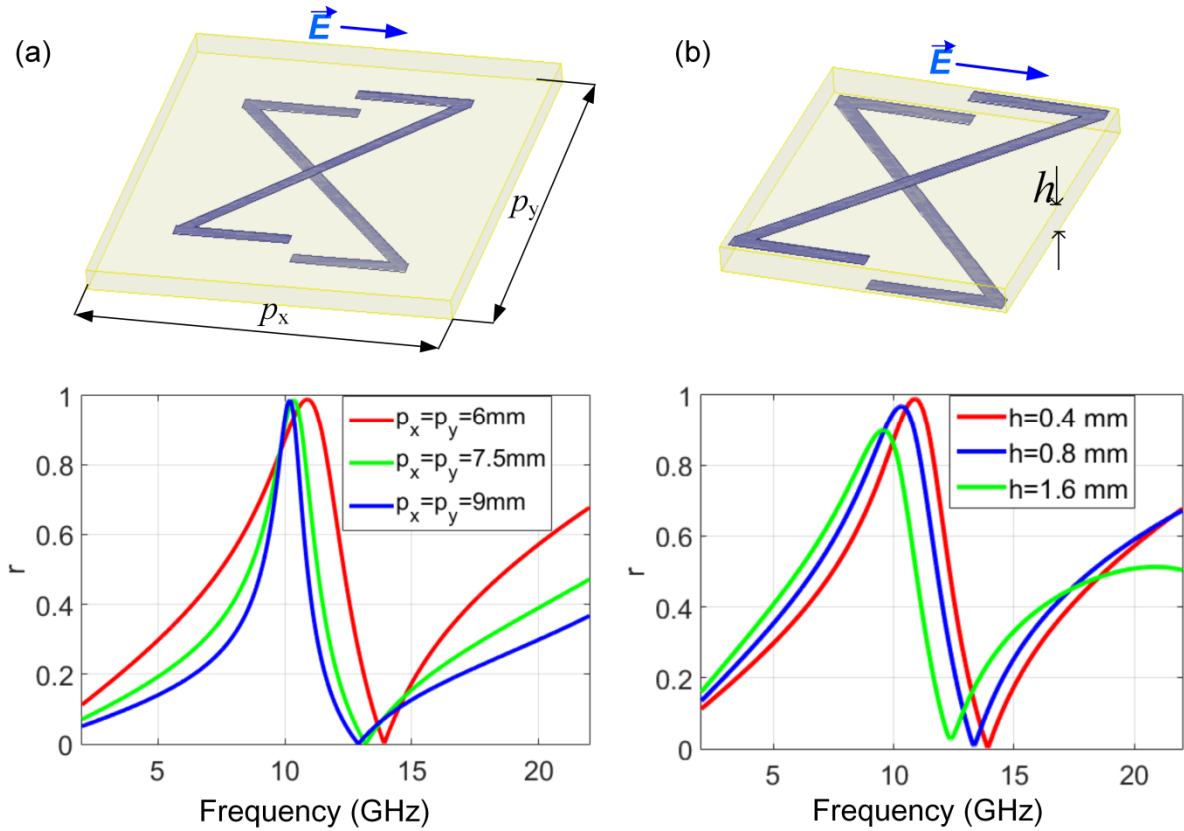


Fig. 5.2. Reflection and transmission spectra for non-overlapping Z resonators at vertical (a) and horizontal (b) polarization of E-field.

To demonstrate that the appearance of this phenomenon does not rely on coupling between adjacent unit cells, the simulation results are performed for a higher unit cell size, as depicted in Fig. 5.3a. The resonance keeps its asymmetric line shape and amplitude when the size of the unit cell is increased. The position of resonance frequency is only little sensitive to the variation of in-plane separation distance. Thus, the considered resonance is provided by excitation inside the unit cell. An increase in the thickness of dielectric substrate leads to a shift in resonance position and does not strongly influence the resonance line shape.



**Fig. 5.3. Variation of the unit cell period (a) and the thickness of dielectric spacer (b) for enantiomeric Z-shaped MS.**

To analyze the excitation mode for bi-layered Z structure the calculated instantaneous charge and current distribution at frequencies corresponding to reflection maximum and minimum are presented in Fig. 5.4. At the point of maximum reflection at 10.9 GHz the excitation of Z-elements represents two dipole moments excited along incident E-field polarization direction (Fig. 5.4a, c). However, owing to the enantiomeric geometry, such excitation form anti-symmetric mode along y-axis. At the minimum reflection at 13.9 GHz the dipoles turn in the opposite direction and intensity of forming currents is strongly reduced (Fig. 5.4b, d).

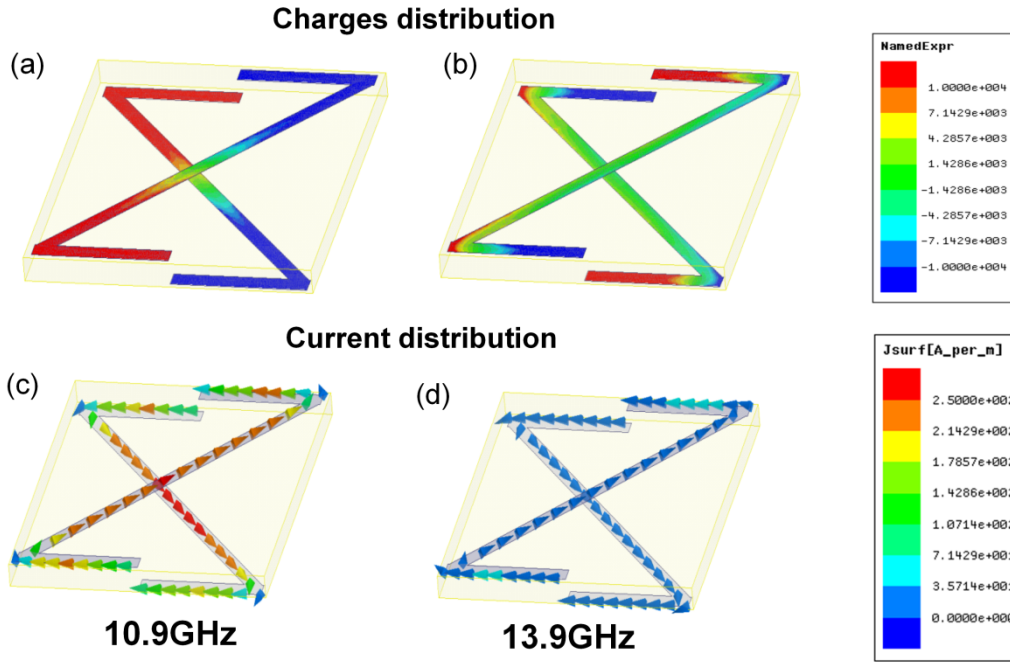


**Fig. 5.4.** Instantaneous charge and current distribution for bi-layered Z MS illuminated by horizontally polarized E-field.

It should be emphasized that the observed excitation is not based on the resonance of individual element. The simulation results for single-layered Z-shaped resonator illustrated in Fig. 5.5b demonstrates that with incident electric field polarized along y-axis, the excited resonance at 9.5 GHz corresponds to dipole excitation. However, as it can be seen from reflection spectra in Fig. 5.5c, d the resonance is not pronounced. The effective dipole excitation is observed only for electric field polarized along x-axis. We also demonstrate the similar behavior for the series of Z-shaped elements with increased horizontal parts, as shown in Fig. 5.5a. It should be noticed, that coupling to free-space of single meta-atom for dipole excitation is reduced for increasing resonator length (Fig. 5.5d). These features will be exploited for suppressing the radiation losses in bi-layered MS that provides drastically an increase in the resonance quality factor.

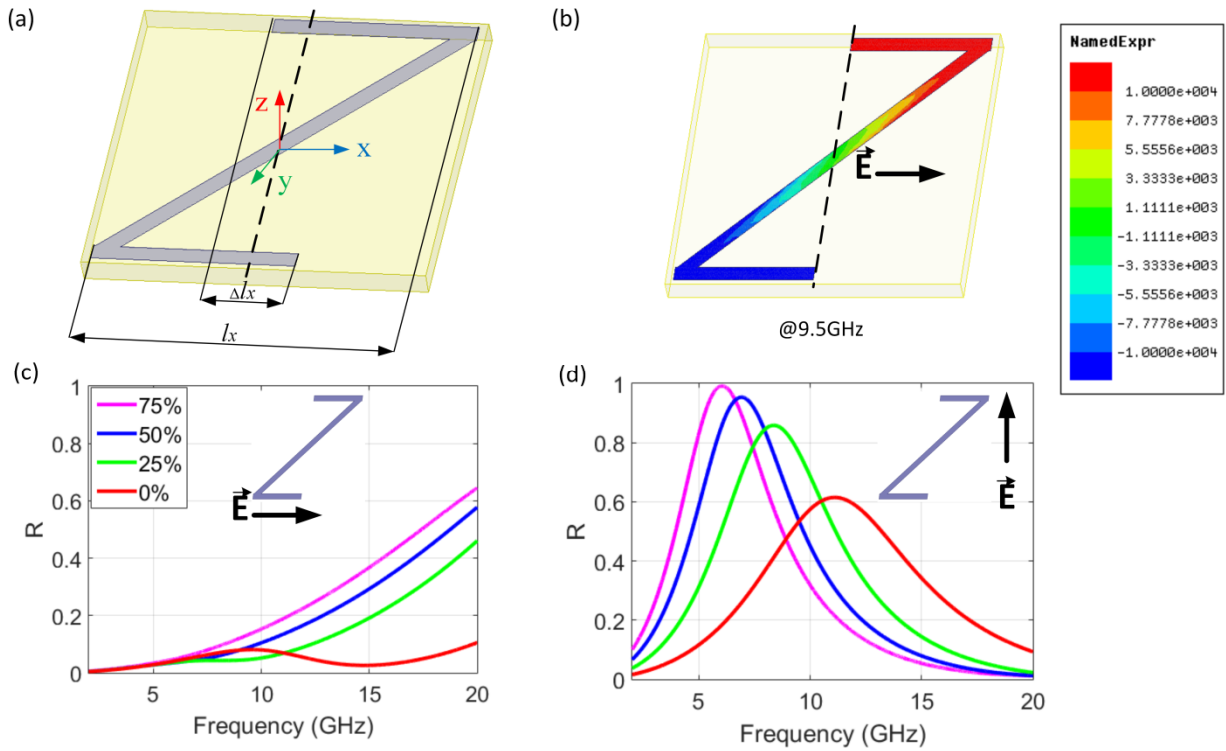


**Fig. 5.5. Single-layered Z-resonator. (a) Schematic of unit cell and principle of increasing horizontal legs. (b) Instantaneous charge distribution at 9.5 GHz for non-overlapping Z illuminated by horizontally polarized electric field. Reflection of series Z-element at different resonator lengths for horizontal (c) and vertical (d) polarization.**

The proposed method consists in designing bi-layered enantiomeric Z composed of partially overlapping elements as presented in Fig. 5.6a. By breaking the symmetry with respect to orientation of external electric field, oppositely induced currents are exciting antisymmetric mode. This results in suppression of radiation in overlapping parts. We denote the degree of overlapping as  $\frac{\Delta l_x}{l_x}$  which is ratio of the length of overlapping area and dimension  $l_x$ , as illustrated in Fig. 5.6a. For simplicity, we consider such designs from 0 to 100% overlap with step 25%. Simulated reflection and transmission characteristics for evolution of overlap illustrated in Fig. 5.6b-c demonstrate considerable increase of resonance quality factor with increase degree of overlap. For instance, Q-factor for 0% overlap Z equals to 3.8, while for 75% Q-factor reaches the value of 123. For fully overlapped Z, Fano resonance associated with antisymmetric dipole moments in coupled elements is not excited since such dipole mode is not allowed for this geometry. From symmetry consideration, the fundamental mode for 100% overlap Z for incident electric field orientated along y-axis corresponds to excitation of three co-directed dipole moments in diagonal and parallel legs of Z-shaped resonator. Obviously, that the

resonance frequency corresponding to this fundamental mode excitation is higher due to decrease of effective resonator length.

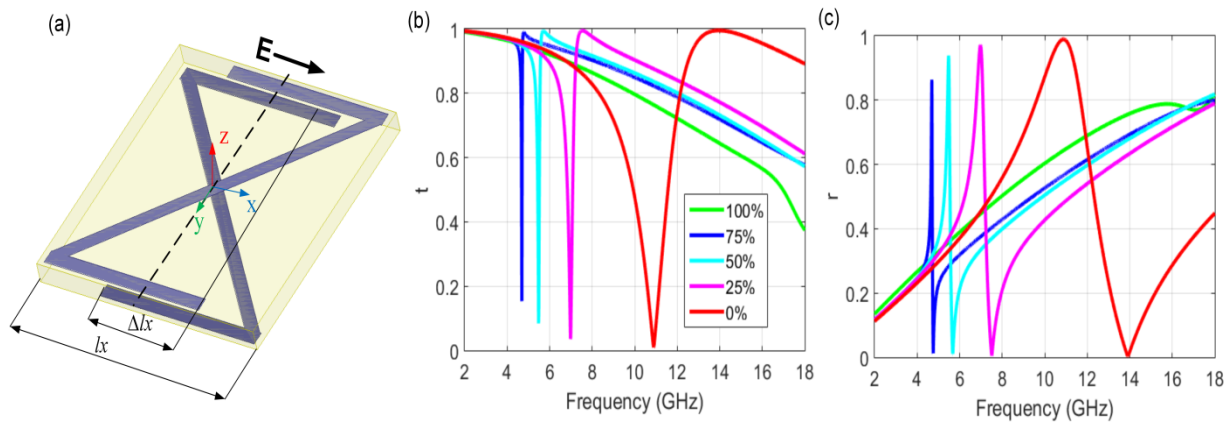


**Fig. 5.6. (a) Schematic of partially overlapping Z-shaped enantiomeric structures. (b)-(c) calculated transmission and reflection spectra for different ratio of Z legs overlap.**

To examine the reduction of radiation losses multipole decomposition analysis for 0% and 75% of overlap is performed (Fig. 5.7). The multipole decomposition represents the calculation of relative strength of the induced multipole moments contributing to the far-field response of the MSs [Fedotov 2013; Savinov 2014; Radescu 2002]. This method is based on expressions for the total radiated power derived by Radescu and Vaman [Radescu 2002] including three families of multipoles: electric, magnetic and toroidal type of excitation. The expression for the radiated power in case of harmonic excitation which is proportional to  $e^{i\omega t}$  has the form:

$$I = \frac{2\omega^4}{3c^3} |P|^2 + \frac{2\omega^4}{3c^3} |M|^2 + \frac{4\omega^5}{3c^4} \text{Im}[P^\dagger T] + \frac{2\omega^6}{3c^5} |T|^2 + \frac{\omega^6}{5c^5} |Q^{(e)}|^2 + \frac{\omega^6}{20c^5} |Q^{(m)}|^2 - \frac{2\omega^6}{15c^5} \text{Re}(M^\dagger \langle R_m^2 \rangle) \quad (4.47)$$

Note that expression is given in the CGS (Centimeter–gram–second) system of units. The first two terms correspond to the conventional electric and magnetic dipole scattering. The third term accounts for the interference between the electric and toroidal dipoles. The fourth term corresponds to the toroidal dipole scattering. The fifth and sixth terms represent electric and magnetic quadrupoles. The last term is a further correction resulting from the finite size of the current distribution in the meta-molecule. It is known as the “mean-square radius of the magnetic dipole term” and related to contribution of higher order terms. The further equations corresponds to representation of multipole terms in Cartesian basis more suitable for considered MS [Radescu 2002]:

$$\begin{aligned}
P_\alpha &= \frac{1}{i\omega} \int d^3r J_\alpha \\
M_\alpha &= \frac{1}{2c} \int d^3r [r \times J]_\alpha \\
T_\alpha &= \frac{1}{10c} \int d^3r [(r \cdot J) r_\alpha - 2r^2 J_\alpha] \\
\langle R_m^2 \rangle_\alpha &= \frac{1}{2c} \int d^3r [r \times J]_\alpha r^2 \\
Q_{\alpha\beta}^{(e)} &= \frac{1}{i2\omega} \int d^3r \left[ r_\alpha J_\beta + r_\beta J_\alpha - \frac{2}{3} \delta_{\alpha\beta} (r \cdot J) \right] \\
Q_{\alpha\beta}^{(m)} &= \frac{1}{3c} \int d^3r \left[ [r \times J]_\alpha r_\beta + r_\alpha [r \times J]_\beta \right]
\end{aligned} \tag{4.48}$$

According to computed intensity of multipole terms for bi-layered Z-shaped MSs illuminated by a plane wave with electric field orientated along y-axis, the strongest contribution to radiation is provided by the electric dipole particularly its y-component for both 0 and 75% overlapping structures. As it can be seen from Fig. 5.8c and d, the electric dipole excitation is consistent with reflection line shape in Fig. 5.8a and b. Other terms are very weak being by three order of magnitude smaller than electric dipole for both designs (Figs. 5.8e-f). As it can be noticed, the intensity of dipole terms is reduced approximately in ten times, when non-overlapping elements are transformed to 75% partially overlapping Z-resonators. Therefore, the reduction of radiation losses by using the proposed designing approach is also proven by multipole expansion.

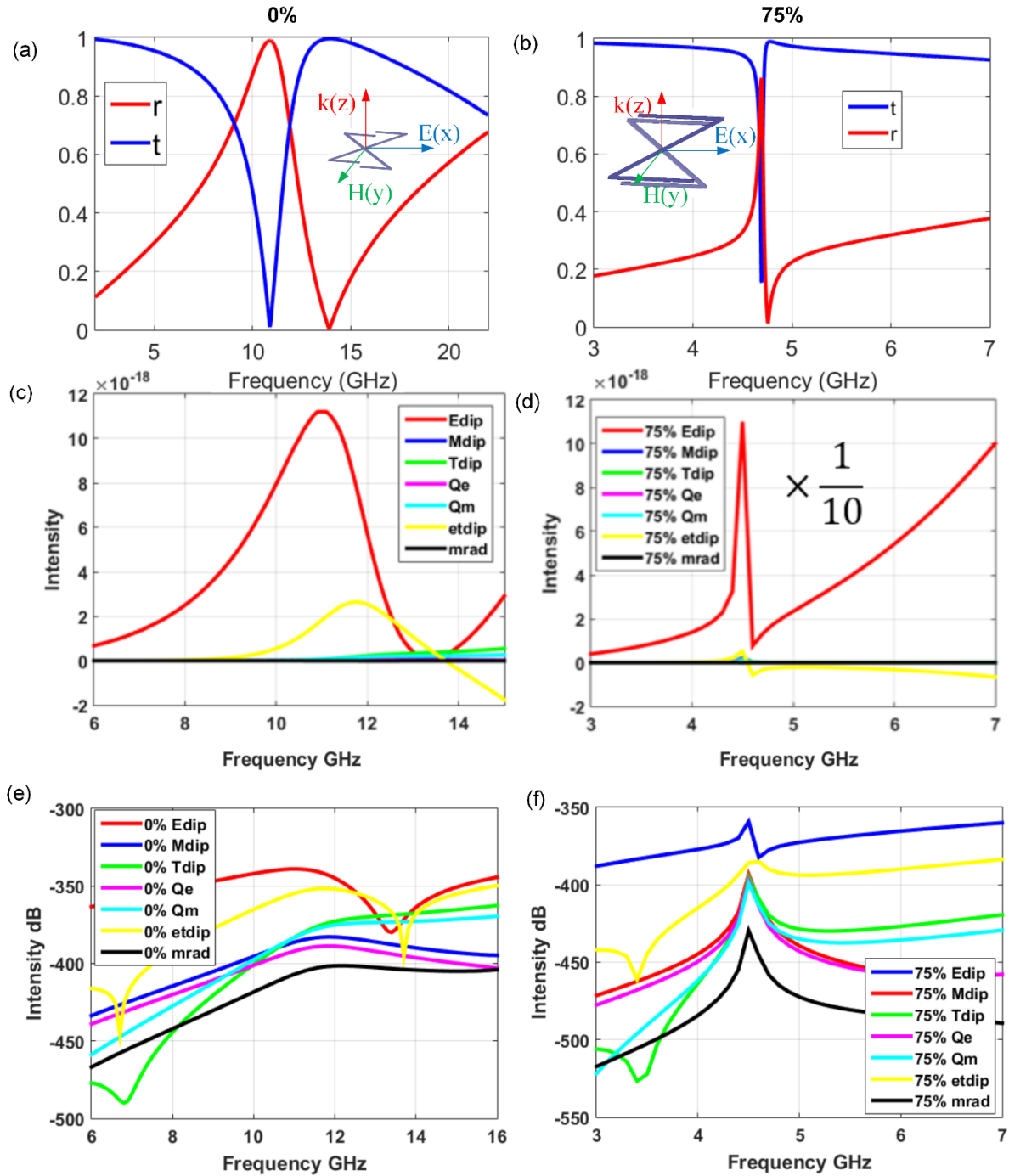
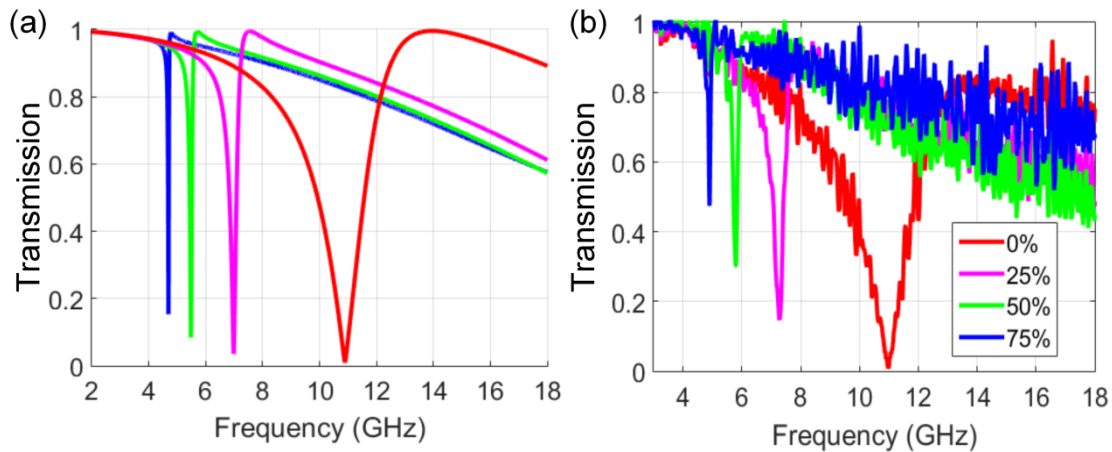


Fig. 5.8. Multipole decomposition for partially overlapping Z: left column corresponds to 0% overlap, right column corresponds to 75% overlapping. (a)-(b) transmission and reflection spectra.

## 5.2. Measurement result

To validate modeling results, prototypes of bi-layered enantiomeric atoms-based metasurface with partially overlapped resonators is fabricated using classical printed circuit board technology. Total sample size for each MS is  $35 \times 35$  cells on a  $210 \text{ mm} \times 210 \text{ mm}$  dielectric substrate. The material parameters of the substrate and the geometrical dimensions used for the

experimental validation are the same as in numerical simulations. Microwave transmission measurements have been done in accordance with description in section (2.6). Measured transmission characteristics for the family of Z-shaped designs show a good qualitative agreement with simulation results as it can be observed in Fig. 5.9.



**Fig. 5.9. Transmission coefficients for partially overlapping Z-shaped enantiomeric structures. (a) Simulations and (b) measurements.**

### 5.3. Excitation of second higher order mode

In this section we investigate resonance response of Z-shaped enantiomeric structure under normal incidence of electric field orientated along  $y$ -axis as displayed in Fig. 5.10a. Using the same design principle as in section 5.2 we consider evolution of partially overlapping Z from 0 to 100%. For the samples used for simulations, the length of the  $17 \mu\text{m}$  thick copper wires along the  $x$ - and  $y$ -directions is, respectively,  $l_y = 5.8 \text{ mm}$  and  $l_x = 5.7 \text{ mm}$ , and the width is  $w = 0.3 \text{ mm}$ . For the unit cell, the periods considered along  $x$ - and  $y$ - directions are respectively  $p_x = p_y = 6 \text{ mm}$ . The dielectric substrate used throughout this study for the printed circuit is a copper-cladded epoxy with a relative dielectric constant of 3.9 with tangential losses of 0.02 and a thickness of 0.4 mm.

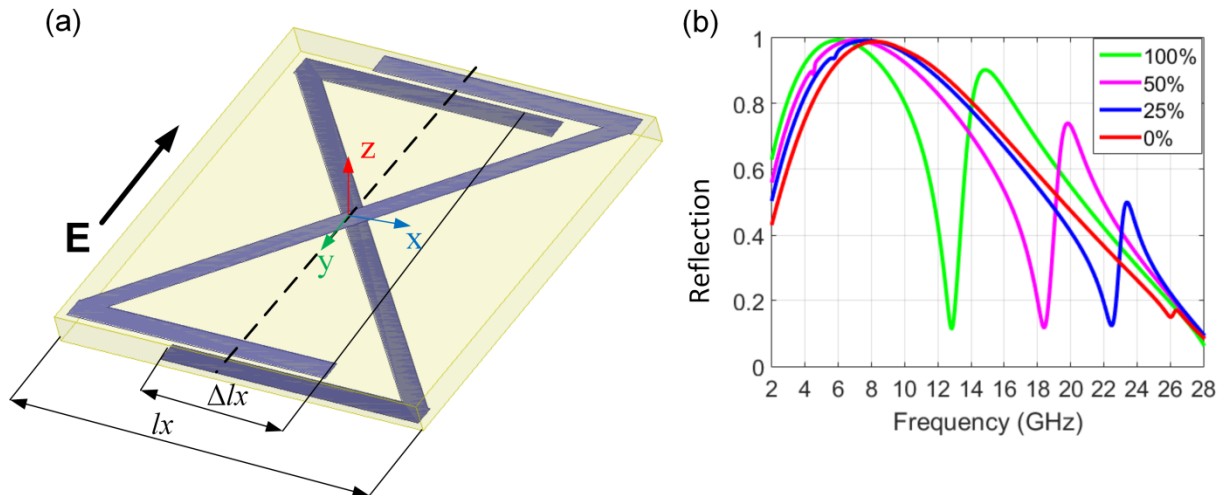


**Fig. 5.10. (a) Partially overlapping Z-shaped enantiomeric structures illuminated by normally incident electric field orientated along  $y$ -axis. (b) Calculated reflection spectra for the family of the design.**

As has been shown in Fig. 5.5d, under vertically polarized E-field the individual Z-element at increasing overlap exhibits reduction of fundamental resonance bandwidth. The same tendency is observed for enantiomeric structure presented in Fig. 5.10b. Besides fundamental resonance in the spectrum an additional mode appears at higher frequency which is more efficiently manifested at fully overlapping elements. This resonance is not observed neither for individual element or horizontally polarized light resulting from the symmetry matching of incident field and geometry. To further investigate this resonance excitation we will conduct our analysis by considering fully overlapping enantiomeric structure as schematically shown in the inset of Fig. 5.11a. Simulated reflection and transmission characteristics presented in Fig. 5.11a exhibit fundamental mode at 6 GHz and higher order mode at 13.5 GHz. Since the resonance line shape of second higher order mode is asymmetric we will determine its frequency position from maximum of absorption. The instantaneous current distributions illustrated in Fig. 5.11b-c indicates that resonances excited at 6 GHz and 13.5 GHz correspond to the lowest eigenmode frequency and the second higher order, respectively. It should be noted, that the described behavior is practically the same whether considering an ideal lossless substrate or a more realistic case with tangential losses of 0.02, as shown in Fig. 5.11a.

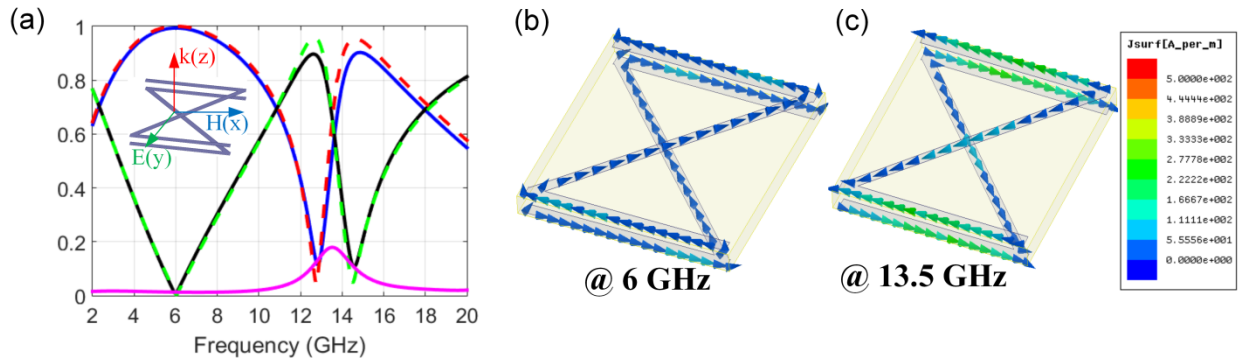


**Fig. 5.11. (a) Computed reflection and transmission coefficients for 100% overlapping Z-shaped enantiomeric structure. Solid and dotted curves correspond respectively to the substrate with tangential losses of 0.02 and without losses. Magenta curve corresponds to absorption when using lossy substrates. Instantaneous current distribution for fundamental mode (b) and second higher order mode (c).**

To evidence that excitation mechanism does not rely on coupling between adjacent unit cells, the simulation results are performed for different cell dimension corresponding to the increase of in-plane separation distance between adjacent elements, as depicted in Fig. 5.12. As it can be seen, in contrast to the fundamental resonance, the dark mode resonance is very little affected by the change of in-plane separation distance. Such a behavior is due to the very small value of electric dipolar momentum for second higher order mode resonance. This is not the case for the fundamental frequency bearing a strong electric dipolar momentum and by consequence strongly affected by the variation of separation distance. When the separation distance  $d$  between the two Z designs is varied, the second higher order mode resonance frequency is also little insensitive with respect to the variation of the separation distance in contrast to the fundamental mode (Fig. 5.13).

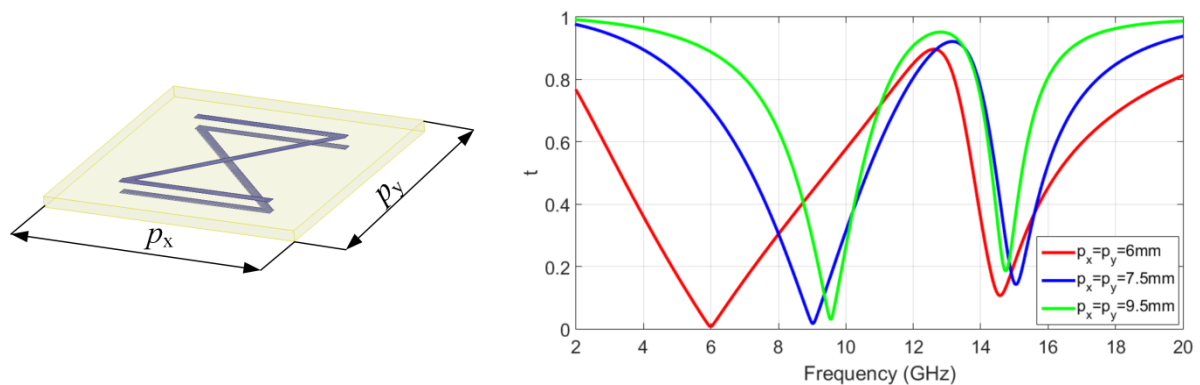


**Fig. 5.12. Variation of the unit cell period for enantiomeric Z-shaped MS.**

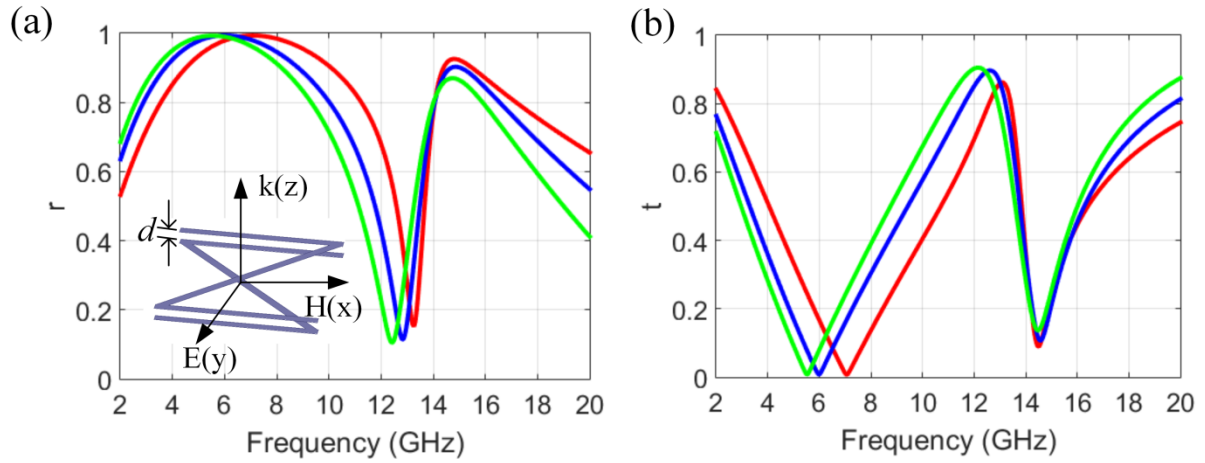


**Fig. 5.13. Variation of the thickness of dielectric spacer for enantiomeric Z-shaped MS.**

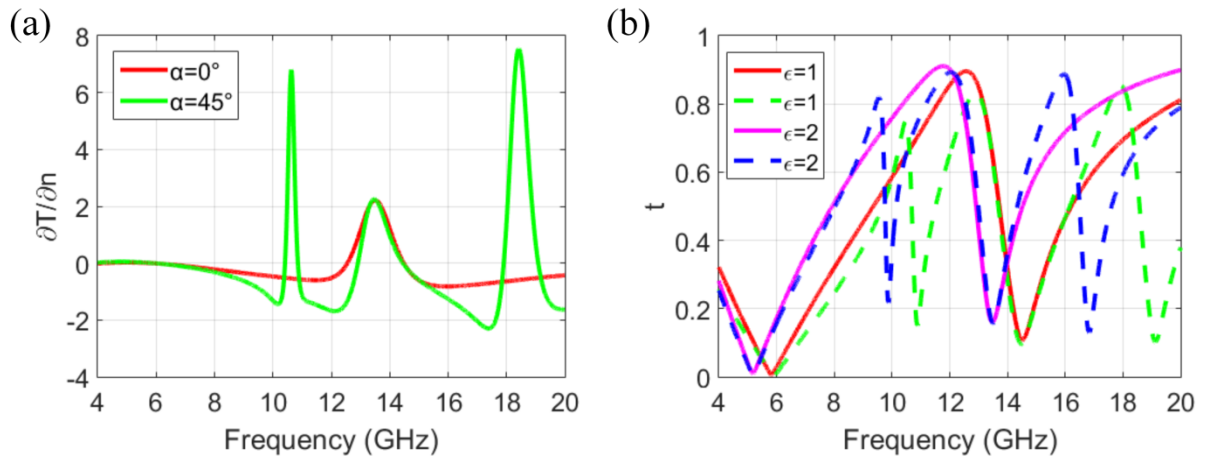


**Fig. 5.14. (a) Derivative  $\partial T/\partial n$ , corresponding to the variation of transmission for an infinitesimally small variation of the surrounding media refractive index. (b) Transmission coefficients under normal (continuous traces) and  $45^\circ$  oblique incidence (dashed traces) of the bi-layered enantiomeric structure immersed in a medium having permittivity 1 and 2.**

The robustness of dark mode associated with second higher order resonance with respect to the variation of in-plane or inter-layers separation distance makes it particularly attractive for the implementation in the optical domain in view of surface species sensor applications. To quantify the sensitivity of the investigated structure for such applications, the derivative  $\partial T/\partial n$ , corresponding to the variation of transmission for an infinitesimally small variation of the surrounding media refractive index, is calculated. As it can be observed under normal incidence from Fig. 5.14a, the derivative  $\partial T/\partial n$  reaches a maximum at 13.5 GHz that corresponds to the steepest variation of transmission associated with the second higher order mode resonance. The value of  $\partial T/\partial n$  at this frequency is several times higher with respect to the fundamental

frequency region, meaning that the second higher order mode resonance would provide much better sensitivity for sensor applications.

The ability of multi-spectral sensing operation is another important advantage of the considered enantiomeric structure. Indeed, under oblique incidence, the Z-shaped enantiomeric structure supports direct excitation of dipolar and quadrupolar magnetic mode resonances as shown at respectively 10.7 GHz and 18.3 GHz in Figs. 5.14b and 5.15a. We consider oblique incidence (angle  $\alpha$ ) in H-plane (plane containing vectors  $H$  and  $k$ ) where magnetic field excitation occurs. These modes possess a zero net electric dipolar momentum leading to less radiation losses and therefore a higher resonance quality factor of the response with respect to the electric dipole mode excitation. Such principle of direct dark mode excitation has been considered in detail in Chapter 3. Quality factor for dipolar magnetic resonance at 10.7 GHz is equal to 5.4 in comparison to 0.8 and 3.7 for fundamental and second high order modes respectively. Instantaneous currents distributions of Fig. 5.16 show that these magnetic modes exhibit current loops in horizontal plane that result in magnetic momenta. Consequently, direct excitation of additional “dark mode” resonances by using magnetic field component of the incident electromagnetic wave becomes possible. The derivative  $\partial T/\partial n$  for 45° oblique incidence displayed in Fig. 5.14a shows that the sensitivity associated with magnetic dark modes can be even higher than that of the second higher order electric mode.

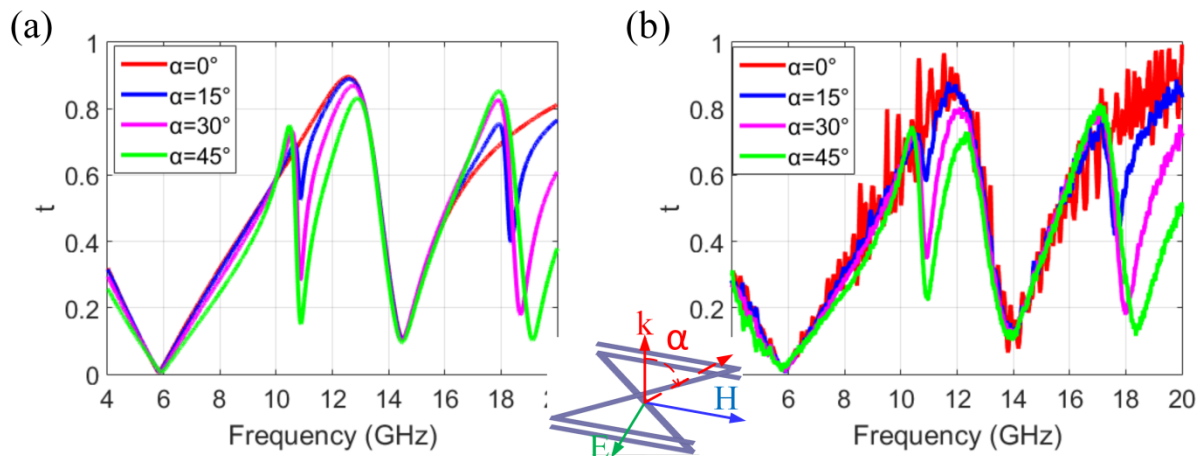


**Fig. 5.15. Transmission coefficients under normal and oblique incidence: (a) Simulations. (b) Measurements.**

Their sensitivity level can be monitored through the variation of the incidence angle. Such kind of multi-spectral operation with adjustable level of sensitivity for selected spectral domains allows a better discrimination of species and greatly enhances the robustness and sensitivity of

sensor operations. As qualitative example, we provide modification of the frequency response of the investigated bi-layered enantiomeric structure when it is immersed in a liquid having permittivity  $\epsilon_r = 2$ . A strong shift of the spectral response towards lower frequencies is noted (Fig. 5.14b). In agreement with previous analysis, the variation of transmission (reflection) are especially important at frequencies corresponding to the excitation of the dark modes.

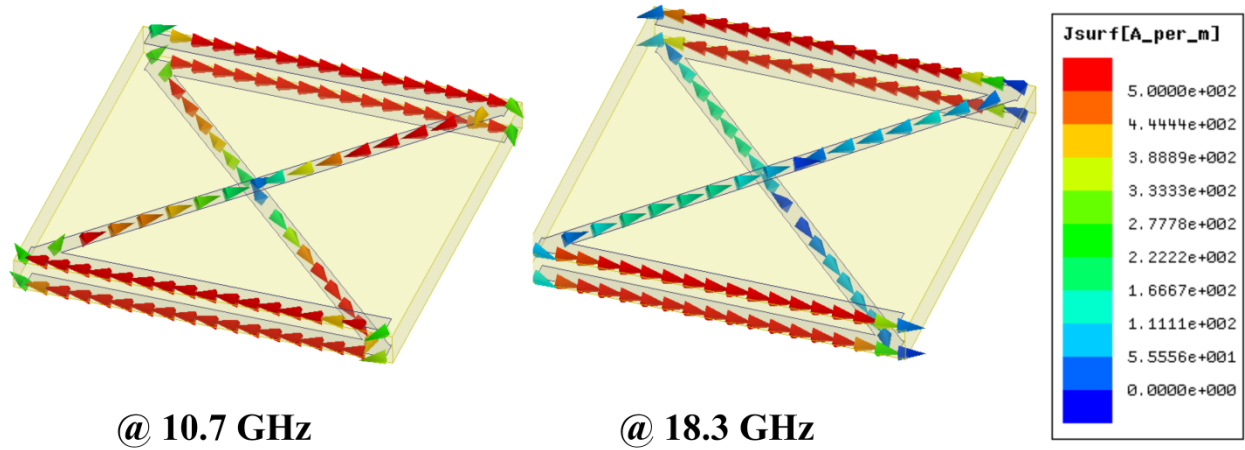


**Fig. 5.16. Computed instantaneous current distributions for dipolar magnetic mode at 10.7 GHz and quadrupolar magnetic mode at 18.3 GHz.**

To validate modeling results, a prototype of the enantiomeric atoms-based metasurface was fabricated with the total sample size  $35 \times 35$  cells on a  $210 \text{ mm} \times 210 \text{ mm}$  dielectric substrate. The material parameters of the substrate and the geometrical dimensions used for the experimental validation are the same as in numerical simulations. Microwave transmission measurements were conducted according to description in section 2.7. Measured transmission characteristics show a good qualitative agreement with simulation results as it can be observed in Fig. 5.15b.

## 5.4. Conclusions

In this chapter the resonance behavior for enantiomeric structures have been considered. Enantiomeric Z-shaped structure exhibit either narrow Fano resonance related to the electric dipole excitation or electric second higher order mode depending on symmetry matching of incident field orientation and geometry. For the Fano resonance excitation the method providing increase of quality factor more than 30 times by suppressing radiation losses has been performed.

## 5.4 Conclusions

---

The obtained electric second higher mode presents important advantages for multi-spectral sensor applications compared to fundamental resonance excitation.

## References

- [Alpeggiani 2017] F. Alpeggiani, N. Parappurath, E. Verhagen & L. Kuipers, 2017. “Quasinormal-Mode Expansion of the Scattering Matrix”. *Physical Review X*, 7.
- [Fedotov 2013] V.A. Fedotov et al., 2013. “Resonant Transparency and Non-Trivial Non-Radiating Excitations in Toroidal Metamaterials”. *Scientific Reports*, 3.
- [Lepetit 2010] T. Lepetit, E. Akmansoy, J.-P. Ganne & J.-M. Lourtioz, 2010. “Resonance continuum coupling in high-permittivity dielectric metamaterials”. *Physical Review B*, 82.
- [Maslovski 2009] S.I. Maslovski, D.K. Morits & S.A. Tretyakov, 2009. “Symmetry and reciprocity constraints on diffraction by gratings of quasi-planar particles”. *Journal of Optics A: Pure and Applied Optics*, 11, p.074004.
- [Parappurath 2017] N. Parappurath, F. Alpeggiani, L. Kuipers & E. Verhagen, 2017. “The Origin and Limit of Asymmetric Transmission in Chiral Resonators”. *ACS Photonics*, 4, pp.884-890.
- [Radescu 2002] E.E. Radescu & G. Vaman, 2002. “Exact calculation of the angular momentum loss, recoil force, and radiation intensity for an arbitrary source in terms of electric, magnetic, and toroid multipoles”. *Physical Review E*, 65.
- [Savinov 2014] V. Savinov, V.A. Fedotov & N.I. Zheludev, 2014. “Toroidal dipolar excitation and macroscopic electromagnetic properties of metamaterials”. *Physical Review B*, 89.

## Chapter 6.

# Conclusions and Outlooks for Future Work

### 6.1. Conclusions

The goal of this thesis is to explore innovative methods to improve the quality factors of metasurface resonance response in microwave and optical domains. The study is focused on solutions allowing the suppression of radiative losses by using concepts of dark mode and Fano resonance. In this thesis, we investigate excitation mechanism in individual resonators as well as in systems of coupled elements.

In the Chapter 3 it is shown theoretically and experimentally that dark mode excitation in individual resonator can be achieved in an independent manner not relying on mode hybridization. The proposed method is based on symmetry matching approach. It consists in designing resonant elements operating in the first higher order mode, whose excitation through the electric component of the incident field is forbidden but instead allowed for the magnetic component under oblique incidence on the MS. We demonstrate highly efficient S-shaped resonator dark mode resonance excitation in the optical domain exhibiting sharp spectral features far exceeding those of the conventional SRR resonator. Symmetry matching approach is extended to the complementary MSs providing dark mode resonances in reflection as well as in transmission with quality factor about 30 times higher than for the fundamental resonance.

The second part of our study is dedicated to the Fano resonance excitation mechanism in a system of identical coupled resonators. The theoretical analysis is performed by using TCMT accounting for the existence of two propagation pathways either through indirect resonance coupling or direct free-space propagation to explain Fano interference effect. Two general configurations are considered corresponding to symmetric and enantiomeric space arrangement of resonators. The TCMT modeling shows that Fano resonance appears in the vicinity of high quality factor anti-symmetric mode for both cases. We demonstrate that cavity systems formed by near-field coupled symmetrically stacked metasurfaces provides sharp spectral characteristics. In the absence of absorption losses, the quality factor of such a cavity would tend to infinity in the limit of infinitesimally thin cavity. The advantage of such deeply subwavelength thickness length MSs cavity with respect to the far-field coupled MS Fabry-Perot cavities consists in less influence of absorption losses due to smaller physical volume and no need for matching of cavity length with respect to plasmon resonance frequency. It is confirmed that radiation losses of bi-

layered MSs can be reduced by using Z-shaped resonator design increasing resonance quality factor.

In Chapter 5, the mechanism of Fano resonance for single and double-layered structures which go beyond the model of mirror symmetry systems have been considered on the basis of CMT formalism. We show that condition of appearance of narrow anti-symmetric mode is related to the breaking of space symmetry with respect to the exciting ports. We also propose a design solution providing increase of Fano resonance quality factor more than 30 times by suppressing radiation losses in partially overlapping enantiomeric Z-shaped resonators.

## 6.2. Outlooks for Future Work

As we discuss in Chapter 1, the ability of metasurfaces to control electromagnetic radiation in an efficient manner makes them promising for numerous applications. The recent trends in MSs are focused on their application in filtering and sensing functionalities requiring high performance MSs. In this thesis we investigate theoretically and experimentally methods providing higher resonator's quality factor based on the concept of dark modes and Fano resonances. This work is intended to bring a contribution for the next generation of optical biosensors and telecom filters. Our theoretical analysis on the basis of coupled mode theory formalism can be useful for the future progress in optimized applications of Fano resonance in MS structures.

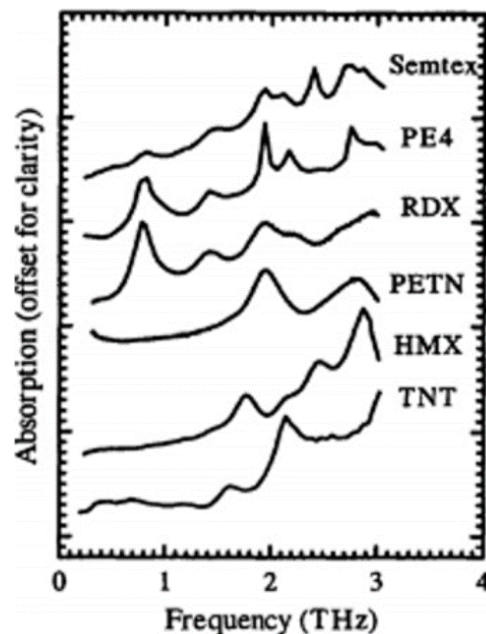
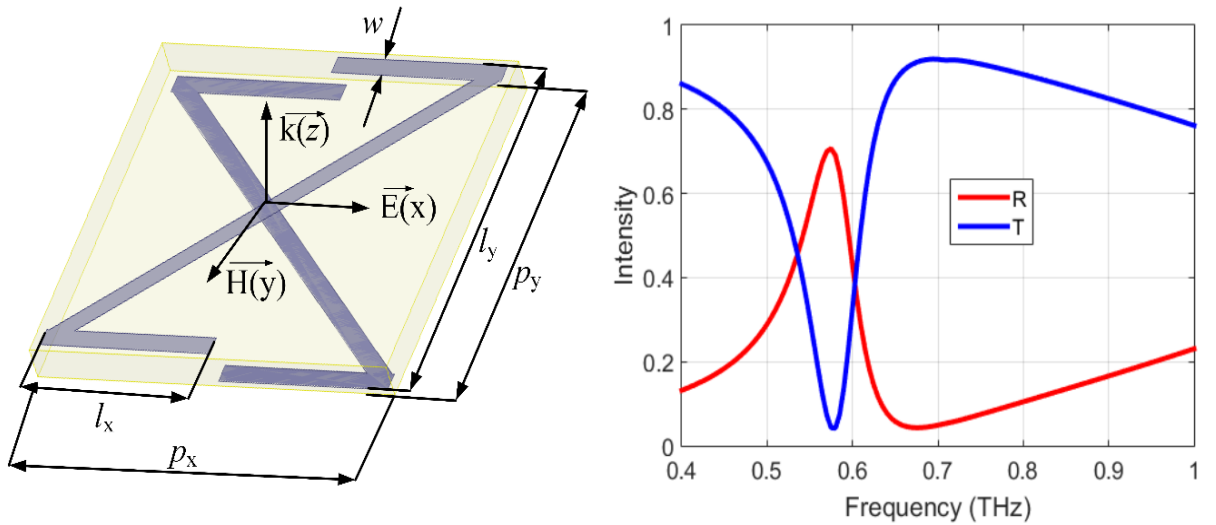


Fig. 6.1. THz spectra of explosives [Federici 2005].

The largest part of our work is performed in microwave. However, the main interest in sensing lies in THz frequency regime, especially for security purposes as illustrated in Fig. 6.1 [Chen 2012; Federici 2005; Jak 2007; Singh 2014]. For this reason, the goal is to extend the methods and results of this thesis to the THz frequency range.

To have an idea of the possibilities of our design in THz regime, we perform simulations demonstrating Fano resonances in the enantiomeric structure and metasurface cavity at about 0.5 THz, as presented in Figs. 6.2 and 6.3. Spectral characteristics under normal incidence exhibit narrow resonances compared to fundamental mode with quality factors  $Q = 7$  and  $Q = 9.1$  for enantiomeric structure and metasurface cavity, respectively. For the simulations, the metal of resonant element is set as gold with DC conductivity of  $41 \times 10^6$  Siemens/m.

Thus, the considered metasurfaces can be applied for THz frequency range. However, the main key point is to find an optimal geometry accounting for the difficulties of technological realization of such structures.



**Fig. 6.2.** Schematic design and spectral characteristics of enantiomeric metasurface. The unit cell period along x- and y-axis are  $p_x = p_y = 90 \mu\text{m}$ , the dimensions  $l_x = l_y = 80 \mu\text{m}$ , the width of metallic wire is  $w = 5 \mu\text{m}$  and the thickness of metallic resonator is  $0.2 \mu\text{m}$ . The dielectric substrate is silicon dioxide with relative permittivity  $\epsilon_r = 4$ ,  $\tan \delta = 0$  and the thickness  $h = 0.3 \mu\text{m}$ .

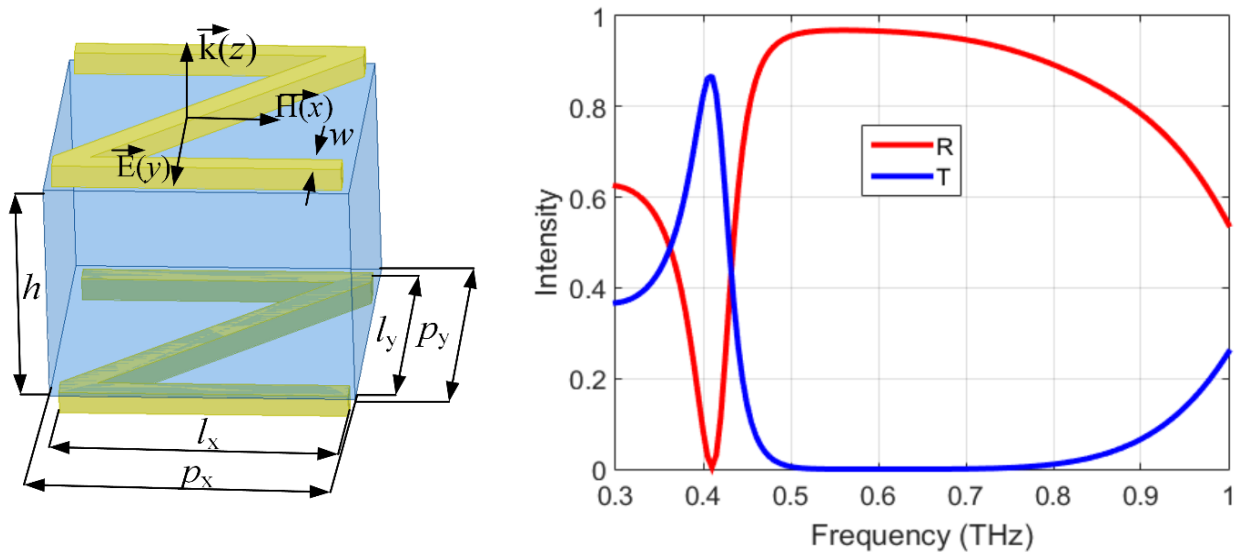


**Fig. 6.3. Schematic design and spectral characteristics of metasurface.** The unit cell period along  $x$ - and  $y$ -axis are  $p_x = p_y = 65.63 \mu\text{m}$ , the dimensions  $l_x = l_y = 62.13 \mu\text{m}$ , the width of metallic wire is  $w = 5 \mu\text{m}$  and the thickness of metallic resonator is  $4 \mu\text{m}$ . The dielectric substrate is silicon dioxide with relative permittivity  $\epsilon_r = 4$ ,  $\tan \delta = 0$  and the thickness  $h = 50 \mu\text{m}$

## References

- [Chen 2012] T. Chen, S. Li & H. Sun, 2012. “Metamaterials Application in Sensing”. *Sensors*, 12, pp.2742-2765.
- [Federici 2005] J.F. Federici et al., 2005. “THz imaging and sensing for security applications—explosives, weapons and drugs”. *Semiconductor Science and Technology*, 20, pp.S266--S280.
- [Jak 2007] Z. Jak, O. Jak, Z. Djuri & C. Kment, 2007. “A consideration of the use of metamaterials for sensing applications: field fluctuations and ultimate performance”. *Journal of Optics A: Pure and Applied Optics*, 9, pp.S377--S384.
- [Singh 2014] R. Singh et al., 2014. “Ultrasensitive terahertz sensing with high-Q Fano resonances in metasurfaces”. *Applied Physics Letters*, 105, p.171101.



## List of publications

### International peer-reviewed journals

1. E. Bochkova, S. N. Burokur, A. de Lustrac, A. Lupu, “Dark modes engineering in metasurfaces by symmetry matching approach,” *Applied Physics A: Materials Science & Processing*, vol. 124, no. 2, p. 119, February 2018.
2. B. Ratni, E. Bochkova, G.-P. Piau, A. de Lustrac, A. Lupu, S. N. Burokur, “Design and engineering of metasurfaces for high-directivity antenna and sensing applications,” *EPJ Applied Metamaterials*, vol. 3, 4, July 2016. (Topical Issue - Metamateterial-by-Design: Theory, Methods, and Applications)
3. E. Bochkova, S. N. Burokur, A. de Lustrac, A. Lupu, “Direct dark modes excitation in bi-layered enantiomeric atoms-based metasurface through symmetry matching,” *Optics Letters*, vol. 41, no. 2, pp. 412-415, January 2016.

### International conferences

1. E. Bochkova, S. N. Burokur, A. de Lustrac, A. Lupu, “Dark modes engineering in metasurfaces,” *11<sup>th</sup> International Congress on Engineered Material Platforms for Novel Wave Phenomena – Metamaterials 2017*, Marseille (France), August-September 2017.
2. E. Bochkova, S. N. Burokur, A. de Lustrac, A. Lupu, “Metasurfaces for dark mode resonances characteristics,” *8<sup>th</sup> International Conference on Metamaterials, Photonic Crystals and Plasmonics (META'17)*, Incheon (Korea), July 2017. (Invited)
3. E. Bochkova, A. de Lustrac, A. Lupu, T. Lepetit, S. N. Burokur, “Sharp Fano resonances in bi-layered symmetric Z-structures,” *IEEE International Symposium on Antennas and Propagation and USNC-URSI Radio Science Meeting*, San Diego (USA), July 2017.
4. B. Ratni, E. Bochkova, G.-P. Piau, A. de Lustrac, A. Lupu, S. N. Burokur, “Metasurfaces for antennas and sensors,” *IEEE Radio and Antenna Days of the Indian Ocean (RADIO 2016)*, Réunion Island, October 2016.
5. E. Bochkova, S. N. Burokur, A. de Lustrac, A. Lupu, “Electromagnetically induced transparency through magnetic field interactions in bilayered enantiomeric metasurfaces,” *10<sup>th</sup> International Congress on Advanced Electromagnetic Materials in Microwaves and Optics – Metamaterials 2016*, Chania (Crete), September 2016.
6. N. Dubrovina, E. Bochkova, S. N. Burokur, A. de Lustrac, A. Ramdane, A. Lupu, “Symmetry approach to the dark modes metasurfaces,” *International Conference on Metamaterials and Nanophotonics (METANANO 2016)*, Anapa (Russia), September 2016. (Invited)
7. E. Bochkova, S. N. Burokur, A. de Lustrac, A. Lupu, “Far field dark modes excitation and electromagnetically induced transparency,” *7<sup>th</sup> International Conference on Metamaterials, Photonic Crystals and Plasmonics (META'16)*, Malaga (Spain), July 2016.
8. E. Bochkova, S. N. Burokur, A. de Lustrac, A. Lupu, “Direct dark modes excitation through symmetry matching in Z-shape atoms bilayer enantiomeric metamaterials,” *9<sup>th</sup> International Congress on Advanced Electromagnetic Materials in Microwaves and Optics – Metamaterials 2015*, Oxford (UK), September 2015.
9. N. Dubrovina, E. Bochkova, S. N. Burokur, A. de Lustrac, A. Martinez, A. Ramdane, A. Lupu, “Dark modes excitation and symmetry related properties of metasurfaces,” *17<sup>th</sup>*

*International Conference on Transparent Optical Networks (ICTON 2015)*, Budapest (Hungary), July 2015. (Invited)

10. E. Bochkova, S. N. Burokur, A. de Lustrac, A. Lupu, "Engineering dark mode resonances in Z-metasurfaces for sensing applications," *First International Workshop on Metamaterials-by-Design: Theory, Methods, and Applications to Communications and Sensing*, Paris Saclay (France), December 2015.

#### **National (French) conferences**

1. E. Bochkova, A. Lupu, A. de Lustrac, S. N. Burokur, "Résonances à fort facteur de qualité par une géométrie adaptée à l'onde incidente," *Assemblée générale GDR Ondes 2017*, Nice, Octobre 2017.
2. E. Bochkova, N. Dubrovina, S. N. Burokur, A. de Lustrac, A. Lupu, "Métasurface à modes sombres et transparence induite électromagnétiquement," Colloque National Métamatériaux 2017, Orsay, Mars 2017. (Invité)
3. N. Dubrovina, E. Bochkova, S. N. Burokur, J.-M. Manceau, R. Colombelli, A. de Lustrac, A. Ramdane, A. Lupu, "The symmetry approach to the metasurfaces dark modes excitation and electromagnetically induced transparency," *LIA ALPhFA Second Workshop*, Marseille, France, June 2016.
4. E. Bochkova, S. N. Burokur, A. de Lustrac, A. Lupu, "Excitation directe de modes sombres dans les métasurfaces," *Assemblée générale GDR Ondes 2015*, Lyon, Octobre 2015.

**Titre :** Concepts avancés de métamatériaux pour l'électromagnétisme et la photonique

**Mots clés :** métamatériaux, mode sombre, résonance de Fano, facteur de qualité

**Résumé :** Les métasurfaces permettent de contrôler efficacement les rayonnements électromagnétiques en manipulant la phase, l'amplitude et la polarisation des ondes. Pour de nombreuses applications, telles que des fonctions d'agilité, de commutations et de détection, des surfaces de haute performance sont nécessaires. L'objectif de cette thèse est d'explorer des méthodes innovantes permettant d'améliorer les facteurs de qualité des métasurfaces dans les domaines micro-ondes et optique. La limitation des métasurfaces est généralement liée aux pertes par rayonnement et à l'absorption non radiative.

L'étude se concentre sur des solutions permettant la suppression des pertes de rayonnement en utilisant des concepts de mode sombre et de résonance de Fano. Un mécanisme d'excitation direct de mode sombre dans un résonateur individuel basé sur l'adaptation de symétrie est

proposé. La possibilité d'améliorer l'efficacité de la réponse magnétique en optique est présentée.

L'analyse de l'excitation par résonance de Fano dans un système de résonateurs couplés identiques est également réalisée sur la base du formalisme de la théorie des modes couplés. Deux configurations générales correspondant à l'arrangement spatial symétrique et énantiomères des résonateurs sont considérées. Dans le premier cas, le système de cavité formé par les métasurfaces très proches fournit des caractéristiques spectrales très étroites et une sensibilité efficace élevée par rapport aux cavités Fabry-Perot conventionnelles. Dans le second cas, les caractéristiques de conception permettent de contrôler la suppression des pertes de rayonnement, permettant d'augmenter considérablement le facteur de qualité de la résonance de Fano.

**Title :** Advanced concepts of metamaterials for electromagnetism and photonics

**Keywords :** metamaterials, dark mode, Fano resonance, quality factor

**Abstract:** Metasurfaces allows an effective control of electromagnetic radiation by manipulating phase, amplitude and polarization of electromagnetic waves. For numerous applications including tunable, switchable and sensing functionalities, high performance metasurfaces are required. The goal of this thesis is to explore innovative methods enabling to improve the quality factors of metasurfaces in microwave and optical domains. The limitation of metasurfaces is generally related to radiation losses and non-radiative absorption.

The study is focused on solutions allowing the suppression of radiative losses by using concepts of dark mode and Fano resonance. A direct dark mode excitation mechanism in individual resonator based on symmetry

matching is proposed. The possibility to enhance magnetic response efficiency in optical frequency range is presented.

Analysis of Fano resonance excitation in a system of identical coupled resonators is also performed on the basis of coupled mode theory formalism. Two general configurations are considered corresponding to symmetric and enantiomeric space arrangement of resonators. In the first case, cavity system formed by near-field coupled metasurfaces provides sharp spectral characteristics and high efficient sensitivity compared to conventional Fabry-Perot cavities. In the second case the design features enables to control suppression of radiation losses, allowing to considerably increase Fano resonance quality factor.

